

**INERTIAL CONFINEMENT  
FUSION AS A TOOL TO STUDY  
FUNDAMENTAL NUCLEAR  
SCIENCE**

By

Tyler M. Kowalewski

A thesis submitted in partial fulfillment of the  
requirements for the degree of

Bachelor of Science

Houghton College

May 2021

Signature of Author.....

Department of Physics  
May 12, 2021

.....

Dr. Mark Yuly  
Professor of Physics  
Research Supervisor

.....

Dr. Brandon Hoffman  
Professor of Physics

# INERTIAL CONFINEMENT FUSION AS A TOOL TO STUDY FUNDAMENTAL NUCLEAR SCIENCE

By

Tyler M. Kowalewski

Submitted to the Department of Physics  
on May 12, 2021 in partial fulfillment of the  
requirement for the degree of  
Bachelor of Science

## **Abstract**

Inertial confinement fusion may possibly be used to make fundamental nuclear science measurements of low energy light ion cross-sections of interest in astrophysics and fusion research. The feasibility of collecting and counting the beta decay of the reaction products (half-life 20 ms to 20 s) in the expanding neutral gas after the ICF shot is being studied using a special vacuum system that allows a radioactive gas to be released, trapped, and counted in situ using different techniques. Initial experiments have used a turbopump to trap the gas in the foreline, where it can be counted by a  $4\pi$  phoswich beta detector. The construction and simulation of this detector, tests using  $^{41}\text{Ar}$  gas produced via the  $^{40}\text{Ar}(d,p)^{41}\text{Ar}$  reaction, and an OMEGA laser ride along experiment to measure background rates from milliseconds to seconds after a high yield D-T laser shot will be described.

Thesis Supervisor: Dr. Mark Yuly  
Title: Professor of Physics

*This material is based upon work supported by the Department of Energy [National Nuclear Security Administration] University of Rochester “National Inertial Confinement Program” under Award Number(s) DE-NA0004144.*

*This report was prepared as an account of work sponsored by an agency of the United States Government. Neither the United States Government nor any agency thereof, nor any of their employees, makes any warranty, express or implied, or assumes any legal liability or responsibility for the accuracy, completeness, or usefulness of any information, apparatus, product, or process disclosed, or represents that its use would not infringe privately owned rights. Reference herein to any specific commercial product, process, or service by trade name, trademark, manufacturer, or otherwise does not necessarily constitute or imply its endorsement, recommendation, or favoring by the United States Government or any agency thereof. The views and opinions of authors expressed herein do not necessarily state or reflect those of the United States Government or any agency thereof.*

## TABLE OF CONTENTS

<b>Chapter 1 Introduction .....</b>	<b>8</b>
<b>1.1 Introduction to Fusion Research .....</b>	<b>8</b>
1.1.1 Measuring Light-Ion Cross Sections .....	8
<b>1.2 Thermonuclear Reactions and Fusion .....</b>	<b>12</b>
1.2.1 Uncontrolled Thermonuclear Fusion .....	12
1.2.2 Controlled Thermonuclear Fusion .....	13
1.2.2.1 Gravitational Confinement Fusion .....	13
1.2.2.2 Magnetic Confinement Fusion .....	14
1.2.2.3 Inertial Electrostatic Confinement Fusion .....	15
1.2.2.4 Inertial Confinement Fusion .....	15
1.2.3 ICF as a Tool to Measure Light-Ion Fusion Cross Sections.....	17
<b>1.3 The Experiment .....</b>	<b>18</b>
1.3.1 Previous Work at Houghton .....	21
<b>1.4 Current Progress .....</b>	<b>24</b>
1.4.1 Phoswich Detector System .....	24
1.4.2 Particle Categorization with a Phoswich Detector System .....	25
1.4.3 The $^{41}\text{Ar}$ Experiment and the LLE Ride-Along Experiment .....	27
<b>Chapter 2 Theory .....</b>	<b>28</b>
<b>2.1 Introduction .....</b>	<b>28</b>
<b>2.2 Cross Sections .....</b>	<b>28</b>
<b>2.3 Reaction Rate and Average Reactivity .....</b>	<b>29</b>
<b>2.4 Reaction Yields .....</b>	<b>31</b>
2.4.1 Predicting Cross Sections and Yields.....	31
2.4.1.1 S-Factor Extrapolation.....	32
2.4.1.2 TALYS .....	33
2.4.1.3 R-Matrix.....	33
2.4.2 Radioisotopes to Be Measured in the Proposed Methodology.....	34
<b>Chapter 3 Experiment .....</b>	<b>35</b>
<b>3.1 Introduction .....</b>	<b>35</b>
<b>3.2 Data Acquisition .....</b>	<b>35</b>
3.2.1 Pulse Separation .....	35
3.2.2 Data Acquisition Computer .....	37
<b>3.3 The Getter Phoswich Detector .....</b>	<b>37</b>
3.3.1 Design .....	37
3.3.1.1 Performance.....	38
<b>3.4 The <math>4\pi</math> Phoswich Detector .....</b>	<b>39</b>
3.4.1.1 Design .....	40
3.4.1.2 Construction: Prototype .....	40
3.4.1.3 Construction: Detector.....	42
3.4.1.4 Construction: PMTs and Bases .....	47
3.4.1.5 Performance: Vacuum Testing.....	48
3.4.1.6 Performance: Source Testing .....	48

<b>3.5</b>	<b>2019 <sup>41</sup>Ar Experiment.....</b>	<b>48</b>
3.5.1	Apparatus and Procedure.....	50
<b>3.6</b>	<b>L.L.E. Ride-Along.....</b>	<b>51</b>
3.6.1	Relay Electronics.....	52
3.6.2	Apparatus and Procedure.....	52
<b>3.7</b>	<b>Geant4 Simulations.....</b>	<b>54</b>
<b>Chapter 4 Analysis.....</b>		<b>56</b>
<b>4.1</b>	<b>Introduction.....</b>	<b>56</b>
<b>4.2</b>	<b>2019 <sup>41</sup>Ar Experiment Results.....</b>	<b>56</b>
<b>4.3</b>	<b>L.L.E. Ride-Along.....</b>	<b>59</b>
4.3.1	Assessment of Electronics and Detector.....	59
4.3.1.1	Question 1: Event Binning and Dead-Time Analysis.....	61
4.3.1.2	Question 2: Histogram Shape Over Time.....	64
4.3.1.3	Question 2: Sequential Event Analysis.....	68
4.3.1.4	Question 3: Detector “Warm-Up” Time.....	70
4.3.1.5	Question 4: Possible Background Sources.....	72
<b>4.4</b>	<b>GEANT4 Simulations.....</b>	<b>75</b>
4.4.1	Getter Detector.....	75
4.4.2	4 $\pi$ Detector.....	77
4.4.3	Calculating Expected Decays.....	77
4.4.4	Correcting Crosstalk.....	79
<b>Chapter 5 Conclusion.....</b>		<b>82</b>
<b>5.1</b>	<b>Introduction.....</b>	<b>82</b>
<b>5.2</b>	<b>Summary of Results.....</b>	<b>82</b>
<b>5.3</b>	<b>Future Experiments.....</b>	<b>83</b>
5.3.1	Exploding Wire Experiment.....	83
5.3.2	Second LLE Ride-Along.....	85
<b>5.4</b>	<b>Conclusion.....</b>	<b>85</b>
<b>Appendix A CAD DRAWING OF THE 4<math>\pi</math> PHOSWICH DETECTOR.....</b>		<b>87</b>
<b>Appendix B PMT BASE CIRCUITS.....</b>		<b>88</b>
<b>Appendix C SCHEMATIC FOR THE RELAY ISOLATION CIRCUIT.....</b>		<b>89</b>
<b>Appendix D FEMTODAQ PYTHON CODE RUNNING ON BEAGLEBONE.....</b>		<b>90</b>
<b>Appendix E C CODE USED TO ANALYZE THE PHOSWICH DETECTOR DATA.....</b>		<b>92</b>

## TABLE OF FIGURES

Figure 1. ${}^6\text{Li}(t,p){}^8\text{Li}$ cross-sections as a function of energy .....	10
Figure 2. ${}^2\text{H}(d,n){}^3\text{He}$ cross-section as a function of energy .....	11
Figure 3. Ivy Mike H-bomb detonation.....	12
Figure 4. Gravitational confinement fusion .....	13
Figure 5. Magnetic confinement fusion fields .....	14
Figure 6. Plasma confined within an IEC device .....	15
Figure 7. The process of inertial confinement fusion .....	16
Figure 8 Fusion at the Laboratory for Laser Energetics .....	16
Figure 9. The Laboratory for Laser Energetics and an OMEGA-60 target capsule.....	17
Figure 10. Photo and artist's rendition of the OMEGA-60 laser system.....	17
Figure 11. Timeline of the proposed experiment.....	18
Figure 12. Diagrams of the three proposed trapping methods.....	20
Figure 13. TALYS cross-section predictions.....	23
Figure 14. The Houghton College test chamber .....	24
Figure 15. A simple phoswich detector .....	25
Figure 16. Typical pulses from a phoswich detector system.....	26
Figure 17. Two species of particles in a plasma.....	29
Figure 18. PMT pulse separation circuit.....	36
Figure 19. Traces of the pulses during each step of the pulse separation process .....	36
Figure 20. Final getter detector assembly.....	38
Figure 21. ${}^{207}\text{Bi}$ test run with the getter detector.....	39
Figure 22. ${}^{207}\text{Bi}$ decay scheme and conversion electron spectrum .....	39
Figure 23. Drawing of the $4\pi$ phoswich detector .....	41
Figure 24. The finished acrylic prototype detector .....	42
Figure 25. Cut EJ-212 and EJ-240 scintillator pieces. ....	43
Figure 26. Scintillator box gluing process .....	44
Figure 27. The scintillator before the final assembly .....	45
Figure 28. The finished phoswich detector .....	46
Figure 29. 2-D histogram of a ${}^{207}\text{Bi}$ source produced by the $4\pi$ detector.....	49
Figure 30. Final $4\pi$ detector assembly .....	49
Figure 31. SUNY Geneseo Vacuum System .....	51
Figure 32. The small and $4\pi$ detector detectors outside the LLE target chamber .....	53
Figure 33. Block diagram of electronics for the LLE experiment apparatus .....	53
Figure 34. 2-D histogram of ${}^{41}\text{Ar}$ decay from the $4\pi$ phoswich detector.....	57
Figure 35. ${}^{41}\text{Ar}$ growth curve from an 8 hr counting period with the $4\pi$ detector .....	58
Figure 36. 2-D Histograms from shots 96184, 96188 and ${}^{207}\text{Bi}$ Calibrations .....	60
Figure 37. Improper binning which occurred due FemtoDAQ read-out time.....	61
Figure 38. Decay curves showing dead-time due to FemtoDAQ readout time .....	63
Figure 39. Getter detector decay curves and live-time fraction from shot 96188 .....	64
Figure 40. Time intervals and overlaid histograms.....	66
Figure 41. Shifting and widening of the dE and E histograms in getter detector runs....	66
Figure 42. Shifting and widening of the dE and E histograms in $4\pi$ detector runs .....	67
Figure 43. Sequential difference histograms for shot 96188 with the getter detector ...	68

Figure 44. Sequential difference histograms for ICF shots with the $4\pi$ detector .....	69
Figure 45. Initial start-up of the detectors .....	71
Figure 46. Fitted decay curves for shot 96188 with the getter detector .....	72
Figure 47. Decay diagrams of $^{26}\text{Al}^*$ and $^{16}\text{N}$ .....	74
Figure 48. GEANT4 Getter Detector Rendering .....	76
Figure 49. Getter detector $^{207}\text{Bi}$ simulation comparison.....	76
Figure 50. $4\pi$ Detector simulation .....	77
Figure 51. Experimental data basis and simulation basis.....	80
Figure 52. $4\pi$ detector crosstalk correction comparison.....	81
Figure 53. The exploding wire experiment.....	84

## Chapter 1

### INTRODUCTION

#### **1.1. Introduction to Fusion Research**

At the turn of the 19<sup>th</sup>-century physicists were trying to determine what was the source of the power radiated from the sun. Many theories were proposed, but after the discovery of nuclear reactions, one theory gained traction. Arthur Eddington proposed [1,2] that this energy was produced by hydrogen atoms combining to form helium, as the rest mass of the initial hydrogen atoms is greater than that of the resultant helium atom, suggesting that mass was converted into the emitted energy. Light-ion interactions like this later became known as nuclear fusion.

Studying light-ion interactions such as these is extremely important in the field of nuclear physics. These types of reactions make up what is known as the proton-proton chain (p-p chain) and carbon-nitrogen cycle (C-N cycle), which are the two chief processes by which stars produce energy [3]. Additionally, the hot and dense environment in which these reactions occur is also like the conditions immediately after the Big Bang [4, 5]. A further understanding of these reactions, as well as a measure of their likelihood, can allow for the development of more accurate Big Bang and stellar nucleosynthesis models. The value known as the reaction's cross-section is the quantity that measures the reaction's likelihood and serves as input data for such models.

##### 1.1.1. Measuring Light-Ion Cross Sections

In nuclear physics, a cross-section is a value specific to a certain interaction that is proportional to the probability of the given interaction occurring. Cross-sections allow the determination of how often a certain reaction will occur, which in turn can yield how much of a given product is produced. These values can then be used as input data for statistical models used to predict the likelihood of other reactions and model stellar and post-Big Bang nucleosynthesis.



Experimentally measuring cross-sections is also important for refining existing models. For example, current early-universe nucleosynthesis models overpredict the abundance of  ${}^7\text{Li}$  while underpredicting the abundance of  ${}^6\text{Li}$  [6,7]. This may be because not all sources of  ${}^6\text{Li}$  have been accounted for; the cross-section of the  ${}^3\text{H}(t,\gamma){}^6\text{He}$  reaction, whose product decays into  ${}^6\text{Li}$ , has never been measured at any energy, and is therefore not included in these models. Therefore, this reaction could have a significant but unknown effect on the rate of  ${}^6\text{Li}$  production in the early universe [8]. This lack of data is primarily caused by difficulties in measuring the characteristics of light-ion reactions that have extremely low cross-sections at the very low energies of interest, since the cross-sections decrease rapidly as the energy of the incident particle decreases. Therefore, it is worth examining the method by which these measurements have been traditionally obtained, and possibly considering other methods that do not share the same limitations.

Typically, cross-sections are measured using particle accelerators. Accelerators use electric and magnetic fields to accelerate and focus charged particles into a beam. These particles are then directed into a target, where the beam particles interact with the target nuclei by either scattering off or reacting with the nuclei of the target material. By changing the beam particle and the target material, a wide range of possible interactions can be investigated. Characteristics of the interaction itself, the structure of the incident particles and the target nucleus, and possible nuclear reaction channels can all be studied through generating reactions in this manner.

Though accelerators continue to be frequently used to measure the cross-sections of light-ion reactions, they have certain limitations. One such limitation is that at low energies it is difficult to maintain beam intensity. The Coulomb repulsion between beam ions has a greater effect on the focus and luminosity of the beam at these lower energies. This makes measuring or calculating the target beam current difficult and introduces an energy spread in the beam particles, making them no longer monoenergetic. This makes calculating a cross-section at a specific energy difficult and is another source of error when measuring low energy (keV range) reactions.

Another limitation of particle accelerators is that they are relatively slow in generating low-likelihood reactions. Accelerator beam currents are typically from 1 to 100 microamperes, which corresponds to anywhere from a few trillion to a few 100 trillion particles per second moving down the beamline. Though these seem like large numbers, for some reactions with small cross-sections, the amount of time needed to obtain a statistically significant number of reactions makes the use of an accelerator impractical. For example, a 1  $\mu\text{A}$  beam of tritons hitting a 0.016 mm thick  ${}^7\text{Li}$  foil (beam particles lose energy as they travel through the foil, so to reduce the energy spread that this introduces, a very thin foil is used) at 18.3 keV (the average ion temperature used for the ICF calculations in Table 1) will take roughly 2,800 years to accumulate 1,000,000 occurrences of the  ${}^7\text{Li}(t,\alpha){}^6\text{He}$  reaction. Such a long experiment is not feasible. This issue often results in an absence of cross-section data below a few hundred keV for most reactions. Figure 1 shows an example of a reaction with no cross-section data below 2 MeV. This issue has also led to some rare light-ion reactions, such as the previously mentioned  ${}^3\text{H}(t,\gamma){}^6\text{He}$  reaction, having never been measured at any energy. The cross-section of light-ion reactions decreases as the energy of the incident particle decreases, as seen in Figure 2.

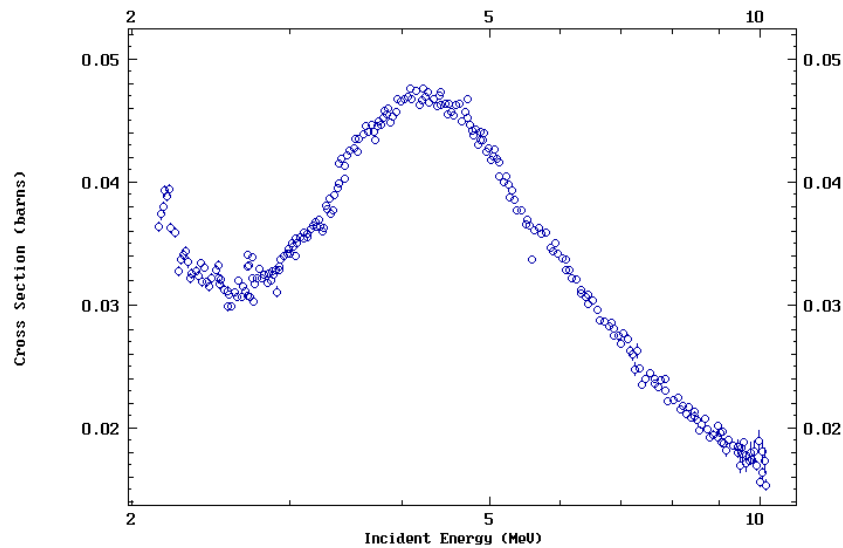


Figure 1.  ${}^6\text{Li}(t,p){}^8\text{Li}$  cross-sections as a function of energy. The  ${}^6\text{Li}(t,p){}^8\text{Li}$  reaction is an example of a light ion reaction lacking cross-section data below a few MeV. Plot constructed using National Nuclear Data Center (NNDC) EXFOR [9] and data from Ref. [10] extracted from the National Nuclear Data Center NuDat 2 database [11].

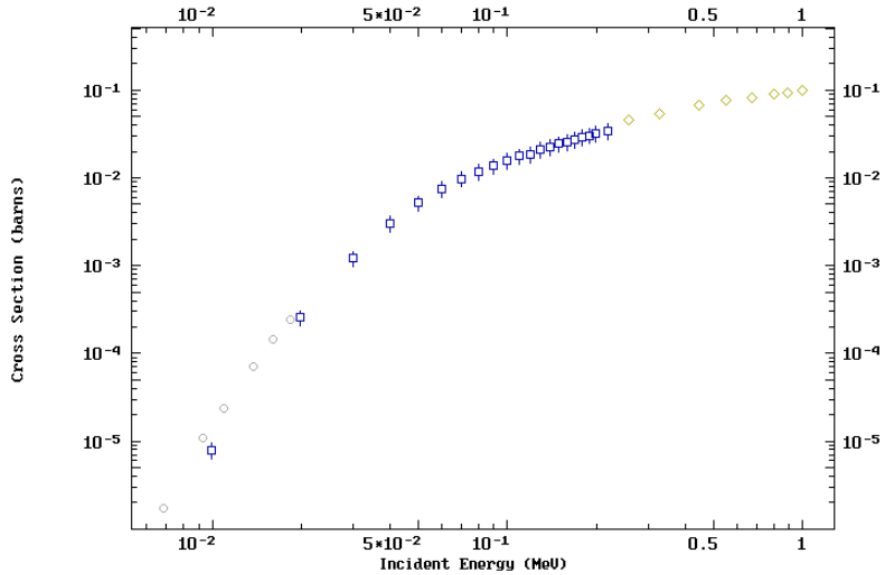


Figure 2.  ${}^2\text{H}(d,n){}^3\text{He}$  cross-section as a function of energy. The  ${}^2\text{H}(d,n){}^3\text{He}$  is a well-studied reaction due to it being one of the fundamental reactions present in D-D fusion. Like many light-ion fusion reactions, its cross-section decreases sharply as the energy of the incident particle decreases. Plot constructed using EXFOR [9] and NNDC [11] with data from Ref. [12,13,14].

This sharp decrease in cross-section makes measuring the reactions difficult, since they are less likely to occur, separation of background from the good data becomes difficult. This issue is easily solved by increasing the number of incident and target particles to ensure more reactions occur, however, this is difficult to do with accelerators due to the aforementioned limitations on beam intensity.

Moreover, because they could take place in stellar fusion, tritium-induced reactions are of special interest. However, this exposes another limitation of accelerators, as tritium can easily permeate into most materials used in the construction of accelerator beamlines, eventually forcing operators to decommission equipment, or go through lengthy and expensive cleaning procedures, to remove contamination [15][16]. For this reason, no accelerator labs currently allow triton beams, and very few allow the production of secondary tritons.

These limitations have created the need to develop a more efficient way of creating low-energy, light-ion reactions for fundamental nuclear research.

## 1.2. *Thermonuclear Reactions and Fusion*

One method that could produce many nuclear reactions on a timescale that is feasible for a laboratory is to use a thermonuclear process. A thermonuclear process occurs when the temperature of a plasma containing the reacting ions is high enough for nuclear reactions to occur at significant rates. An event known as ignition is achieved when the energy liberated in the reactions is sufficient to create a chain reaction. This chain reaction could either be controlled or uncontrolled.

### 1.2.1. Uncontrolled Thermonuclear Fusion

Uncontrolled thermonuclear fusion is when the nuclear fuel (usually a mix of tritium and deuterium for fusion reactions) is heated and compressed, but the plasma is not confined to any specific volume. The energy released during the fusion reactions then causes the plasma to expand rapidly and violently. The most famous example of uncontrolled thermonuclear fusion is found in the hydrogen bomb. The first hydrogen bomb was detonated during the Operation Ivy “Mike” test, pictured in Figure 3 [17]. Though energies on the scale of tens of petajoules can be released, such an event cannot be safely and sustainably repeated in a laboratory.

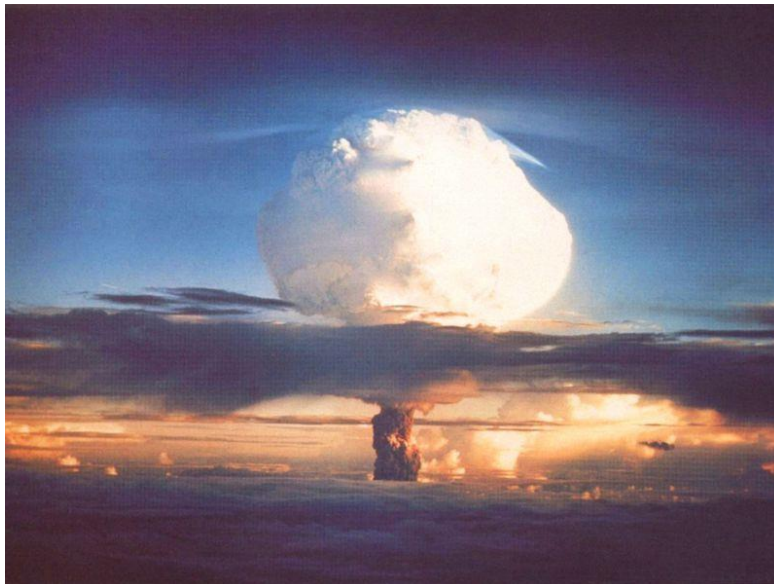


Figure 3. Ivy Mike H-bomb detonation. On November 1<sup>st</sup>, 1952, the United States Military detonated the first hydrogen bomb. A hydrogen bomb is an example of uncontrolled thermonuclear fusion. Figure taken from Ref [18].

### 1.2.2. Controlled Thermonuclear Fusion

In a laboratory setting, there must be a force that confines the plasma for a long enough time at a high enough number density and temperature for a significant number of fusion reactions to safely occur. The quantity that is used to assess these confinement requirements, which compares the energy generated in the reactions to the energy lost to the environment, is known as the Lawson Criterion [19]. Fortunately, plasma, unlike most substances at room temperature, is electrically conductive and is composed of individual charged particles, as the temperature of the plasma causes the nuclei of the contained atoms to be stripped of their electrons. This allows the plasma to be strongly influenced by external magnetic and electric fields. For this reason, electric, magnetic, or gravitational fields can be used to confine the plasma.

#### 1.2.2.1. Gravitational Confinement Fusion

One way to confine the plasma is with a strong gravitational field, such as those present within stars. Due to the immense weight of stellar material, the center of a star is compressed, reaching temperatures and pressures needed to produce fusion reactions, shown in Figure 4. This process is known as gravitational confinement fusion, and it is responsible for the natural generation of all the elements between hydrogen and iron. However, the mass needed to supply a strong enough gravitational force is so large that gravitational confinement fusion is only found within stars [3].

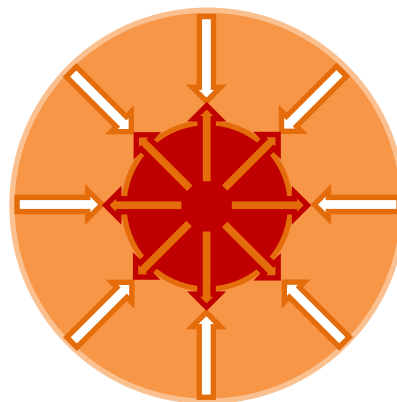


Figure 4. Gravitational confinement fusion. The weight of the outer layers of a star compresses and confines the inner layers for extremely long periods of time. As fusion occurs, the released energy raises the temperature of the fuel, creating an outward pressure that prevents further compression.

### 1.2.2.2. Magnetic Confinement Fusion

Another method for confining the plasma is known as magnetic confinement fusion (MCF). The most common design of an MCF machine is the tokamak. These machines are composed of a toroidal chamber wrapped with coils that produce a toroidal magnetic field lines inside the chamber. The reasoning behind this design is as follows. Charged particles travelling in a uniform magnetic field generated by a solenoid follow helical paths about the field lines, which prevents particles from drifting towards the walls of the solenoid. However, the particles may still travel out of the ends. The solution to this problem is to bend the solenoid into a torus, so that the particles cannot leave the inner volume. However, a toroidal solenoid has a stronger magnetic field near its center, which eventually causes particles to drift and collide with the inner walls of the torus. However, producing helical fields, while not completely solving this problem, has been shown to confine particles for sufficient times [20, 21]. A basic diagram of these fields is shown below in Figure 5. Currently, multiple nations around the world are collaborating in the construction and design of ITER. ITER will use a tokamak design and aims to be the first fusion experiment to reach ignition and become net energy positive, meaning that it will generate more energy than was put into it. Once completed, ITER will be the world's largest MCF experiment [21].

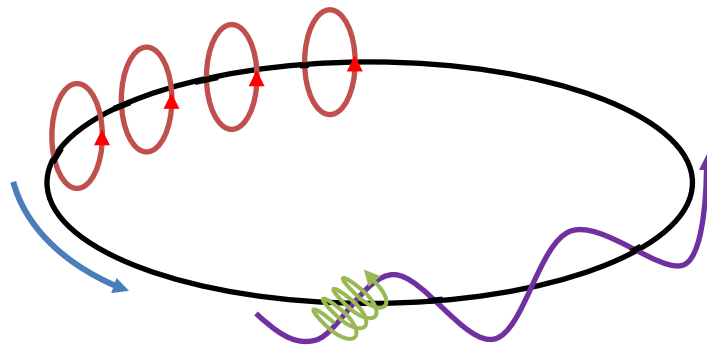


Figure 5. Magnetic confinement fusion fields. Magnetic fields are used to confine and compress the plasma, allowing the plasma to reach temperatures and pressures needed for fusion to occur. The blue field represented the toroidal field created by the toroidal currents driven around the beam chamber; the red fields represent the poloidal fields, created by the current within the plasma, that encompass the beamline; and the purple field represents the resultant helical field, which is the sum of the poloidal and toroidal fields (all fields extend symmetrically around the entire circular beam path). Particles travel in a helical path (green), spiraling around the helical (purple) field lines.

### 1.2.2.3. Inertial Electrostatic Confinement Fusion

Another way to induce fusion on a laboratory scale is using strong electric fields. This is called inertial electrostatic confinement fusion (IEC). One example of an IEC device is the Farnsworth fusor. In this type of fusor, a large potential difference (on the order of 10s of kV) is placed across spherical electrodes, creating a large electrostatic potential well at the center of the fusor, this traps charges and therefore confines the plasma within the well [22]. Houghton College is currently developing a Farnsworth fusor to induce deuterium-tritium (D-T) fusion. An example of such an assembly is shown in Figure 6.



Figure 6. Plasma confined within an IEC device. Using a large voltage on a spherical cathode grid, a large potential well can be created at the center of a vacuum chamber, confining the charged particles that compose the plasma and allowing for fusion to occur. Figure taken from Ref. [23].

### 1.2.2.4. Inertial Confinement Fusion

Another method of confining a plasma is by imparting a large amount of energy into a small capsule of fuel in a short period of time. This can be done by bombarding it with beams of particles or laser light. This causes the outer layer of the outer layers of the capsule to ablate and expand outward rapidly, exerting a reaction force on the fuel within the capsule. This pressure shockwave can then travel through the capsule, producing the conditions needed for fusion in an extremely short period of time at the center. This process is known as inertial confinement fusion and is shown in Figure 7.

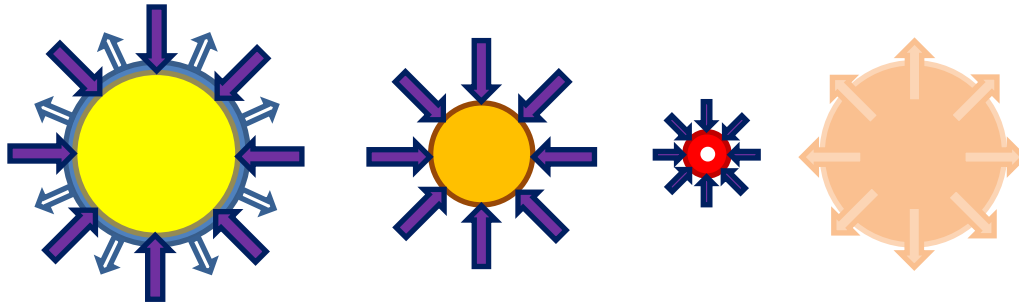


Figure 7. The process of inertial confinement fusion. (1) The lasers hit the capsule, heating the capsule walls and causing them to ablate. (2) The fuel within the capsule compresses due to the inward force exerted by the ablating material. (3) After being accelerated inwards, the fuel implodes and becomes dense enough and hot enough for fusion reactions to begin. (4) After the implosion, the plasma filled with the products of the fusion reactions expands and thermalizes.

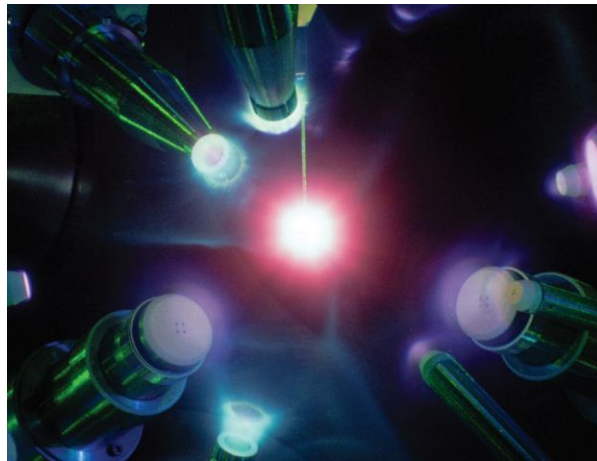


Figure 8 Fusion at the Laboratory for Laser Energetics . After the energy is delivered to the capsule within the OMEGA-60 target chamber, fusion reactions begin. This releases energy in the form of various wavelengths of light and fast-moving particles. Figure taken from Ref. [4].

The three largest ICF facilities in the world are the Laboratory for Laser Energetics (LLE) in Rochester, NY (Figure 9, Figure 10) [24, 25]; the National Ignition Facility (NIF) in Livermore, CA [26]; and Laser Mégajoule (LMJ) in Bordeaux, France [27]. The largest of these facilities is the NIF, but the facility that is most closely related to the work conducted at Houghton College is LLE. The primary laser system of LLE is the 60-beam OMEGA laser system, capable of delivering up to 30 MJ of energy to a target that is about 1 mm in diameter [4] (Figure 8). One distinct feature of LLE is its identity as a user group facility. This means that the facility serves as a collaboration space and experimental setting for a diverse community of research groups. LLE has access to a wide range of modular diagnostics and possible experimental



configurations, allowing many different experiments and types of measurements to occur. Such a facility allows for new experimental methods and diagnostics to be tested alongside operations focusing on fusion science experiments. These side tests are called ride-along experiments and allow smaller research groups to carry out research that would normally not be granted facility shot time.



Figure 9. The Laboratory for Laser Energetics and an OMEGA-60 target capsule. (Left) The Laboratory of Laser Energetics (LLE) located in Rochester, NY is the second largest inertial confinement facility in the United States. (Right) Target capsules that are filled with the fusion fuel measure only 1 mm in diameter. Figures taken from Ref. [4]

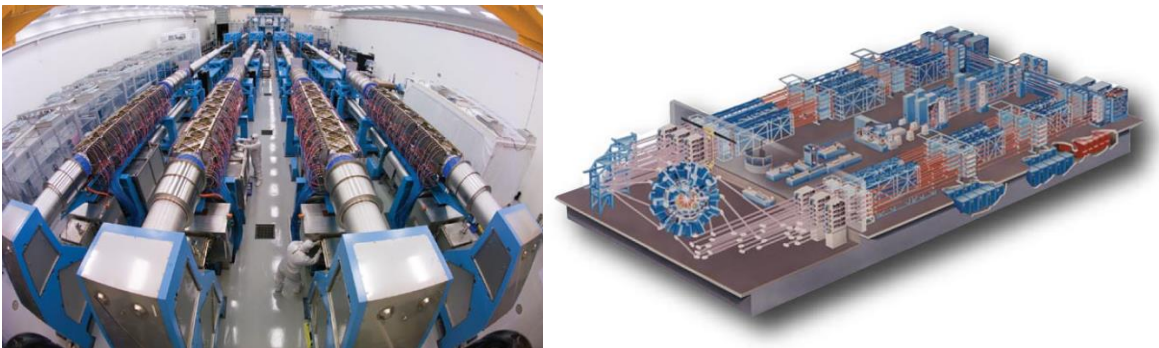


Figure 10. Photo and artist's rendition of the OMEGA-60 laser system. (Left) a photo of the OMEGA-60 laser system, and (right) an artist's rendition. The laser guides and focusing arrays of the OMEGA-60 laser system at LLE has a footprint the size of a football field. A single laser pulse is generated and is then split and amplified many times over before being redirected to the spherical target chamber. Figures taken from Ref. [4].

### 1.2.3. ICF as a Tool to Measure Light-Ion Fusion Cross Sections

Because in ICF a macroscopic quantity of nuclear fuel is raised to temperatures at which nuclear reactions begin to occur, ICF could be used to study low energy, light-ion reactions

in a short amount of time. For example, by using ICF to initiate a thermonuclear implosion, 1,000,000  ${}^7\text{Li}(t,\alpha){}^6\text{He}$  reactions at a temperature of 18.3 keV could be created within a nanosecond, as opposed to the 2,800 years needed for 1,000,000 reactions with a typical accelerator (recall Section 1.1.1). Another benefit is that all ICF facilities are equipped to handle tritium, since it is a component of the nuclear fuel used in most experiments. Facilities have systems designed to scrub tritium from the vacuum system [8]. This makes ICF laboratories one of the few places where tritium-induced reactions can be studied.

### 1.3. The Experiment

While ICF implosions have the capability of producing these low-cross-section, light-ion reactions, neutrons from D-D, DD-T, and T-T fusion, as well as prompt gamma rays from inelastic neutron scattering and delayed gamma rays from neutron activation will all contribute to a very high background rate immediately after the shot. Reducing the background and the damage to detectors and electronics from the EMP and primary neutrons is key to finding an accurate count of the desired reactions. For this reason, a method that will measure the decays of product nuclei in the milliseconds after the implosion, a comparatively long time after the initial flux of background particles and radiation, is proposed. Figure 11 shows a timeline of the proposed experiment.

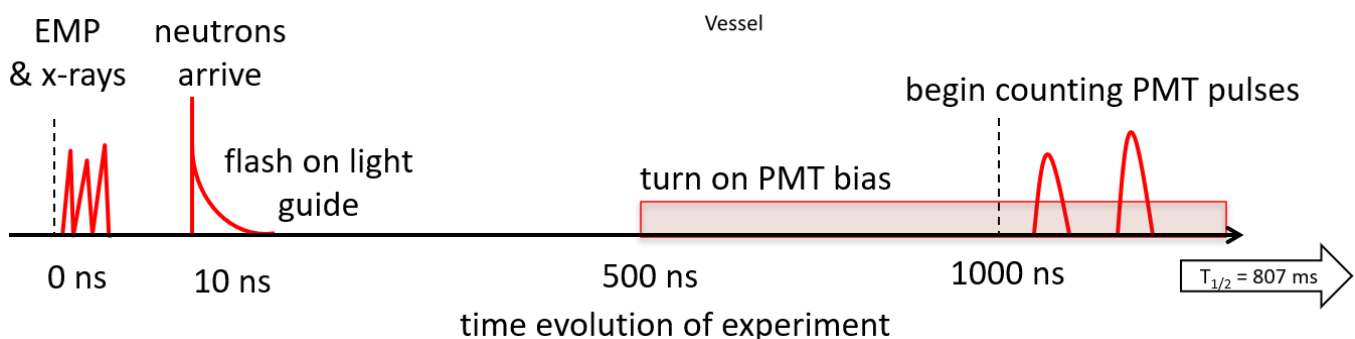


Figure 11. Timeline of the proposed experiment. Shown above is the timeline of the proposed experiment, referencing, as an example, the half-life of  ${}^6\text{He}$ , which could be created through the  ${}^3\text{H}(t,\gamma){}^6\text{He}$  reaction, whose cross-section has never been measured at any energy. By waiting to turn on the detector until after the initial EMP and flux of gammas and neutrons, the measurement can be made in an environment with less background. Most current experiments at ICF facilities measure primary radiation released immediately after the shot, rather than secondary radiation released by reaction products.

This means that the reactions that could be measured using this method are reactions that produce radioactive products with half-lives on the order of tens of milliseconds to 10 s. This time scale allows for the initial background from prompt radiation to decrease but is shorter than the longer half-lives of most neutron activation products created in the surroundings after the implosion. A brief timeline of the experiment is as follows:

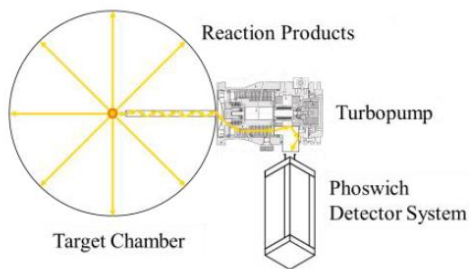
1. The control room signals to the apparatus that the shot has occurred, and the apparatus then waits a configurable amount of time (until step 4) before powering the detector and connecting the detector signal to the processing electronics.
2. Immediately following the shot the fuel capsule is compressed and heated by the lasers (as described in Section 1.2.2.4) and fusion reactions begin to occur. Then the EMP and primary gamma and neutron radiation from the implosion are emitted.
3. After fusion reactions cease, the plasma begins to thermalize, expanding outward into the chamber, cooling, and recombining.
4. The expanding neutral gas is trapped within a collection system where counting of the decays of the desired products contained within the gas can then begin.

In order to count the desired reaction products, a mechanism is needed to capture a fraction of the expanding neutral gas mixture while simultaneously measuring the decays of its constituents. After a fraction of the gas is trapped and decays are identified and counted as a function of time, the number of counts and the collection fraction, which will both be measured, can be used to determine how many of a given product nucleus was created. This can then be used to calculate the reactivity, which is the cross-section integrated over the thermal velocity distribution, for a given reaction (this calculation is discussed further in Chapter 2).

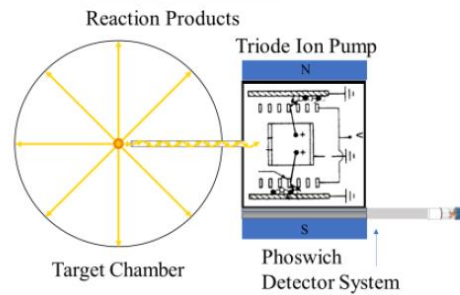
Two methods of trapping the expanding neutral gas after the shot are being considered (Figure 12). Both collection methods are to be tested on a small scale to estimate a collection fraction (an experiment designed to measure the collection fraction of each method can be found in Chapter 5).

1. A long collection tube would be affixed to the intake of a turbopump or ion pump, and the open end placed a short distance from Target Chamber Center (TCC) (a few cm away from the target capsule). A fraction of gas would then travel down the tube as it is expanding and become trapped in the foreline of the turbopump or embedded in the wall of the ion pump, where the decays can be counted.
2. A chemical getter would be used that would allow the more chemically reactive products to stick to a surface affixed to the detector system, where they can then be counted.

### Turbopump System



### Ion pump System



### Getter System

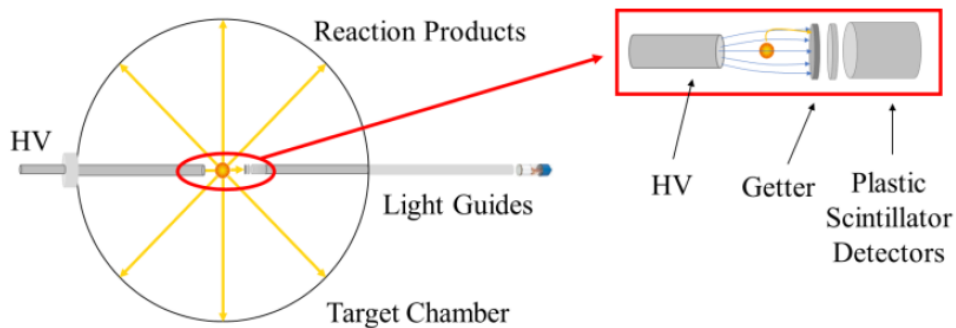


Figure 12. Diagrams of the three proposed trapping methods. (Top) The first proposed method uses a collection tube placed within a few centimeters of the target chamber's center (TCC). A turbopump (left) or ion pump (right) is attached to the end of the collection tube and traps the expanding gas as it travels down the tube. The gas will then be expelled by the turbo pump into a trap, or embedded within the wall of the ion pump, where a phoswich plastic scintillator detector will measure the beta decay of the products. (Bottom) The second method, which could be used for measuring the decay of chemically reactive products, uses high voltage to accelerate ions (before the gas thermalizes) towards a getter where they become trapped. A light guide then transfers the light produced by the scintillator to an external photomultiplier tube (PMT).

Evacuating the entire chamber after the event using the large cryopumps in the OMEGA-60 system was also considered. However, previous work [28] has shown that it would take about 90 s to completely evacuate the product gas after the shot. An evacuation time of 90 s is considerably longer than many of the products' half-lives, so this method is not feasible.

The reactions of interest would result in products which beta decay with a half-lives from tens of milliseconds to a few seconds. These comparatively longer half-lives allow for a significant fraction of the products to remain by the time counting starts. The desired reactions could be created by doping a deuterium, tritium, or D-T filled capsule with the relevant isotopes (a fraction of 1% dopant is assumed in Table 1). Using TALYS [29] and S-factor extrapolations from Ref. [30] (the S-factor extrapolation is explained in greater detail in Section 2.4.1.1), a code designed to extrapolate the cross-section of a reaction from pre-existing data (further discussed in Section 2.4.1.2), the predicted yields of several light-ion fusion reactions have been estimated in Table 1. The exception to this is the  ${}^3\text{H}(t,\gamma){}^6\text{He}$  reaction, whose cross-section has never been measured at any energy and has a target mass  $A < 5$ , which prevents using TALYS to extrapolate a cross-section. Additionally, TALYS calculations are plotted alongside data for several measured reactions in Figure 13.

### 1.3.1. Previous Work at Houghton

To date, a small-scale apparatus has been built that can be used to test possible product trapping and decay counting methods. A test vacuum chamber fitted with a fast release valve multiple small ion gauges, and turbopump and getter traps was constructed to release, track, and trap radioactive gases (Figure 14). During the summer of 2019,  ${}^{41}\text{Ar}$  was produced at SUNY Geneseo using a tandem pelletron accelerator via the  ${}^{40}\text{Ar}(d,p){}^{41}\text{Ar}$  reaction. This gas was then transported to Houghton College and released via the fast valve into the test vacuum chamber. A turbopump then trapped the expanding gas that travelled down a collection tube, allowing the  ${}^{41}\text{Ar}$  decays to be counted using a silicon surface barrier detector, NaI detector, and a HPGe detector. The decay of  ${}^{40}\text{Ar}$  was identified and the measured half-life calculated agreed with the accepted value of 109.61 min.

Table 1. Product half-life, reactant natural abundances, and predicted yields for several light ion reactions that may be studied using ICF. The predicted yields are based on the yield of OMEGA shot 77951 which was a tritium-filled SiO<sub>2</sub> capsule “exploding pusher” having a 1.5%-98.5% DT mixture and reaching an ion temperature of 18.3 keV. Reactivities were calculated using TALYS-1.9 [29] and the S-factor extrapolations of Abramovich et. al. [30]. No cross sections are available for <sup>3</sup>H(t,γ)<sup>6</sup>He so the predicted yield is based on assuming a branching ratio of 10<sup>-7</sup>, which is simply an estimated “best case”. For <sup>11</sup>B(d,p)<sup>12</sup>B and <sup>15</sup>N(d,p)<sup>16</sup>N for which data are available at higher energies, TALYS underpredicts the cross-sections by as much as a factor of 100 (view Figure 13). The reactions in gold are best suited for the OMEGA-60 laser system, while the reaction in green would become feasible if the yield were increased be 100-1000 times, such as at the NIF.

Reaction	Product Half-life	Reactant Abundance	Predicted Yield
<sup>3</sup> H(t,γ) <sup>6</sup> He	807 ms	<sup>3</sup> H fill	8×10 <sup>4</sup>
<sup>6</sup> Li(t,p) <sup>8</sup> Li	840 ms	7.6%	0.2-1×10 <sup>7</sup>
<sup>7</sup> Li(t,α) <sup>6</sup> He	807 ms	92.4%	0.7-2×10 <sup>6</sup>
<sup>9</sup> Be(t,α) <sup>8</sup> Li	840 ms	100%	5×10 <sup>5</sup>
<sup>9</sup> Be(t,γ) <sup>12</sup> B	20.2 ms	100%	18
<sup>10</sup> B(t,p) <sup>12</sup> B	20.2 ms	19.9%	5770
<sup>11</sup> B(d,p) <sup>12</sup> B	20.2 ms	80.1%	534
<sup>13</sup> C(t,γ) <sup>16</sup> N	7.1 s	1.1%	1
<sup>13</sup> C(t,α) <sup>12</sup> B	20.2 ms	1.1%	677
<sup>13</sup> C(t,p) <sup>15</sup> C	2.45 s	1.1%	111
<sup>14</sup> N(t,p) <sup>16</sup> N	7.1 s	99.6%	16
<sup>15</sup> N(d,p) <sup>16</sup> N	7.1 s	0.4%	0.15

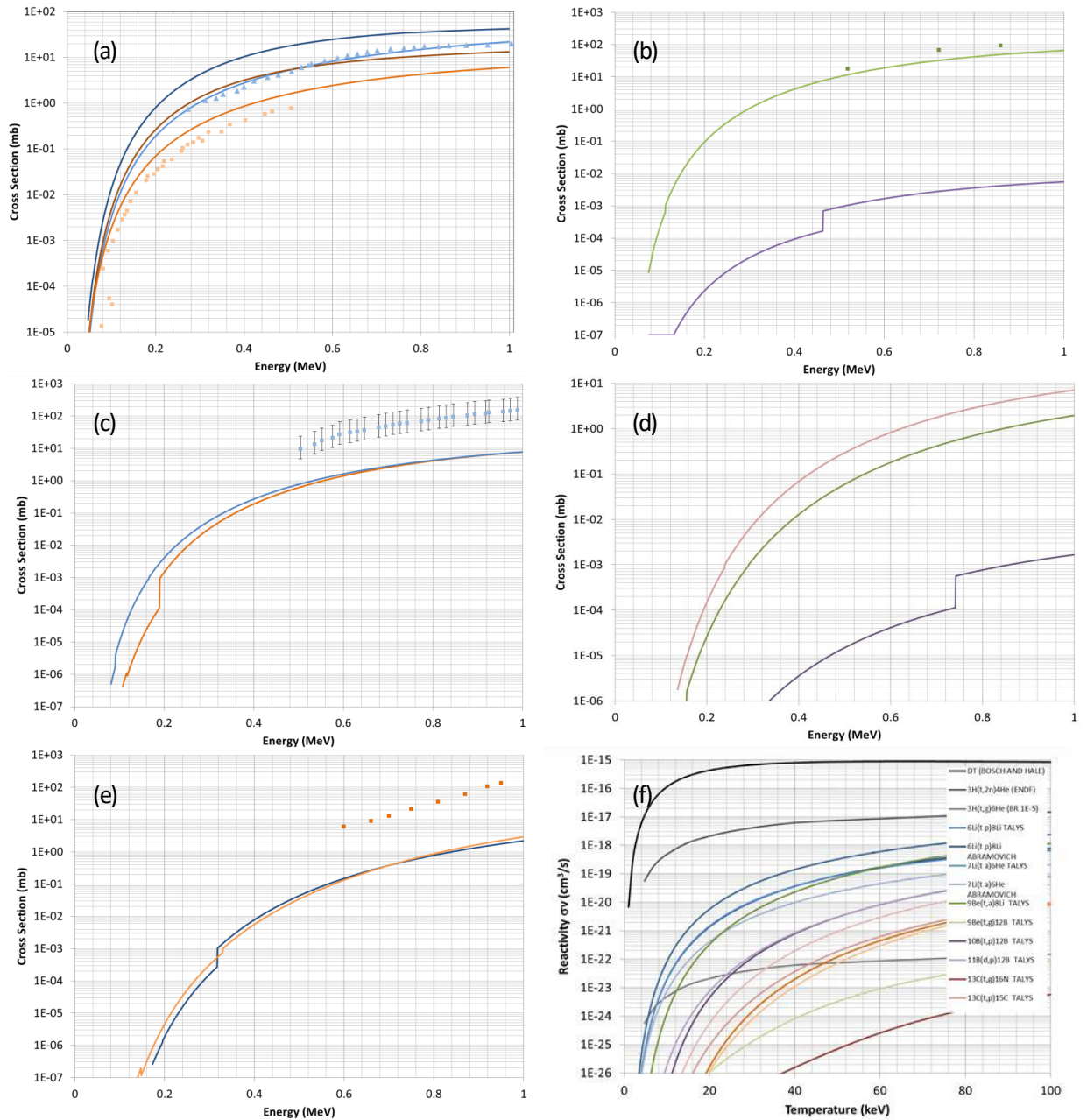


Figure 13. TALYS cross-section predictions. (a) Cross sections for  $^6\text{Li}(t,p)^8\text{Li}$  predicted by TALYS (dark blue curve), S-factor [30] (light blue curve) and measured [31] (light blue triangles), and for  $^7\text{Li}(t,\alpha)^6\text{He}$  predicted by TALYS (dark brown curve), S-factor [30] (orange curve) and measured [31, 32] (orange squares). (b) Cross sections for  $^9\text{Be}(t,\alpha)^8\text{Li}$  predicted by TALYS (green curve), and measured [33] (green squares), and for  $^9\text{Be}(t,\gamma)^{12}\text{B}$  predicted by TALYS (purple curve). (c) Cross sections for  $^{10}\text{B}(t,p)^{12}\text{B}$  predicted by TALYS (orange curve), and for  $^{11}\text{B}(d,p)^{12}\text{B}$  predicted by TALYS (blue curve) and measured [34] (blue squares). (d) Cross sections for  $^{13}\text{C}(t,p)^{15}\text{C}$  (green),  $^{13}\text{C}(t,\gamma)^{16}\text{N}$  (purple) and  $^{13}\text{C}(t,\alpha)^{12}\text{B}$  (pink) predicted by TALYS. (e) Cross sections for  $^{14}\text{N}(t,p)^{16}\text{N}$  predicted by TALYS (blue curve), and for  $^{15}\text{N}(d,p)^{16}\text{N}$  predicted by TALYS (orange curve) and measured [35] (orange squares). (f) Reactivities calculated by integrating Equation (2.7) for each of the predicted cross sections.



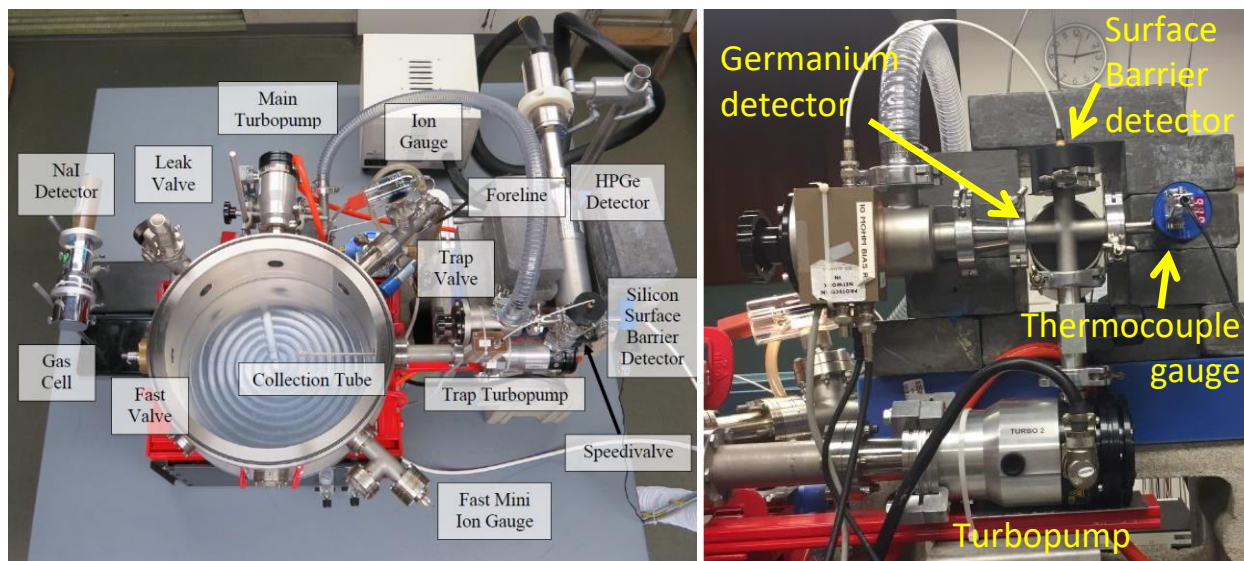


Figure 14. The Houghton College test chamber. The test chamber was used to test methods of collecting and measuring the decay of radioactive gases.

In another experiment, which occurred during the summer of 2018,  ${}^6\text{He}$  was created via the  ${}^9\text{Be}(n,\alpha){}^6\text{He}$  reaction and its decay was also identified and measured. These experiments are described in Ref. [36]. Having shown that it was feasible to trap and detect gaseous radioactive isotopes, efforts then turned towards developing a detector that could identify the incident particles.

## 1.4. Current Progress

### 1.4.1. Phoswich Detector System

As shown later in Table 1, it is predicted that, depending on the reaction being observed, only as many as  $10^7$  desired reactions might be expected in a high-yield ICF shot. However, the neutron flux generated after the shot activates nuclei in the environment, leading to large amounts of secondary radiation. For this reason, a detector system was needed that could identify the incident particles, so that the desired decay can be seen amidst the background decays present. This would allow for events with desired characteristics to be selected, reducing the background. This motivated the selection of a dE-E detector.

A dE-E detector was chosen because it has the ability to identify particles based on their total kinetic energy and the rate they lose kinetic energy while travelling through a medium. The basic design of the dE-E detector in this work has been a phoswich configuration, which



consists of two layers of plastic scintillator optically coupled together. The first layer, known as the “fast”, “thin”, or “dE” layer consists of a thin (compared to the E layer) layer of a plastic scintillator that has a relatively quick decay time, usually on the order of nanoseconds. This layer is then coupled to the second layer, known as the “slow”, “thick”, or “E” layer with a longer decay time, usually on the order of hundreds of nanoseconds. The coupled scintillators are then optically coupled to a photomultiplier tube (PMT), where the light pulse is converted into a current pulse that can be digitally recorded and analyzed. Shown in Figure 15 is a simple phoswich detector that can be optically coupled to a PMT.

#### 1.4.2. Particle Categorization with a Phoswich Detector System

The process of identifying the particle incident on the detectors is dependent on the light pulses generated as the particle passes through the two layers of scintillator. When passing through the thinner dE layer, the particle typically loses only a small fraction of its energy, and the pulse generated is typically on the order of tens of nanoseconds wide with a peak height of about 100 mV, depending on the gain of the PMT. When passing through the E layer, the particle typically deposits the rest of its energy, producing a longer pulse on the order of hundreds of nanoseconds with a peak of around 80 mV

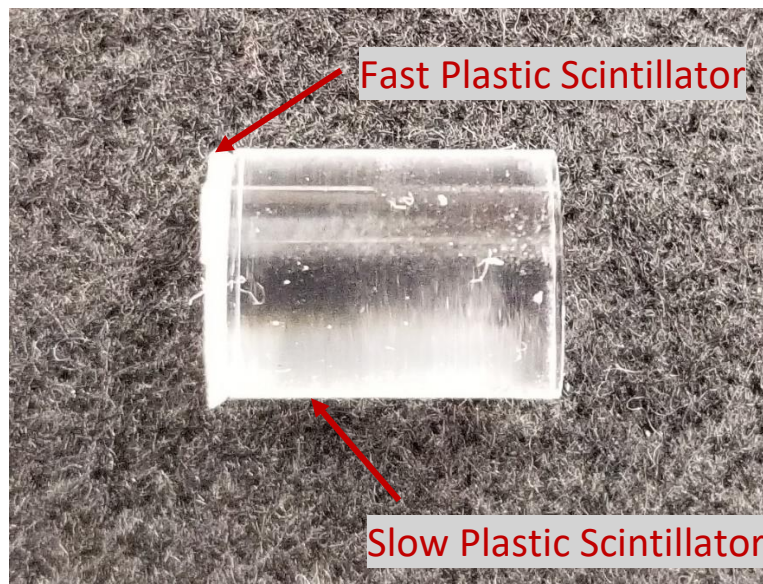


Figure 15. A simple phoswich detector. A thin layer of plastic scintillator with a fast decay time is coupled to a thicker layer of scintillator with a much slower decay time.

Together, these form a resultant pulse which has a short rise time and sharp peak, followed by a slowly decaying, long tail. Figure 18 shows examples of the shape and approximate size of pulses outputted by a phoswich detector system.

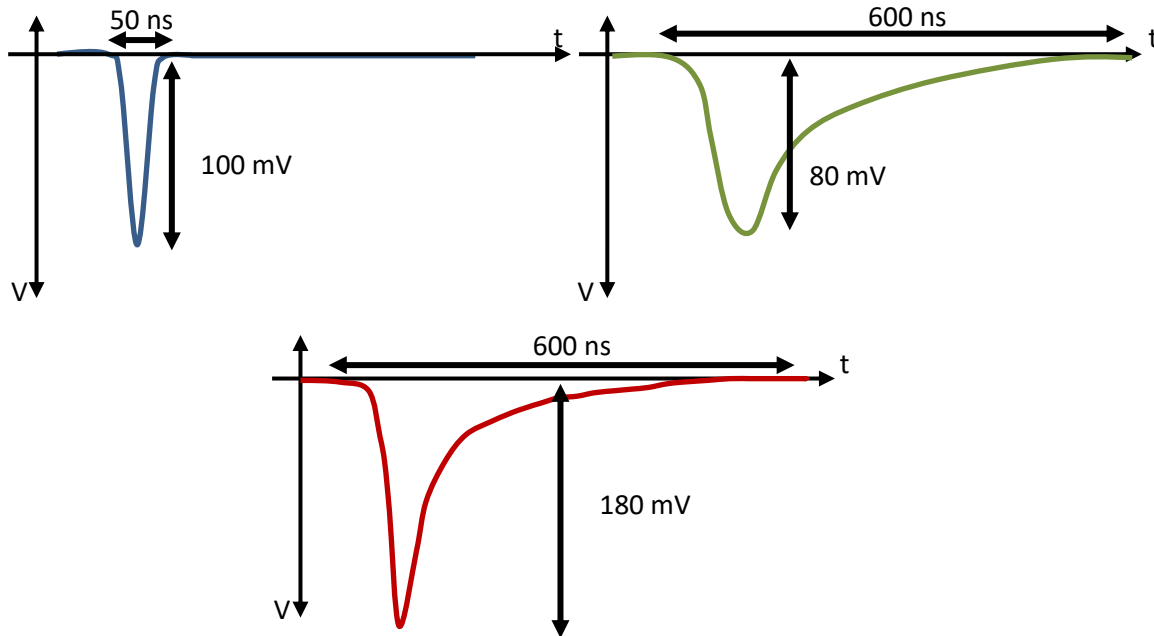


Figure 16. Typical pulses from a phoswich detector system. As a particle passes through the dE layer, a sharp, short-duration negative voltage pulse is produced (blue). As a particle passes through the E layer, a shorter and longer pulse is produced (green). These two pulses sum together to give the resultant pulse: a sharp peak followed by a long tail (red).

The major advantage of this system is that, assuming the particle has stopped within the detector, the pulse height of the fast, dE pulse is proportional to the rate at which the particle loses kinetic energy, while the pulse height of the slow, E pulse is proportional to the total kinetic energy of the particle. By separating the sum pulse into its constituent dE and E components different particles can be identified based on how fast they deposit energy and how much energy they had. For example, an  $\alpha$  particle has a charge of  $2e$ , which causes it to strip electrons from nuclei within the detector and lose energy rather quickly. This produces a large dE pulse for a given energy. beta particles, due to their smaller charge of  $1e$ , and much smaller mass, interact with the detector by scattering off of bound electrons (potentially ionizing them) and nuclei. Due to a beta particle's comparatively small mass, it loses energy rather slowly, allowing it to travel further into the detector. Most of its energy is then in

the thicker E layer, depending on the angle the beta particle entered the detector. However, gammas and neutrons have no charge, and will therefore interact with the detector in a different manner. Gammas will interact either by Compton scattering or through the photoelectric effect while neutrons will interact by scattering off nuclei within the detector. Because of its larger volume, these interactions are more likely to occur in the thick layer of the detector, so typically only an E pulse would be generated.

#### 1.4.3. The $^{41}\text{Ar}$ Experiment and the LLE Ride-Along Experiment

Two separate phoswich detectors have been constructed and tested: the “getter” detector consisting of the two layers of scintillator pictured in Figure 15 coupled to a 1.5” PMT which can be used in the getter-based collection method, and a turbopump trap detector in the form of a hollow box with a solid angle of  $4\pi$ , coupled to a 5” PMT. During the summer of 2019, the  $4\pi$  detector was filled with  $^{41}\text{Ar}$  created via the  $^{40}\text{Ar}(d,p)^{41}\text{Ar}$  reaction using SUNY Geneseo’s tandem pelletron accelerator. The purpose of this experiment was to test if the decay of a radioactive, inert gas contained within the  $4\pi$  detector’s inner volume could be detected and identified. This experiment is described in further detail in Section 3.5 and the results are presented in Section 4.2.

After the test of the  $4\pi$  detector system at SUNY Geneseo, a ride-along experiment was performed at LLE with the goal of testing the behavior of the  $4\pi$  detector and electronics in the time immediately following an ICF implosion, testing the functionality of the circuit isolating the electronics until counting can begin, and obtaining a preliminary count of the secondary radiation in the target chamber environment following the implosion.

## Chapter 2

### THEORY

#### **2.1. Introduction**

Once the decays from the desired products have been identified and counted, steps can be taken towards calculating the cross-section for the desired reaction. To perform these calculations, the concept of a cross-section and its relation to the yield of a given reaction must be more rigorously established. In this chapter, the cross-section will be defined, and values will be estimated for several nuclear reactions occurring between two species of particles in a plasma. Additionally, possible light-ion reactions that could be measured with the proposed methodology will be discussed.

#### **2.2. Cross Sections**

As stated previously, the cross-section of a nuclear reaction is proportional to the probability of the given reaction occurring. In inertial confinement fusion, these reactions occur within a hot and dense plasma. To fuse, nuclei must have enough kinetic energy to become close enough for the strong force to overcome the repulsive Coulomb force. Classically, this would require much more energy than is observed. However, due to quantum mechanical effects, nuclei may tunnel through the Coulomb potential barrier, allowing reactions to occur at much lower energies.

Consider  $N_1$  nuclei of species  $S_1$ , with number density  $n_1$ , interacting in a plasma with  $N_2$  nuclei of species  $S_2$ , with number density  $n_2$ , as shown in Figure 17. As species  $S_1$  moves at speed  $v$  through the region containing species  $S_2$ , it takes a short time  $t$  to cover a tiny distance  $d$ . Therefore, the tiny volume  $V = Avt$  is the volume of  $S_2$  nuclei that  $S_1$  nuclei will interact with in time  $t$ . These parameters are chosen to be small so that the number densities of each species of nuclei, as well as the velocity of  $S_1$  can be assumed to be constant within  $V$ . It is expected that the number of total interactions  $N$  between the two species in time  $t$  is proportional to the number of particles in each species,  $N_1$  and  $N_2$ . Additionally, the total

number of interactions  $N$  between the two species would be inversely proportional to the cross-sectional area  $A$  of the volume  $V$  of  $S_2$  particles that can be interacted with.

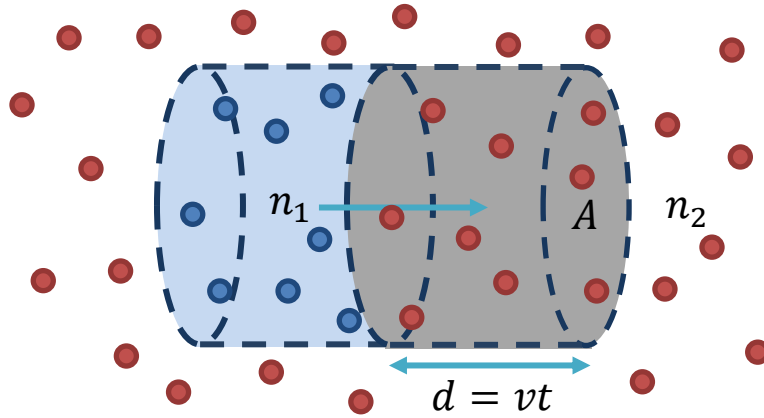


Figure 17. Two species of particles in a plasma. Particle species  $S_1$  (blue) of number density  $n_1$  in the light blue volume moves with a speed  $v$  in the lab frame through a target species  $S_2$  (red), with number density  $n_2$  that is stationary in the lab frame, into the tiny cylindrical grey volume with a tiny base area of  $A$ .

This is because, in a given time  $t$ , and for a given number density of  $S_2$  nuclei, a larger  $A$  would correspond to more  $S_2$  nuclei being within the path of  $S_1$  nuclei. Therefore, the total number of interactions can be written as

$$N = \sigma \frac{N_1 N_2}{A} = \sigma (n_1 A d) (n_2 d), \quad (2.1)$$

where the constant of proportionality  $\sigma$  is known as the total cross-section. The total cross-section will be a function of the incident energy  $E_1 = \frac{1}{2} m_1 v^2$  (assuming non-relativistic motion) of the  $S_1$  particles.

### 2.3. Reaction Rate and Average Reactivity

The reaction rate per unit volume is

$$R = \frac{N}{(Ad)t} = n_1 n_2 \sigma v \quad (2.2)$$

assuming that all  $S_1$  particles have the same energy and all  $S_2$  particles are at rest in the lab frame. However, in a high-temperature plasma, both species of particles have a thermal

(Maxwell-Boltzmann) velocity distribution [37]. Therefore, the average reactivity, denoted as  $\langle\sigma v\rangle$ , must be used. The thermal (Maxwell-Boltzmann) velocity distribution is

$$dn = 4\pi n \left[ \frac{m}{2\pi kT} \right]^{\frac{3}{2}} e^{-\frac{mv^2}{2kT}} v^2 dv, \quad (2.3)$$

where  $dn$  is the number of particles with velocity between  $v$  and  $v + dv$ ,  $n$  is the number density of the particles,  $m$  is the rest mass of a particle in the distribution, and  $T$  is the absolute temperature. This can then be rewritten in terms of the kinetic energy of the particles of  $S_1$  relative to  $S_2$ ,  $E_1 = \frac{1}{2}m_r v^2$ , and differential kinetic energy  $dE_1 = m_r v dv$ , where  $m_r = \frac{m_1 m_2}{m_1 + m_2}$  is known as the reduced mass:

$$dn = 4\pi n \left[ \frac{m_r}{2\pi kT} \right]^{\frac{3}{2}} e^{-\frac{E}{kT}} \left( \frac{2E}{m_r} \right) \left( \frac{dE}{m_r v} \right), \quad (2.4)$$

which then implies

$$dn = \frac{4n}{\sqrt{2\pi m_r (kT)^3}} e^{-\frac{E}{kT}} dE. \quad (2.5)$$

Therefore, Equation (2.2) can be written as

$$R = \int_0^\infty \sigma(E) n_2 v dn_1 = \int_0^\infty \sigma(E) n_2 \frac{4n_1}{\sqrt{2\pi m_r (kT)^3}} e^{-\frac{E_1}{kT}} dE_1 = n_1 n_2 \langle\sigma v\rangle_{1,2}, \quad (2.6)$$

where

$$\langle\sigma v\rangle_{1,2} = \frac{4}{\sqrt{2\pi m_r (kT)^3}} \int_0^\infty \sigma(E) E e^{-\frac{E_1}{kT}} dE_1 \quad (2.7)$$

is known as the average reactivity. The reaction rate can then be written as

$$R = n_1 n_2 \langle\sigma v\rangle_{1,2} = f_1 f_2 \left( \frac{\rho}{\bar{m}} \right)^2 \langle\sigma v\rangle_{1,2}, \quad (2.8)$$

where  $f_1, f_2$  are the number fractions of each species,  $f_i = \frac{n_i}{n}$ ;  $n$  is the total number density of the two-specie plasma;  $\bar{m}$  is the average ion mass;  $\rho$  is the total mass density.

Measuring the reaction rate in the plasma is then an indirect measurement of the average reactivity. To construct a cross-section as a function of energy, one would need several measurements of reactivity at different average plasma temperatures or a theoretical understanding of the energy dependence, to deconvolute the cross-section as a function of energy.

#### 2.4. Reaction Yields

In an experiment designed to measure the cross-section or reactivity of a given reaction, typically the total number of occurrences of a given reaction is counted. This quantity is known as the yield. If the reaction rate does not rapidly change over time or the volume in which the reactions occur, the yield is roughly proportional to the reaction rate:

$$Y_{1,2} \propto R_{1,2} = f_1 f_2 \left( \frac{\rho}{m} \right)^2 \langle \sigma v \rangle_{1,2}. \quad (2.9)$$

To calculate the yield of a given reaction, the density of the target plasma  $\rho$  must be known. This is a difficult quantity to measure as a function of position in the volume of the plasma and time, but by taking the ratio of the desired yield to a known yield, this dependence cancels out, assuming all species have the same dependence on position and time:

$$\frac{Y_{1,2}}{Y_{3,4}} \cong \frac{f_1 f_2 \langle \sigma v \rangle_{1,2}}{f_3 f_4 \langle \sigma v \rangle_{3,4}} \quad (2.10)$$

for a plasma with species  $S_1, S_2, S_3, S_4$ . Table 1 was generated by integrating Equation (2.7) and utilizing Equation (2.10) with  $S_1$  being a dopant,  $S_2 = S_4$  being deuterium or tritium, and  $S_3$  being deuterium or tritium. The cross-sections needed in these calculations were estimated using the TALYS software (described in Section 2.4.1.2) and S-factors from Ref. [30] in combination with pre-existing data (where available).

##### 2.4.1. Predicting Cross Sections and Yields

As discussed, many light-ion fusion reactions have no measured cross-section or reactivity data below a center of mass-energy of a few hundred keV. Therefore, to evaluate Equation (2.7) and obtain an average reactivity used to predict the yield, a prediction of the cross-

section as a function of energy was made. There are several methods available depending on the previous measurements that have been made to extrapolate from.

#### 2.4.1.1. S-Factor Extrapolation

One method of extrapolating the cross-section uses the S-factor. The physics behind a nuclear reaction can be broken down into two parts: the physics of the Coulomb repulsion, and the nuclear physics that comes into play when the nuclei are close enough to interact [38]. For reactions occurring at an average center-of-mass energy of 10s of keV, there is not enough energy to overcome the Coulomb repulsion, therefore, as stated previously, the mechanism by which the nuclei are able to come within the range of the strong force is quantum mechanical tunneling. For this reason, the probability, and therefore the cross-section, of a given reaction is proportional to the tunnelling probability factor known as the Gamow factor:

$$\sigma(E) \propto e^{-\frac{2\pi Z_1 Z_2 e^2}{\hbar v}} = e^{-\frac{E_G}{\sqrt{E}}}, \quad (2.11)$$

where  $E_G = \pi\alpha Z_1 Z_2 \sqrt{2m_r c^2}$  is known as the Gamov constant and  $\alpha = e^2/\hbar c$  is the fine structure constant. The Gamow factor is derived by solving the one-dimensional case of quantum tunnelling using the WKB approximation. For a full derivation see Ref. [39]. Furthermore, quantum mechanics tells us that the reaction probability is also proportional to the geometric cross-section  $\sigma_{geo} \propto \frac{1}{E}$  [38]. The constant of proportionality between these two factors and the cross-section, which may be a function of the center-of-mass energy, is known as the S-factor. Therefore,

$$\sigma(E) = S(E) \frac{1}{E} e^{-\frac{E_G}{\sqrt{E}}}. \quad (2.12)$$

This type of approximation takes advantage of the fact the  $S(E)$  typically varies slowly with  $E$  since the quickly varying dependence on  $E$  has been factored out into the inverse factor and the exponential factor [40]. Cross-sections at lower energies can be extrapolated by fitting Equation (2.12) to previously measured cross-section data at higher energies. The



need for existing cross-section data, as well as the fact the approximation becomes less reliable the further one extrapolates, limits the usefulness of this method [12].

#### 2.4.1.2. TALYS

TALYS [29] goes beyond the simple S-factor extrapolation and incorporates other relevant considerations to estimate the cross-section of a given reaction, such as the basic nuclear structure and angular momentum. It uses the optical model, which attempts to describe the elastic and inelastic interactions between the nuclei and the incident particle based on the complex, one-body potential of the pre-equilibrium system. It also accounts for the pre-equilibrium behavior of the incident particle being absorbed to form a compound nucleus, and the further decays after the decay of the compound nucleus. The TALYS code aims to more accurately predict the cross-section of reactions with targets that having  $Z \geq 3$  and  $A \geq 5$ . However, like the S-factor extrapolation, this method is limited by the availability of previous measurements, as TALYS functions by obtaining several parameters from a fit to previous measurements.

#### 2.4.1.3. R-Matrix

The R-Matrix approximation attempts to overcome the shortcomings of the S-factor approximation by predicting the cross-section of a given reaction without reference to pre-existing data of the reaction of interest. Instead, the R-Matrix approximation obtains cross-section estimates by fitting parameters the nuclear structure of the compound nucleus which the desired reaction passes through. Taking advantage of the relatively short range of strong nuclear interactions, the method models “channel radii” around the target nuclei in which the nuclei and the incident particle can be modeled as a two-body interaction. Essentially, by knowing how a certain compound nucleus behaves, one can use an R-matrix approximation to model the behavior of any interaction which passes through the same compound nucleus. This allows for one to consider the Coulomb and angular momentum potential barriers, which helps to model the interaction more completely [38]. However, in modeling the behavior of the compound nucleus, the method relies on fits to previous measurements of different reaction channels. This method can be used when the reaction of interest passes through a compound nucleus which has several channels that have been well-measured.

#### 2.4.2. Radioisotopes to Be Measured in the Proposed Methodology

As previously mentioned, TALYS and S-factors from previously measured data were used to estimate the yields of several light-ion reactions that could be measured with the proposed methodology. The notable exception to this is the  ${}^3\text{H}(t,\gamma){}^6\text{He}$  reaction, which has no previous measurements at any energy, so an S-factor extrapolation is impossible, and the target has an  $A < 5$ , which is not allowed by TALYS. However, an estimate using AZURE2 [41], a code which utilizes the R-matrix method, is current being attempted, as R-matrix calculations have previously been made for the  ${}^6\text{He}$  compound nucleus to calculate  ${}^3\text{H}(t,2n){}^6\text{He}$  cross sections [42], which could be of use here. With the yields of potential reactions estimated, a ride-along experiment on LLE's OMEGA-60 laser system was conducted that would test if the constructed detector system could see the decays of products of the reactions of interest above the background.

## Chapter 3

### EXPERIMENT

#### **3.1. Introduction**

In this section, a full description of the pulse separation electronics for particle identification, the construction and preliminary testing of both the getter and  $4\pi$  detectors, and the circuit used to isolate the electronics during the LLE ride-along will be discussed. Additionally, a more detailed description of the 2019  $^{41}\text{Ar}$  experiment and the LLE ride-along experiment will be given.

#### **3.2. Data Acquisition**

In order to analyze the signals from the dE and E layers of the phoswich detectors, a system used to separate the PMT's output pulses into their constituent fast and slow components was developed. The electronics that were used to separate the pulses were briefly mentioned in Section 1.4.2, however, the final system used in both experiments that were conducted will be discussed in greater detail in this section.

##### 3.2.1. Pulse Separation

As discussed in Section 1.4.2, typical pulses from a phoswich detector system were comprised of a fast pulse from the dE layer and a slow pulse from the E layer, shown in Figure 16. These pulses were separated by NIM electronics before being sent to the data acquisition computer (described in Section 3.2.2) to be recorded. A block diagram of these electronics is shown in Figure 18.

Pulses from the PMT (trace 1 in both subfigures of Figure 19) were split, with one path leading to a Lecroy 428F linear fanout (LF), and another path heading to a Lecroy 612A PMT amplifier (AMP). This was done to ensure that a copy of the original pulse was preserved, as an amplified pulse would also carry amplified noise. The path which was amplified then connected to an Ortec 538B constant fraction discriminator (CFD) whose discriminator threshold was set to just above background noise.

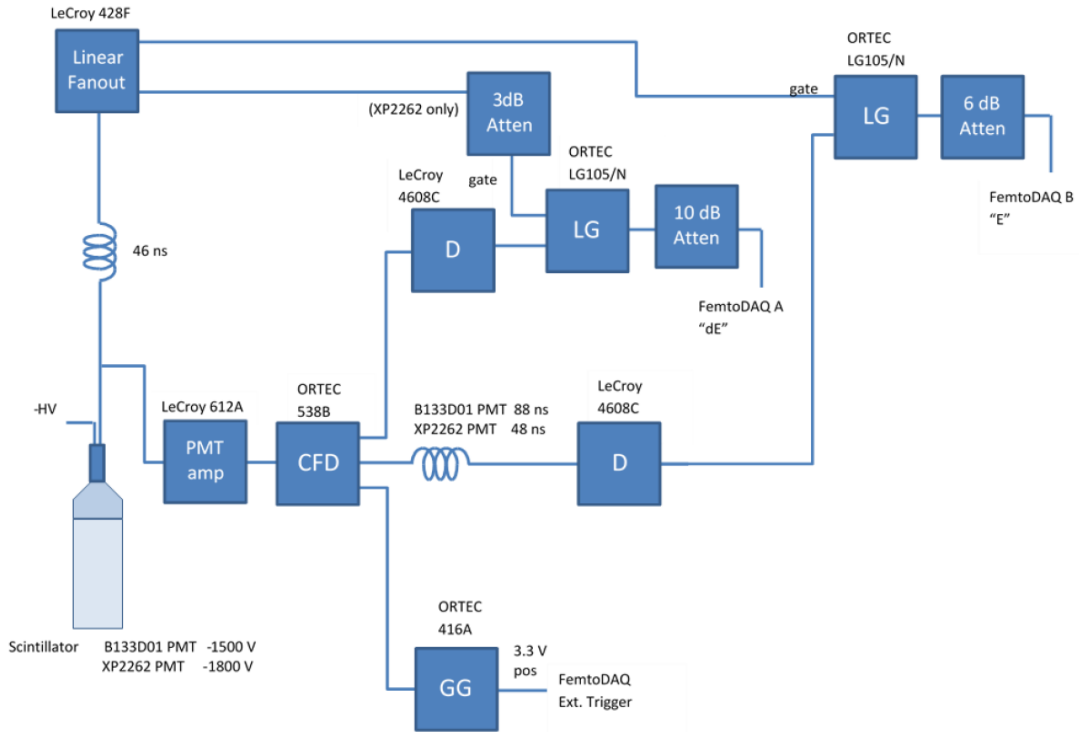


Figure 18. PMT pulse separation circuit. Here, CFD stands for constant fraction discriminator, GG for gate generator, D for discriminator, and LG for the linear gate. Model numbers are written above each component block.

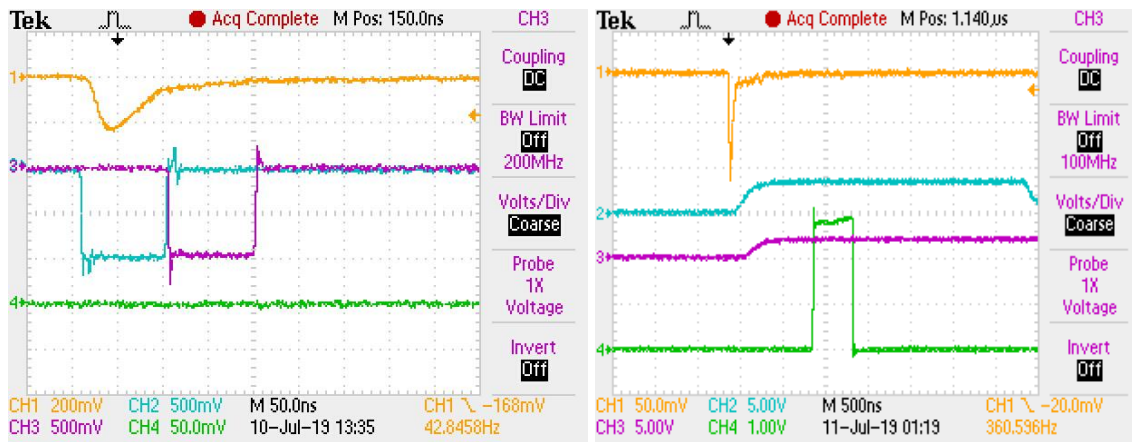


Figure 19. Traces of the pulses during each step of the pulse separation process. The signal from the PMT (orange) and the two gates enclose the two different components of the pulse (fast gate is blue, left; the slow gate is purple, left). The outputs from the linear gates are also seen above (fast output blue, right; slow output purple, right), as well as the trigger for the FemtoDAQ (green, bottom).

The CFD output was then sent to an Ortec 614A gate generator (GG) to generate a logic pulse that would trigger the data acquisition computer and to Ortec LG105/N linear gates (LG) to generate the gates for the dE and E components of the original pulse, allowing only the desired component of the pulse through to be digitized. The 4608C Discriminators were used to adjust the width of the gates. Delays were added to select the dE and E components of the pulse. This circuit is shown in Figure 18 and Figure 19 shows the timing at each step of the circuit. The digitized pulses were then plotted into a histogram.

### 3.2.2. Data Acquisition Computer

The data acquisition computer used was a SkuTek FemtoDAQ LV-2 running Linux BeagleBone, which executed a Python code that controlled a field-programmable gate array (FPGA) that digitized pulses when triggered. These digitized pulses were stored in a memory buffer until a configurable timeout period elapsed or the buffer filled. The FemtoDAQ then read out the events' dE and E component pulse heights, with their timestamps, into a file. This file was then transferred to a PC and analyzed using a C script which utilized ROOT [47], a statistical analysis package created by CERN. This script plotted the file into histograms for both the dE and E pulses, as well as a combined 2-D histogram. The script was also modified to show how the shape of the histograms changed over time, among other factors. The Python code used to control the FPGA is found in Appendix D, and the C script used to analyze the data is found in Appendix E.

## 3.3. *The Getter Phoswich Detector*

The first detector that was designed and constructed was the getter detector. This detector was designed to be small, as it would need to be within the target chamber during a laser shot. Additionally, this detector can be fitted with a getter material, which would trap chemically reactive products as the plasma expanded and cooled, and can be mounted to light guides, which would allow the PMT to be further from the target chamber, reducing the probability of it being damaged by primary radiation from the implosion.

### 3.3.1. Design

The getter detector follows the general design of a simple phoswich detector outlined in Section 1.4.1 and pictured in Figure 15. It is 13 mm diameter, 19 mm tall cylinder consisting

of a 1 mm thick circular layer of EJ-212 plastic scintillator, which has a rise time of 0.9 ns and a decay time of 2.4 ns, optically coupled with EJ-550 silicon optical grease ( $n = 1.46$ ) to an 18 mm thick layer of EJ-240 plastic scintillator, which has a decay time of 285 ns. The total thickness of 19 mm was chosen as this is thicker than the range of 2 MeV betas in the scintillator, which ensures that betas that enter normal to the detector are stopped. The scintillator was then optically coupled with EJ-550 silicon optical grease to an ET Enterprises XP2262 PMT. All optical couplings were made by first cleaning the surfaces with isopropyl alcohol and Kimtech task wipes, applying a thin layer of optical grease via a gloved finger to both surfaces, and pressing the surfaces together until all air pockets were squeezed out. Then, in order to prevent light from escaping, the scintillator and PMT assembly was wrapped in smooth, reflective layer of 0.016 mm thick  $^{27}\text{Al}$ . Finally, a light sheath was designed and 3-D printed from PLA plastic that fit over the detector and PMT, holding the scintillator in place and making the detector light-tight. An Ortec Model 269 PMT base was used to power the PMT. Figure 20 shows the final getter-detector assembly.

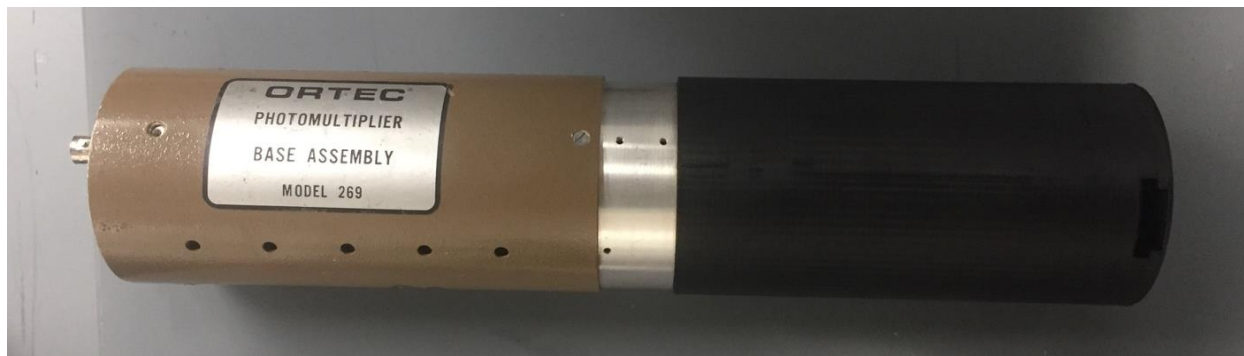


Figure 20. Final getter detector assembly. Pictured here is the getter detector and XP2262 PMT encased in the 3-D printed light sheath, attached to the Ortec model 269 PMT base.

### 3.3.1.1. Performance

To test the performance of the getter detector, a  $^{207}\text{Bi}$  source, which emits roughly 1 MeV betas, was placed within the slot shown at the top of the light sheath at the right of Figure 20. Pulses from the PMT were then viewed with an oscilloscope and recorded using the pulse separation electronics described in Section 3.2.1. A 2-D histogram of the events is shown in Figure 21 and the decay scheme of  $^{207}\text{Bi}$  is shown in Figure 23.

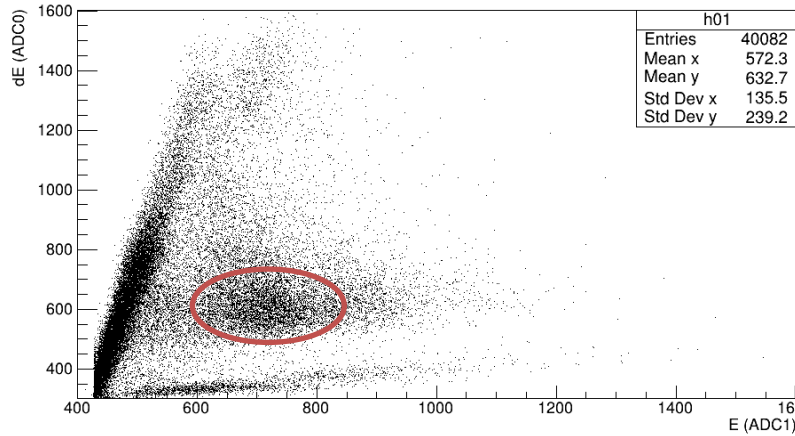


Figure 21.  $^{207}\text{Bi}$  test run with the getter detector. Pictured above is a 2-D histogram generated during the preliminary test of the getter. The dE component of the pulse height is shown on the vertical axis, while the E component pulse height is shown on the horizontal axis. The circles region contains roughly 1 MeV betas emitted during  $^{207}\text{Bi}$  decay.

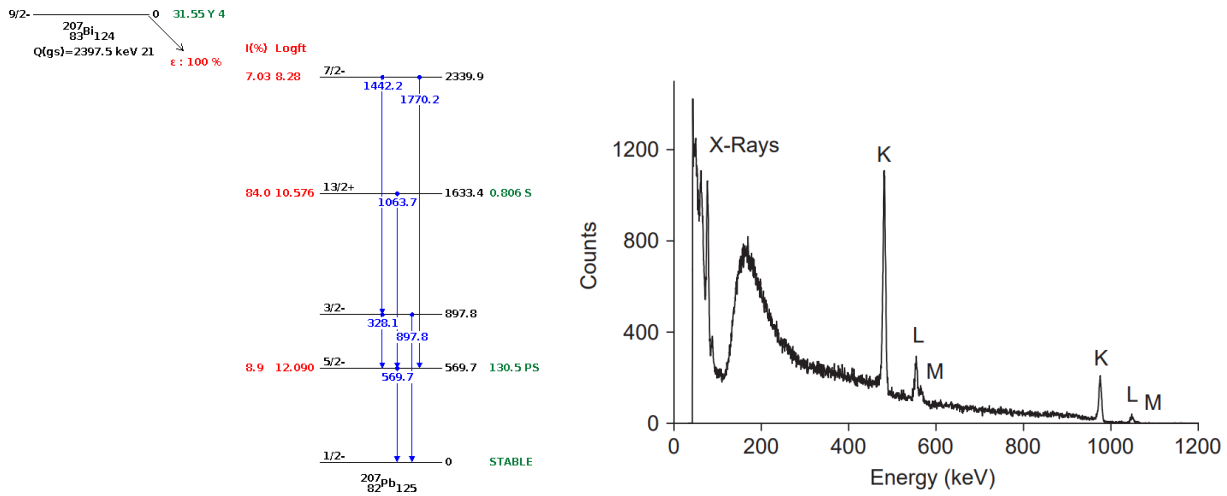


Figure 22.  $^{207}\text{Bi}$  decay scheme and conversion electron spectrum. Decay scheme generated using Ref. [11], and conversion spectrum taken from Ref [43].

### 3.4. The $4\pi$ Phoswich Detector

Though it served as a testing prototype for the pulse separation electronics the getter detector can only be effectively used with the getter collection method. Due to the predicted low yield of many of the proposed reactions (Table 1), the entire trapped gas volume in the turbo pump needed to be counted with a detector that has the largest solid angle possible. Therefore, a detector that would enclose the trapped gas within its inner volume, while counting the decays, was designed.

#### 3.4.1.1. Design

The chosen design was that of a hollow rectangular prism, with a solid angle of close to  $4\pi$  steradians, that could be evacuated and then serve as a chamber for the radioactive gas to expand into once trapped behind the output port of the turbopump. This design was chosen because it could easily be hand-constructed, attached to the output port of turbopump, and had an inner volume that was large compared to the inner turbine volume of the turbopump and output vacuum pipes. This ensured that most of the trapped gas is in the detector and not within the fore line or turbopump. The hollow rectangular prism consisted of an inner prism constructed from a thin layer of fast scintillator, optically coupled via the method described in Section 3.3.1 to a thicker layer of slow scintillator. Additionally, a hole was drilled in the bottom face that was tapped to allow for a QF-16 vacuum flange with NTP  $\frac{1}{2}$ " nipple to be screwed in so the detector could be connected to the output port of the turbopump. Figure 23 shows a drawing of the design.

The pairing of a 1 mm thick layer of EJ-212 and 18 mm thick EJ-240 scintillator was chosen. Again, this pair was chosen because it was thicker than the range of endpoint betas that would be emitted by the reactions of interest in Table 1. The CAD drawing of the  $4\pi$  detector can be found in Appendix A.

#### 3.4.1.2. Construction: Prototype

Before the full detector was cut and assembled using the EJ-212 and EJ-240 scintillator, a model made from spare 16 mm thick, and 0.8 mm thick acrylic was constructed in order to become familiar with techniques for cutting and gluing plastics similar to the scintillator. The 18 mm and 1 mm acrylic were not available at the time, so the external dimensions seen in Appendix A were modified to have an acrylic wall thickness of 16.8 mm to ensure that the internal dimensions of the acrylic box remained the same, preserving the inner volume. The entire prototype was glued using EJ-500 optical cement, the adhesive that was intended to be used for the final detector. As seen in Figure 24, many defects were present and needed to be corrected. Firstly, the optical cement was only slightly more viscous than water, so it did not fill gaps between the pieces. Small errors in the machining of the pieces accumulated into about a 0.5 to 0.75 mm gap in the joint between the bottom face of the outer thick pieces



and the bottom cap piece. This left bubbles in some of the other joints despite being clamped while curing.

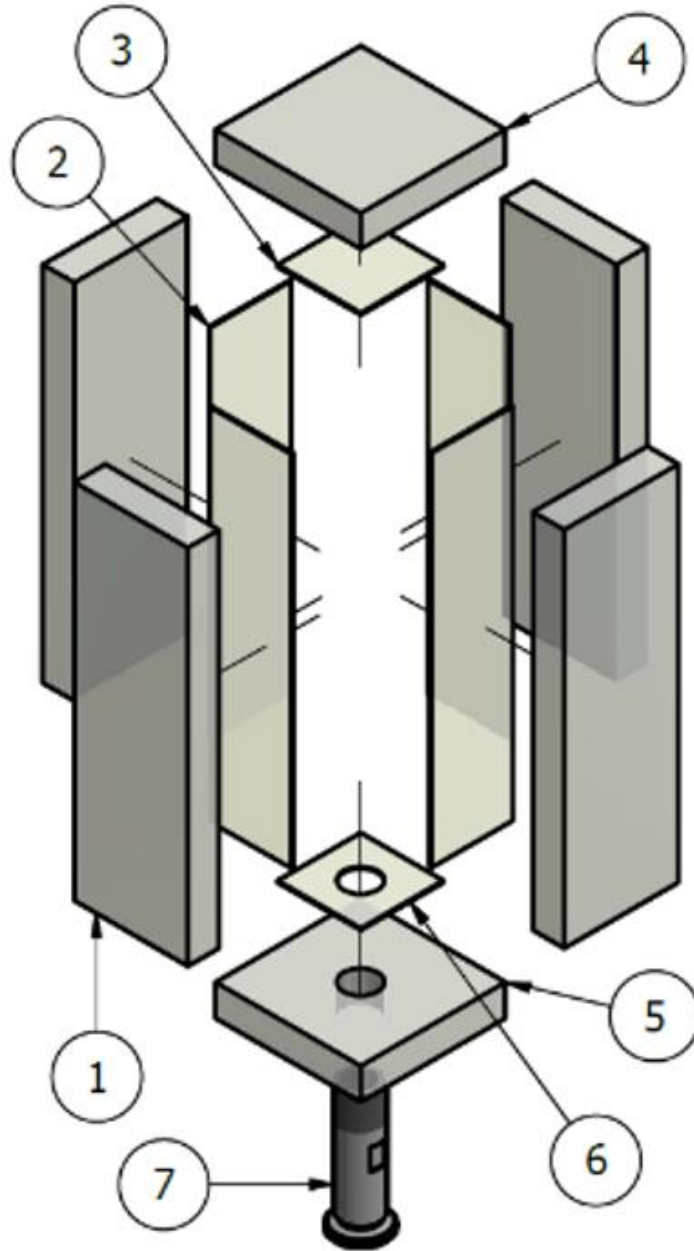


Figure 23. Drawing of the  $4\pi$  phoswich detector. The design would consist of sheets of the slow scintillator (1, 4, and 5) optically coupled to sheets of the thin scintillator (2, 3, and 6) with a threaded hole drilled in the bottom face so that a QF-16 half nipple could be attached so that the detector could be mounted to the turbopump output port. The overall dimensions of the detector are 8.4 cm x 8.4 cm x 24.6 cm (not counting the QF-16 flange).



Figure 24. The finished acrylic prototype detector. Many visual imperfections exist within the practice detector: glue joints were not perfectly coupled structurally or optically due to bubbles within the glue joints, measurements of the end caps were slightly off compared to the rest of the body (by about 3 mm), and glue had hardened on the outside surface of the box due to resting on a surface while curing rather than being suspended in a clamp.

Additionally, the epoxy frequently oozed out of the joints and dry onto the outside face while the piece was curing. Since it was not possible to clean the pieces thoroughly during the entire 24-hour period, this left a residue on the outside face.

To ensure the best light transmission, these imperfections needed to be corrected. To solve the issue of the optical cement not filling the joints, many different adhesives with higher viscosities were tested. They were assessed visually based on transparency (for good optical coupling), set and cure time, viscosity (how easily did it structurally complete the connection without clamping or added pressure, as this increases seepage out of the joint), and strength of the bond. Devcon 2-Ton Epoxy was selected based on its relatively quick set and cure times of 30 min and 10 hr, overall transparency, viscosity, and strength.

#### 3.4.1.3. Construction: Detector

Based on the work done constructing the acrylic prototype, the following method was developed and two  $4\pi$  detectors were constructed. Four pieces of the 18 mm EJ-240 were slowly cut by hand on a bandsaw (labeled 1 in Figure 23). These pieces were then all clamped together, with cardboard spacers between the clamps and the plastic to prevent scratches, and had both their long edges end milled (scrolling across the surface at about 1 to 3 mm/s) to ensure that the long edges were parallel. Next, they were oriented and clamped such that milling the short edge would ensure that the short and long edges were perpendicular to

each other. When finished, the four thick pieces were the same size and squared off. This entire process was repeated using the 1 mm EJ-212 to create the inner thin layers (labeled 2 in Figure 23). Next, two 84 mm x 84 mm square pieces of the 18 mm EJ-240 were cut for the end cap pieces (labeled 4 and 5 in Figure 23). They were milled using the previous procedure to ensure all sides were square and opposite sides were parallel. Finally, the same process was repeated on two 46 mm x 46 mm square 1 mm EJ-212 pieces to create the inner plastic end caps (labeled 3 and 6 in Figure 23). Pieces labeled 5 and 6 were then clamped, drilled, and tapped through using a 1/2" NPT tap. Figure 25 shows the pieces at this stage of the construction.



Figure 25. Cut EJ-212 and EJ-240 scintillator pieces. The EJ-212 “thin” scintillator was cardboard-backed (to prevent scratches) while the EJ-240 “thick” scintillator was wrapped in protective, transparent plastic sheet. Both protective measures remained on the scintillator pieces until they were ready for polishing. Referencing Figure 23, pieces labeled 1 are seen on the right, pieces labeled 2 are seen in the center with the cardboard backing, pieces labeled 4 and 5 are seen in the center at the top, and pieces labeled 3 and 6 are seen on the left with the cardboard backing.

Once all pieces were cut, they were prepped for gluing. After each of the following sanding and polishing steps the pieces were rinsed with water and cleaned with isopropyl alcohol and a Kimtech task wipe. Each piece had every milled edge sanded with 600 grit silicon carbide sandpaper until all visible tooling marks were removed, then 1500 grit silicon carbide sandpaper was used until a smooth, transparent finish was achieved. Next, Novus

plastic/acrylic polish was used to further refine the finish. Novus #3 Heavy Scratch Remover was applied generously to all the cut edges and buffed with Kimtech task wipes. Once any remaining blemishes were removed, the pieces were washed with soap and water. Novus #2 Fine Scratch Remover was then used with Kimtech wipes until all edges had a near-complete transparent finish. The pieces were then washed again with soap and water. Finally, Novus #1 Plastic Clean and Shine were sprayed unto all surfaces of the pieces and buffed until dry. Lastly, just edges that were to be glued were slightly roughened with 400 grit silicon carbide sandpaper, then washed with soap and water, left to dry, and wiped down with isopropanol.

All pieces were polished using the Novus polish process described above and cleaned with isopropanol before each gluing step. First, two thick pieces were glued together into L-shaped corners (Figure 26 left) using the Devcon 2-Ton Epoxy and then allowed to cure for 24 hours. Next, the EJ-212 and EJ-240 scintillation layers were glued with EJ-500 optical cement using the procedure described in Section 3.3.1, mixed three-parts epoxy to one-part hardener by volume (Figure 26 center). Then, the two L-shaped segments were glued together, using Devcon 2-Ton Epoxy (Figure 26 right). The Devcon 2-Ton Epoxy was used in gluing the larger pieces together due to its higher viscosity, as described in Section 3.4.1.2, as this ensured better optical and structural coupling than the EJ-500 optical cement. Figure 27 shows the glued-L-shaped pieces and end caps, just before the final assembly.

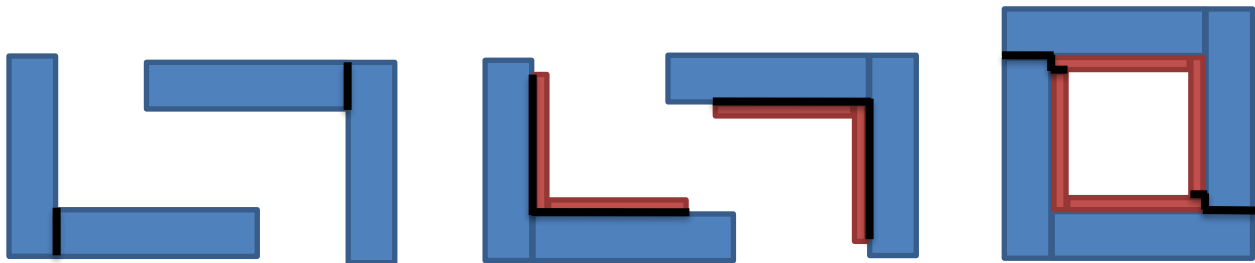


Figure 26. Scintillator box gluing process. The slow plastic is shown in blue; the fast plastic is shown in orange. The current joint to be glued is shown by a black line. (Left) Step 1: Gluing the plastic “L” s. (Center) Step 2: Gluing the inner thin pieces to the outer thick “L” s. (Right) Gluing the “L”s together. The staggering of the thin and thick pieces was done to offer extra structural support, as the box would have to hold a vacuum (down to just a few hundred mTorr).

While gluing the thin pieces to the “L”s, the thin end pieces were glued to the thick end pieces. While the glue was setting after the two “L” s were put together, the top and bottom caps

were glued on. During the gluing process, the entire assembly was hand-leveled and C-clamps with foam covers (to protect the plastic) as well as 2 kg weights were used to supply pressure to the curing glue joints, while any excess glue was wiped from the seams with Kimtech wipes and isopropanol. The whole assembly was then allowed to cure for 24 hours and both the outside and inside of the detector (where possible) were thoroughly polished using the previously described method.

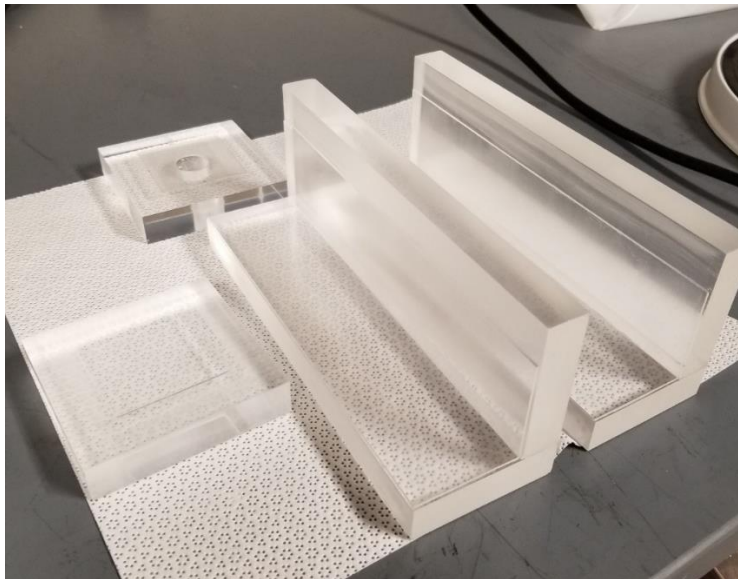


Figure 27. The scintillator before the final assembly. Each piece that was to be assembled is shown here, after being re-polished with the above-mentioned method and cleaned with isopropanol.

On the first attempt to assemble the detector, the EJ-212 bottom piece could not be coupled with the EJ-240 bottom piece due to small mistakes in the machining of the rest of the detector, so it was discarded. However, on the second attempt, all pieces fit as designed. All pieces were cleaned with Kimtech wipes and isopropanol and re-polished using the original procedure to maintain a transparent finish and remove any excess glue from areas near the joints.

After the detector was completely assembled, its ability to hold a vacuum was tested, as well as its behavior when counting beta decays from a source within its inner volume.



Figure 28. The finished phoswich detector. The second attempt to assemble the detector had only a few visible defects, and all pieces were securely coupled with no visible gaps and few bubbles (all smaller than 1 mm in diameter).

#### 3.4.1.4. Construction: PMTs and Bases

After the scintillator detector had been successfully built, several PMTs and PMT bases were tested and categorized to see which PMT and PMT base provided the best combination of signal amplification and response time for the  $4\pi$  detector. Due to the top face of the detector (labelled 4 in Figure 23) being a roughly 8.6 cm x 8.6 cm square (3.39" x 3.39"), a PMT with an active photocathode area that would completely cover the top face of the detector was needed. For this reason, only 5" PMTs were assessed. An ET Enterprises 9823KB PMT was purchased brand new from the manufacturer, while an ADIT B133D01 was purchased second hand to serve as backup. Due to sparking within the homemade PMT base used for the 9823KB the ADIT B133D01 PMT was selected to use until a new base could be obtained. Testing of the PMT and base occurred simultaneously with the construction of the  $4\pi$  detector, therefore the scintillators from the getter detector were optically coupled to the face of the desired PMT using EJ-550 silicon optical grease using the method described in Section 3.3.1. The PMT and detector were then covered in a layer of aluminum foil, using the method described in Section 3.3.1, to reflect emitted light back towards the phototube and to act as a light shield to stop outside light from entering the detector and PMT. The entire assembly was then wrapped in closely wound electrical tape and placed inside of a cardboard box to further ensure that the system was light-tight. A  $^{207}\text{Bi}$  source was placed roughly 1 cm from the phoswich detector. The phototubes were then supplied with the required voltage by the base and signal pulses were displayed on an oscilloscope.

An optimal PMT and base combination would provide enough gain such that the signal pulses were on the order of tens to hundreds of mV with a width of roughly 300 ns and provide enough resolution such that the separate fast and slow pulses were visible within the output pulse. An example is shown in Figure 16.

The need for a PMT base that supplied negative high voltage (at the time it was believed that positive HV was adding noise in the output signal) created the need for a custom PMT base to be built to deliver the correct voltages to the dynodes within the PMT. This also allowed for a transistor-less design which would be less susceptible to the EMP after a laser shot.

Two custom bases were constructed. They were composed of simple 330 k $\Omega$  resistor divider circuits which are shown in Appendix B.

#### 3.4.1.5. Performance: Vacuum Testing

After the 4 $\pi$  detector was constructed, it was tested on how well it could hold a vacuum (this would give insight into how well it could hold the product gas within its inner volume) and if it could produce clear pulses that could be processed by the electronics described in Section 3.2.1. The assembled 4 $\pi$  detector was able to be held at a pressure of 12 mTorr after 30 s to 60 s of evacuation by an Alcatel Pascal 2005 SD forepump.

#### 3.4.1.6. Performance: Source Testing

After the detector was shown to hold a vacuum, its ability to detect beta decays was tested. The detector was optically coupled to the ADIT B133D01 PMT with EJ-550 optical grease and wrapped in 0.016 mm thick  $^{27}\text{Al}$  foil using a similar procedure to the one described for the getter detector in Section 3.3.1. The PMT and detector were then wound tightly in electrical tape to further prevent light leaks and hold the detector in place. A  $^{207}\text{Bi}$  source was suspended within the detector on a threaded rod through a light-tight stopper in the QF-16 flange, and the external lights within the testing area were turned off. The operating voltage (-1200V) was supplied and the signal output of the base was connected to the NIM electronics as shown in Figure 18 and produced the 2-D histogram shown in Figure 29. These preliminary tests showed that the 4 $\pi$  phoswich detector could identify the beta particles from beta decay of a source within its inner volume. After this preliminary test, an acrylic holder which clamps the detector to the ADIT B133D01 PMT was designed and constructed. This provided further structural stability in the detector and PMT assembly and helped to further prevent light leaks into the photocathode of the PMT. This clamp and the final 4 $\pi$  detector assembly can be seen in Figure 30.

### **3.5. 2019 $^{41}\text{Ar}$ Experiment**

In the summer of 2019, an experiment in collaboration with State University of New York College at Geneseo (SUNY Geneseo) was conducted to test the performance of the 4 $\pi$  phoswich detector and data acquisition system.



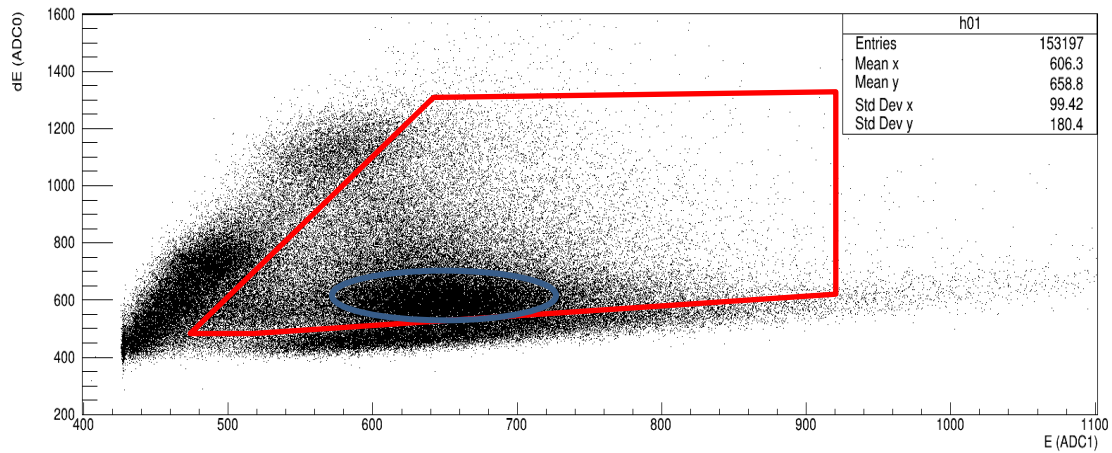


Figure 29. 2-D histogram of a  $^{207}\text{Bi}$  source produced by the  $4\pi$  detector. The blue outline surrounds what are believed to be 1 MeV beta particles from  $^{207}\text{Bi}$  decay. The red quadrilateral shows a region visually selected to be good beta events.

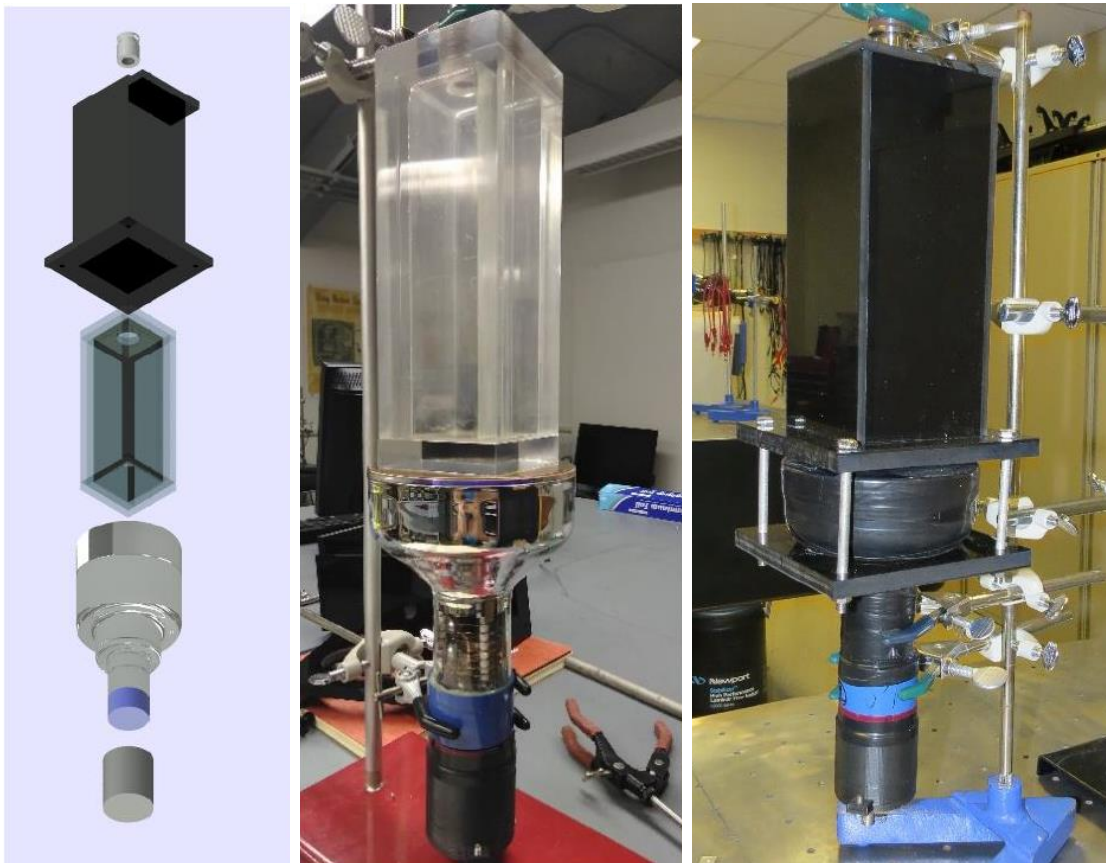


Figure 30. Final  $4\pi$  detector assembly. (Left) A CAD render of the PMT Base, ADIT B133D01 PMT,  $4\pi$  phoswich detector, and acrylic casing. (Center) The  $4\pi$  phoswich detector optically coupled to the ADIT B133D01 PMT before being wrapped in foil and clamped into the casing. (Right) The final assembly of the  $4\pi$  detector within the acrylic casing, clamped to the PMT.

It was shown in the preliminary detector tests that the  $4\pi$  detector could hold a vacuum and detect the beta decay of a source within the detector. However, it was yet to be tested whether the detector was sensitive enough to detect a small number of decays from a radioactive gas of short half-life. Additionally, the ability to identify the presence of a given radioisotope based on the decays recorded by the data acquisition system had yet to be measured. To test both of these points,  $^{41}\text{Ar}$ , a radioactive inert gas (chosen because of its chemical similarity to  $^6\text{He}$ , the product of the  $^3\text{H}(t,\gamma)^6\text{He}$  reaction), was created in a gas cell using SUNY Geneseo's tandem pelletron accelerator and released into the  $4\pi$  detector.

### 3.5.1. Apparatus and Procedure

The PVC gas cell was provided by the pelletron accelerator team at SUNY Geneseo. This cell was flushed and then filled with  $^{40}\text{Ar}$  gas, then positioned at the end of the beamline. A thin Kapton window was used to allow deuterons to leave the evacuated end station and enter the gas cell. A beam of 2 MeV deuterons was produced by the accelerator which produced  $^{41}\text{Ar}$  by the  $^{40}\text{Ar}(d,p)^{41}\text{Ar}$  reaction. The argon was activated by the deuteron beam for at least one half-life of  $^{41}\text{Ar}$  (about 109 min). The gas cell was then attached to the vacuum system shown in Figure 31, which was evacuated by an Alcatel Pascal 2005 SD forepump to a pressure of roughly 15 mTorr. All valves between the gas cell and the detector were then opened, allowing the Ar mixture to expand into the detector's inner volume. The valve at the entrance of the detector was then closed and counting began. Counts were measured by the  $4\pi$  detector, a silicon surface barrier detector (shown at the top of the 4-way cross in Figure 31), a NaI detector (shown just behind the  $4\pi$  detector in Figure 31), and a HPGe detector (not shown in Figure 31). A second method of producing and trapping  $^{41}\text{Ar}$  was also attempted. A liquid  $^{40}\text{Ar}$  capsule was placed beside a PuBe neutron source inside a howitzer and left to be activated for several hours. The vacuum system was evacuated, and the liquid argon cell was attached to the apparatus. A final valve was then opened to allow the liquid argon to rapidly evaporate and expand into the detector. However, even after counting decay events for 8 hr, only a small number of decays were counted. The results of this experiment will be discussed in further detail in Chapter 4, but to summarize, the experiment showed that the  $4\pi$  detector and data acquisition system could detect the beta decay of a radioactive, inert gas that was trapped in the detector's inner volume. Using the data collected during

this experiment, an estimate for the absolute efficiency of the detector was made. The next step was to test the feasibility of counting such a decay in the high background environment a few milliseconds to seconds after an ICF implosion at LLE.

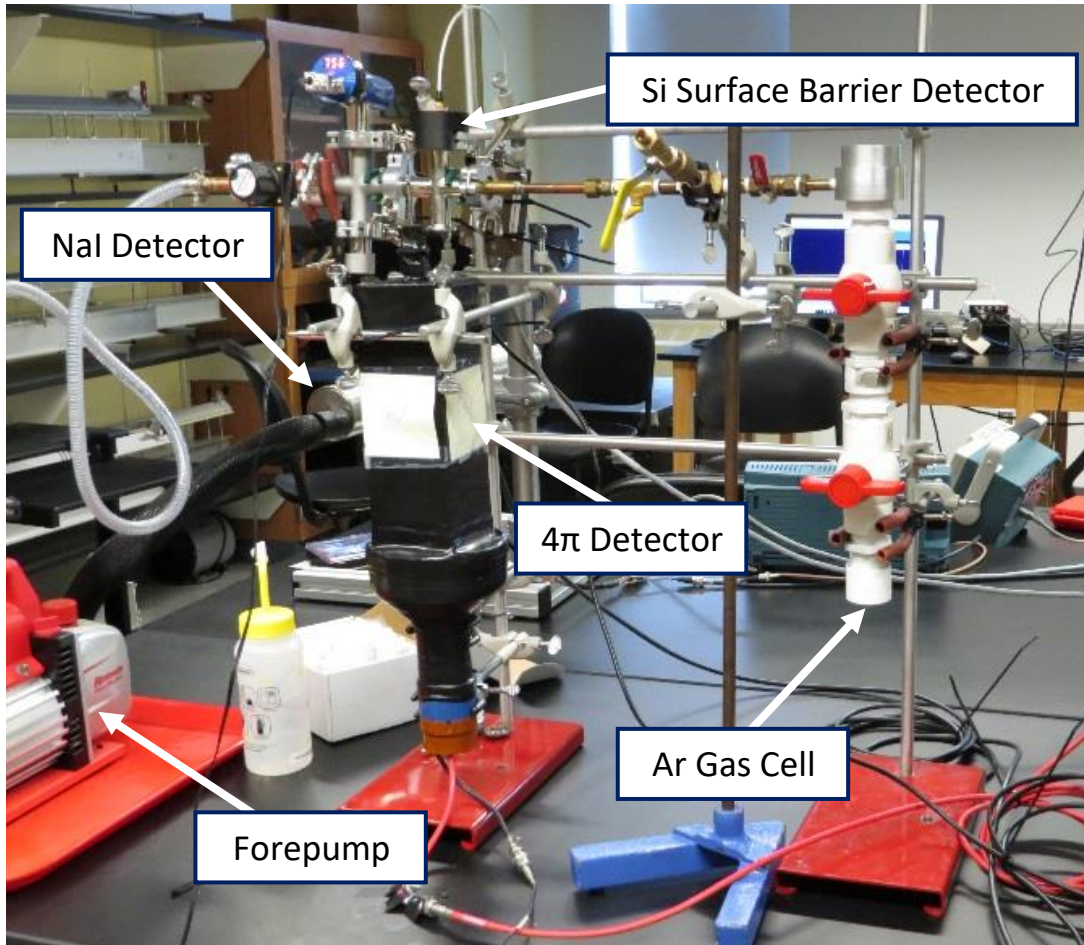


Figure 31. SUNY Geneseo Vacuum System. The  $4\pi$  detector, seen in black was affixed to the ADIT B133D01 PMT and connected to a small vacuum system which was evacuated to about 30 mTorr. The PVS gas cell, seen on the right, was connected to the same system, the other detectors present are also shown, but the HPGe detector is not pictured here. Valves were then opened and allowed the mixture of  $^{40}\text{Ar}$  and  $^{41}\text{Ar}$  to flow into the inner volume of the detector.

### 3.6. *L.L.E. Ride-Along*

The proposed methodology assumes that the level of background radiation after the ICF shot is substantially less than the number of desired product nuclei decays in the same period. However, no previous measurements of the background rate near the target chamber after an ICF shot at OMEGA-60 had ever been made. This was the goal of this experiment. Additionally, the behavior of the electronics and the detector were monitored in the time

before, during, and after a shot. A system for isolating the electronics of the experiment from the EMP was also tested.

### 3.6.1. Relay Electronics

Immediately following a shot, large amounts of gamma and neutron radiation are emitted, as well as a large EMP that has the potential to damage unshielded electronics nearby. To prevent such damage from occurring, the detector's signal and power were electrically disconnected before and during the shot. Then, after a set time after the laser shot, a relay circuit with 15 kV isolation reconnected the signal and power inputs. The schematic of the relay circuit can be found in Appendix C.

### 3.6.2. Apparatus and Procedure

Both the getter and  $4\pi$  phoswich detectors were taken to LLE and placed within 2 m of the target chamber wall, as shown in Figure 32. The detectors were prepared via the method described in Section 3.3.1.1 for the getter detector and Section 3.4.1.6 for the  $4\pi$  detector. When a shot occurred, a TTL trigger pulse was sent from the OMEGA-60 control system to an Arduino Uno which then waited for 2 ms, to ensure that the initial EMP, neutron, and gamma flux had passed, and then closed the isolation relays. The TTL trigger pulse also signaled the FemtoDAQ to begin processing events after a short delay. A block diagram of the relay electronics can be found in Figure 33.

Once the relays were closed, counting began. As mentioned in Section 3.2.2, the FemtoDAQ controlled an FPGA which would digitize and store the pulse information after receiving a trigger. The data in the FPGA's memory buffer would then be read out into a file by the FemtoDAQ after a set timeout period, or when the buffer filled. This timeout was varied between shots in response to the high count rate observed (this is further discussed in Section 4.3.1).

Of the eight shots documented in Tables Table 2 and Table 3, four shots were measured successfully. The shots were measured over varying time intervals from 220 s to 300 s after the shot. Additionally, shielding in the form of  $^{207}\text{Pb}$  bricks between the detectors and the target chamber was also tested. The detectors and electronics were tuned and calibrated



several times throughout the day to ensure that they were still behaving as intended. These runs are listed in Table 2 and further details of the high-yield D-T shots are listed in Table 3.

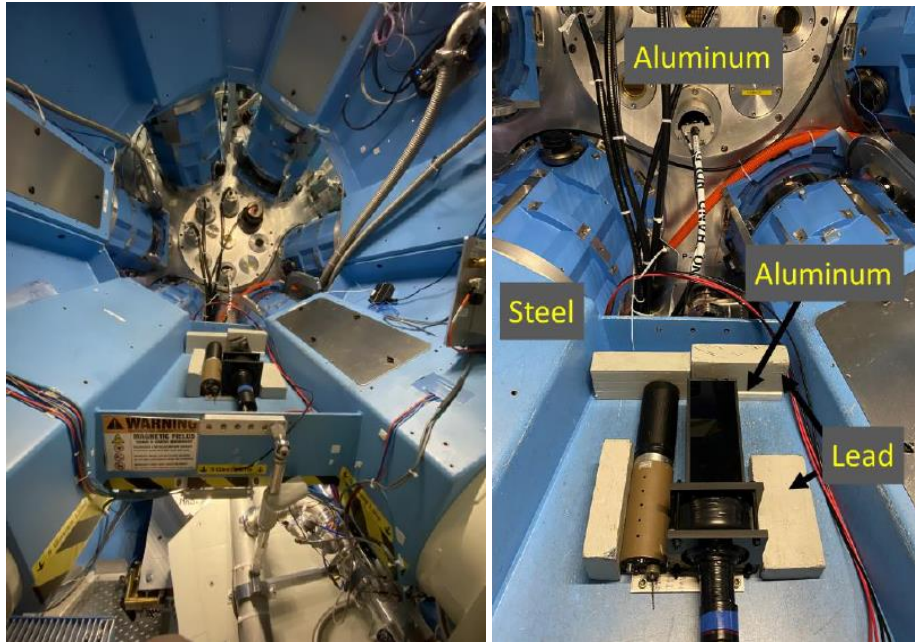


Figure 32. The small and  $4\pi$  detector detectors outside the LLE target chamber. Each detector was placed outside the target chamber and could be connected to power and the data acquisition system between shots, interchanging which detector was being tested.

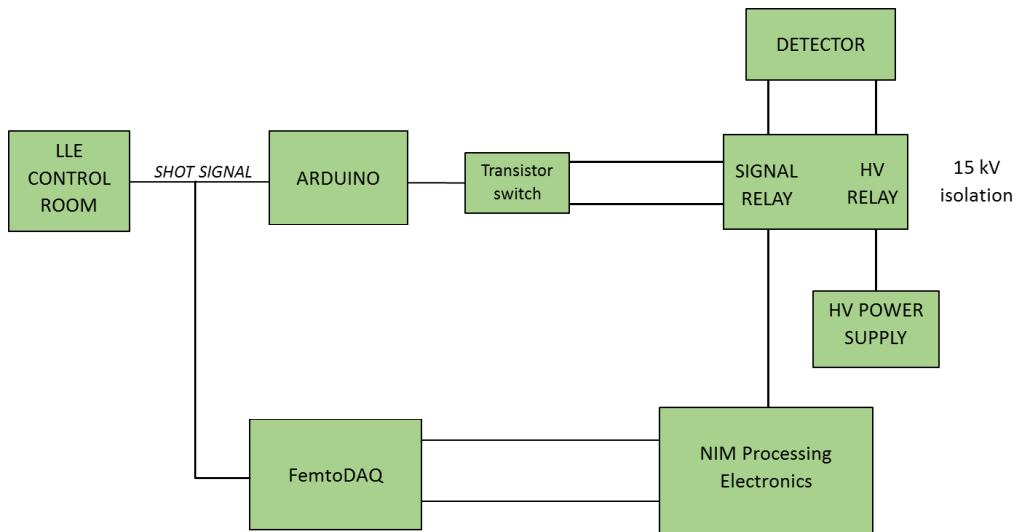


Figure 33. Block diagram of electronics for the LLE experiment apparatus. A signal was received from the LLE control room at the time of the shot, triggering the Arduino, which then waited 2 ms before closing the isolation relays and signaling the FemtoDAQ to begin counting events.

Table 2. LLE Experiment Run List. Shown below is every successful data collection run conducted during the 2020 LLE Experiment. Runs fall under the categories of “Tuning Run”, where the settings for the pulse separation electronics were tweaked; “Background Measurement”, residual background was measured much after a shot; and “High yield D-T Shot”, where the background was measured in the milliseconds to seconds after an ICF implosion. Highlighted in gold are the successful runs which were after high-yield D-T shots.

Run Number	Shot Number	Purpose	Parameters
1-5		Tuning Run	30 sec, 4 $\pi$ detector
6		Tuning Run	10 min, 4 $\pi$ detector, <sup>207</sup> Bi Source
7		Background Measurement	1 hr, 4 $\pi$ detector
8-10		Tuning Run	30 sec, Getter detector, <sup>207</sup> Bi Source
11		Tuning Run	10 min, Getter detector, <sup>207</sup> Bi Source
12		Background Measurement	10 min, Getter detector
13		Tuning Run	30 sec, 4 $\pi$ detector, <sup>207</sup> Bi Source
14		Tuning Run	10 min, 4 $\pi$ detector, <sup>207</sup> Bi Source
15		Background Measurement	10 min, 4 $\pi$ detector
16-20		Various Tuning	Varied Time, 4 $\pi$ detector
21	96181	High Yield D-T Shot	5 min, 4 $\pi$ detector, No shielding
22-29		Various Tuning	Varied Times, 4 $\pi$ detector
30	96184	High Yield D-T Shot	4 min, 4 $\pi$ detector, No shielding
31	96185	High Yield D-T Shot	220 sec, 4 $\pi$ detector, Lead Shielding
32-37		Various Tuning	Varied Time, Getter detector
38	96188	High Yield D-T Shot	5 min, Getter detector, Lead Shielding

### 3.7. Geant4 Simulations

After the 2019 <sup>41</sup>Ar and 2020 LLE experiments, several simulations of both the getter detector and the 4 $\pi$  turbopump trap detector were created using the GEANT4 software package [53]. These were done to further characterize the behavior of both detectors, provide an estimate of the fraction of the measured background that could be attributed to different sources, and give another estimate for the absolute efficiency of both detectors. Several source geometries were examined: a point source within the inner volume of the 4 $\pi$  detector or in front of the getter detector, radioisotopes dispersed isotropically in the air outside both detectors, radioisotopes dispersed isotropically within the 4 $\pi$  detector’s inner

volume, and radioisotopes found within the thin foil wrapping that was around each detector. The code randomly generates a radioisotope or particle event within a specified volume and then tracks the motion of the particles as they interact with materials in the simulation until they either leave the simulation area (a 400 mm cub centered on the relevant detector) or stop. Upon interaction with the detector, a timestamp of the interaction as well as the energy lost while interacting with the specific part of the detector is recorded. These energies are stored in a list file with the same format as the list files generated by the FemtoDAQ. This allows the simulation data to be analyzed in the same way that the experimental data.

Table 3. Table of LLE shot details. The attributes of all the shots conducted during the experiment, including the neutron yield, ion temperature, tested detector, and shielding configuration are listed for each shot. Highlighted in gold are the shots which were successfully measured.

Shot Number	Neutron Yield	T <sub>ion</sub> (keV)	Detector	Shielding	FemtoDAQ Timeout	Note
96175	1.04×10 <sup>14</sup>	9.28	4π Phoswich			FemtoDAQ crashed
96178			4π Phoswich			Trigger test, null shot
96179	1.34×10 <sup>14</sup>	9.51	4π Phoswich			Relays failed to close, FemtoDAQ okay
96180			4π Phoswich			Trigger test, null shot
96181	1.32×10 <sup>14</sup>	8.44	4π Phoswich	none	30 sec	Good
96183			4π Phoswich	none	30 sec	No data, FemtoDAQ memory filled?
96184	1.56×10 <sup>14</sup>	10.64	4π Phoswich	none	0.2 sec	Good
96185	1.50×10 <sup>14</sup>	8.68	4π Phoswich	lead	0.2 sec	Good
96186			Getter Phoswich			No FemtoDAQ trigger
96187			Getter Phoswich			Trigger test, null shot
96188	1.50×10 <sup>14</sup>		Getter Phoswich	lead	30 sec	Good

## Chapter 4

### ANALYSIS

#### **4.1. Introduction**

The 2-D histograms, decay curves, and growth curves from the 2019  $^{41}\text{Ar}$  Experiment and the LLE Ride-Along were used to characterize the behavior of both the getter and the  $4\pi$  detectors, as well as the processing electronics. In addition, the data from the LLE ride-along experiment was used to identify possible background sources. In this section, the results of the two experiments and an in-depth analysis will be given. Furthermore, a preliminary analysis of the results of GEANT4 simulations of both detectors will be given and compared to results obtained during both experiments.

#### **4.2. 2019 $^{41}\text{Ar}$ Experiment Results**

As described in Section 1.4.3, the purpose of the 2019  $^{41}\text{Ar}$  Experiment was to test whether the  $4\pi$  detector and processing electronics could detect the decay of a radioactive, inert gas trapped within its inner volume. A series of 30 s, 2 hr, and 10 hr counting periods were conducted using the method in described in Section 3.5. A region of the 2-D histogram was then selected, based on the region that contained the good beta events but not the background events (background events made up the dense regions of the bottom and the left side of the 2-D histogram) from the  $^{207}\text{Bi}$  calibrations (Figure 29). Figure 34 also shows this region as a green quadrilateral. The background events were most likely cosmic rays as well as possibly radiation from  $^{207}\text{Bi}$  and  $^{137}\text{Cs}$  test sources located at a distance. These events within the cut region were then counted, and the integral number of counts was plotted as a function of time. A silicon surface barrier detector was also affixed to the top of the 4-way cross seen near the top of the detector in Figure 31, to provide a baseline for comparison with the phoswich data to, as well as to be used in calculating the absolute efficiency of the phoswich detector. A NaI detector was also used to measure the gamma spectrum of the gas trapped within the phoswich detector and was placed against its rear wall (shown in Figure 31).



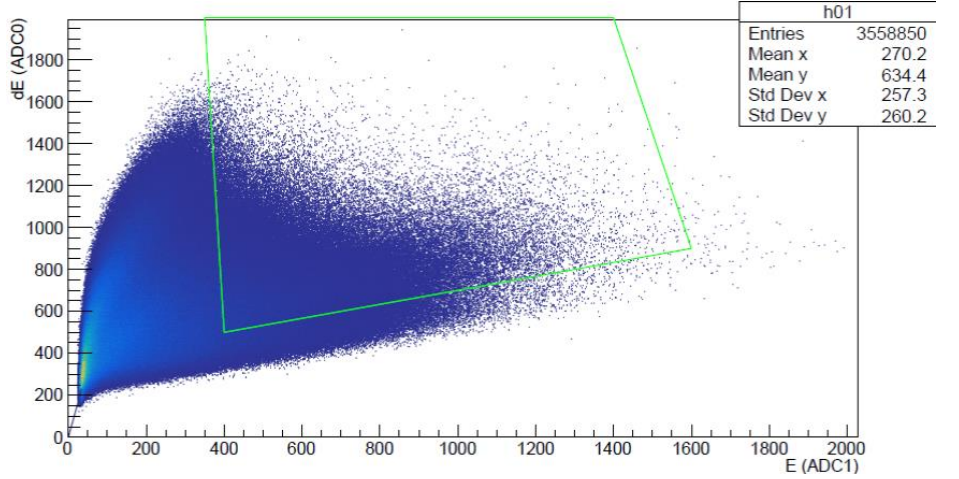


Figure 34. 2-D histogram of  $^{41}\text{Ar}$  decay from the  $4\pi$  phoswich detector. The green quadrilateral shows the region of the plot selected based on a  $^{207}\text{Bi}$  data calibration (like the one shown in Figure 29) that contains mostly good beta events. The 2-D Histogram is from a 2 hr counting run.

As previously mentioned, the events located within the green cut region in the 2-D histogram of each counting run (the 2-D histogram of an 2 hr counting period is shown in Figure 34) were then counted and a growth curve was plotted, which is shown in Figure 35. A sum of two growth curves, one for  $^{13}\text{N}$  and one for  $^{41}\text{Ar}$ , shown below.

$$N(t) = N_{\text{Ar}}(1 - e^{-\lambda_{\text{Ar}}t}) + N_{\text{N}}(1 - e^{-\lambda_{\text{N}}t}) + Ct. \quad (4.1)$$

Here,  $N_{\text{Ar}}$  is the total number of  $^{41}\text{Ar}$  decays detected (left to vary in the fit),  $\lambda_{\text{Ar}}$  is the decay constant for  $^{41}\text{Ar}$  (fixed in the fit),  $N_{\text{N}}$  is the total number of  $^{13}\text{N}$  decays detected (left to vary),  $\lambda_{\text{N}}$  is the decay constant of  $^{13}\text{N}$ , and  $C$  is a constant background rate (left to vary). Initially, the fit included just  $^{41}\text{Ar}$  decay, however, it became evident that another radioisotope was present with a half-life of around 10 min. This caused the fit to deviate from the data for times less than 20 min. It was determined that  $^{13}\text{N}$  was a likely candidate as  $^{12}\text{C}$  within the Kapton window of the gas cell could be turned into  $^{13}\text{N}$  via the  $^{12}\text{C}(d,n)^{13}\text{N}$  reaction which has a cross-section of about 200 mb [44] at the beam energy of 2.1 MeV, which an order of magnitude larger than the  $^{40}\text{Ar}(d,p)^{41}\text{Ar}$  reaction, which has a cross-section of about 25 mb at 2.1 MeV (as predicted by AZURE2 [41] and TALYS [29] using data from Ref. [45]). Once  $^{13}\text{N}$  was accounted for, a good fit was achieved. The fit was obtained by minimizing  $\chi^2$  using MINUIT [46] and the ROOT data analysis software [47]. To fit the growth curve equation to

the data, the following procedure was used. First, all variables were fixed at zero and the only variable allowed to vary was the constant background rate  $C$ , which was then fit to only the last minute of the run to ensure that the background constant was being obtained over a fit interval where background dominated the count rate. Second, the decay constant  $\lambda_{Ar}$  was fixed to a previously measured value of  $0.3795 \text{ s}^{-1}$  [48], the background rate  $C$  was fixed to the value determined in the previous step, and the number of  $^{41}\text{Ar}$ ,  $N_{Ar}$ , was left to vary. This was fit over the interval from 30 min to the end of the run. Lastly, all previous variables were fixed to the values determined in the previous steps, the decay constant of  $^{13}\text{N}$  was fixed to a previously measured value of  $0.0948 \text{ s}^{-1}$  [49], and  $N_N$  could vary. This process ensured that the value of each of the fit parameters would be determined by only looking at the intervals of time where each respective parameter had the greatest influence on the count total. This would provide a starting guess values for the fit. One these starting values were obtained, they were used as initial guesses for MINUIT and all fit parameters were allowed to vary. Through this process, the fit estimated that  $21,097 \pm 324$   $^{41}\text{Ar}$  decays and  $17,161 \pm 767$   $^{13}\text{N}$  decays were detected. Additionally, the fit found the two half-lives to be  $110.2 \pm 1.01$  min for  $^{41}\text{Ar}$  and  $10.2 \pm 0.89$  min which agree with previously measured values for the half-lives of  $^{41}\text{Ar}$  and  $^{13}\text{N}$  [48, 49].

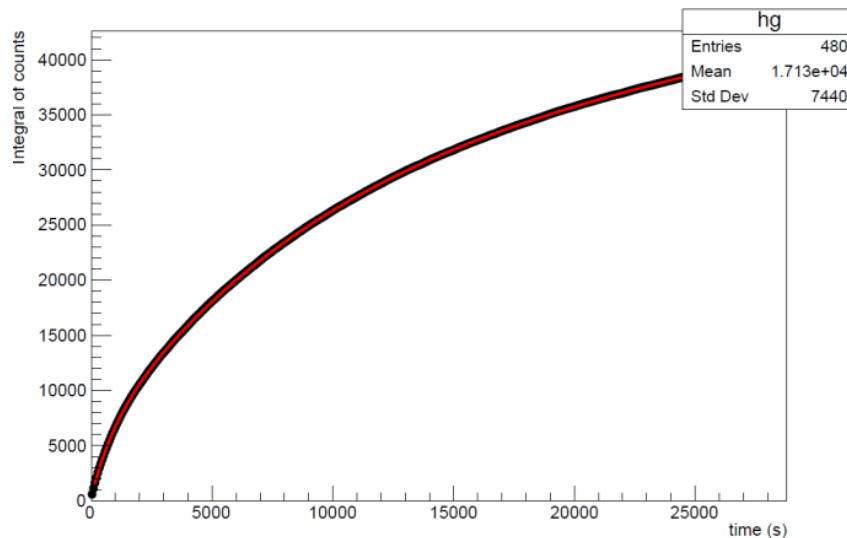


Figure 35.  $^{41}\text{Ar}$  growth curve from an 8 hr counting period with the  $4\pi$  detector. Data are shown in black, while the red curve shows Equation (4.1) fit to the data.

### **4.3. L.L.E. Ride-Along**

After the LLE ride-along experiment, an analysis code was written to allow isotopes present after the fusion shot to be identified, and to study the capabilities of the processing electronics and data acquisition system. There were several main questions which this experiment hoped to answer:

1. How would the detector electronics and data acquisition system respond to being exposed to the high count rates of primary radiation from a high-yield D-T shot? Would the isolation relay circuit would protect the electronics and successfully reconnect the detectors when a signal was received to from the control room? Would the PMTs and PMT bases would survive the initial EMP and primary radiation?
2. How high is the total count rate in the milliseconds to seconds after the shot? For the proposed methodology to be feasible, this background must be low enough allow the desired product nuclei decays to be identified and counted.
3. Will the data acquisition system and pulse separation electronics function correctly in this new environment?

Below is a description of the analysis code, a summary of the data analysis done on the shot data from the ride-along experiment, and preliminary answers to the questions above. Throughout the analysis, the design of the apparatus was considered and areas of the design that could be improved were noted.

#### **4.3.1. Assessment of Electronics and Detector**

Upon first analysis of the ICF data from both the  $4\pi$  and getter detector, several unexpected features were found. These features raised many questions about the behavior of the detector and the electronics in the high-count-rate environment immediately after the high yield D-T shots because these features were not present at low count rates. Several of these questions are listed below:

- Q1. Upon first inspection, large gaps in the decay curve exist and histogram binning does not appear to be correct. Why is this occurring and how can it be corrected?

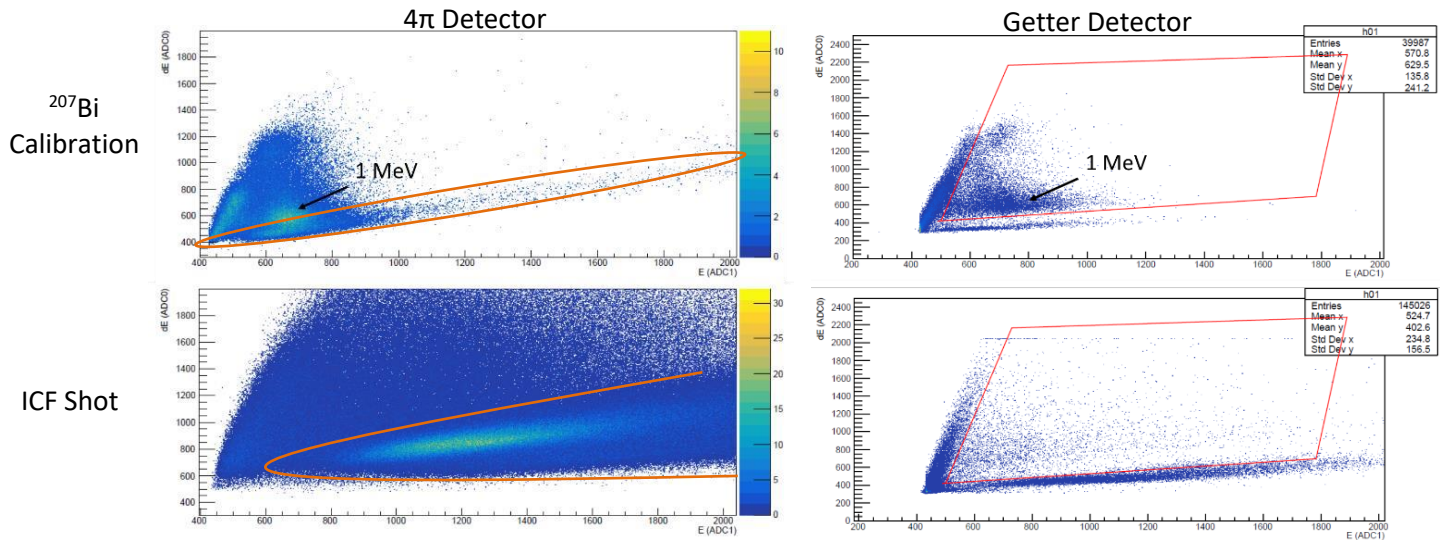


Figure 36. 2-D Histograms from shots 96184, 96188 and  $^{207}\text{Bi}$  Calibrations. The orange region in the  $4\pi$  detector data shows the large band of background events that deposit most of their energy in the E layer of the phoswich. The large E band (enclosed in orange) in the data from shot 96184, measured with the  $4\pi$  detector (bottom left), has shifted up 200 dE channels and has widened significantly when compared to the  $^{207}\text{Bi}$  calibration (top left). Additionally, shot 96188, measured with the getter detector, is shown (bottom right) compared to a  $^{207}\text{Bi}$  calibration (top right).

- Q2. The long band of high E value events in the 2-D E-dE histogram has widened and shifted to higher energies compared to background runs. This shift can be seen above in Figure 36. Why does this occur?
- Q3. How much time passes between the detector being powered on and the point at which the detector is counting at its full rate?
- Q4. Which radioisotopes are identifiable in the decay curve of the background? It might be expected that the background would be caused by the decay of radioisotopes that are created as a result of  $(n,*)$ ,  $(\gamma,*)$ , and  $(p,*)$  reactions with  $^{56}\text{Fe}$ ,  $^{16}\text{O}$ ,  $^{14}\text{N}$ , or  $^{27}\text{Al}$ , as these were the most abundant elements that were present in the immediate area of the detector and the most abundant projectiles from the fusion reactions.

Since the purpose of the LLE ride-along experiment was to see the behavior of the phoswich detectors in the environment after the shot, as well as test different components of the

processing electronics and data acquisition system at higher count rates, each of these questions will be further examined in the following sections.

#### 4.3.1.1. Question 1: Event Binning and Dead-Time Analysis

Most of the interesting features in the data were associated with the count rate. For the  $4\pi$  detector, a count rate of over 350,000 events/s was recorded in the first few seconds after the implosion. This resulted in the memory buffer of the FPGA filling within seconds, however, it took the FemtoDAQ about 30 s to successfully write out all the data stored within its buffer. This resulted in large intervals of deadtime. This issue was much more prevalent in data collected with the  $4\pi$  detector, as the larger volume of the detector resulted in more particles interacting with it, and hence much higher count rates. Additionally, at the beginning and end of the long read-out periods, collection abruptly started/stopped in the middle of a histogram time bin. This resulted in multiple empty and partially filled time bins, which are shown in Figure 37.

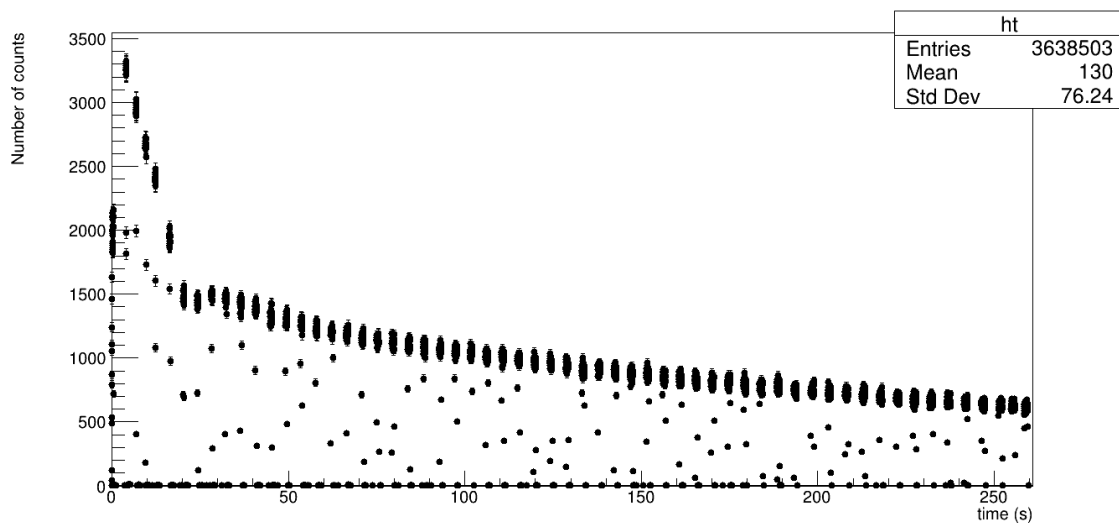


Figure 37. Improper binning which occurred due FemtoDAQ read-out time. The plot above is the raw decay curve from shot 96181, however this feature was present in all decay curves from shots using the  $4\pi$  detector. Figure 38 shows this decay curve and the decay curve for shot 96188 after the dead-time corrections.

This made obtaining a fit difficult, as these undefined bins skewed the fit. These bins were corrected by ignoring the empty bins and correcting the partially filled bins by weighting them by the inverse of the fraction of the bin that was filled with events.

That is,

$$N_{\text{corrected}} = \frac{NT}{t_2 - t_1}. \quad (4.2)$$

Here,  $N_{\text{corrected}}$  is the corrected number of counts in the bin,  $N$  is the number of events recorded in the bin,  $T$  is the width of the time bin, and  $t_1$  and  $t_2$  are the timestamps of the first and last events in the bin, respectively. Once these partially filled bins were corrected, the following deadtime correction was applied.

1. All events that were timestamped within  $3.5 \mu\text{s}$  of a previous event were discarded. The linear gate pulse stretchers held the separated pulses for  $3.5 \mu\text{s}$ , so any new event that came within this period would trigger with the correct timestamp but incorrect  $dE$  and  $E$  values, causing the previous event to just be digitized again. Let the number of these discarded events be  $N_2$ .
2. The time for the FemtoDAQ and FPGA to fully process an event and move onto the next event is roughly  $400 \text{ ns}$ . Therefore, the total deadtime can be written as

$$T_{\text{dead}} = \tau_1 N - \tau_2 N_2, \quad (4.3)$$

where  $N$  is the total number of events in a time bin of width  $T$ ,  $\tau_1 = 400 \text{ ns}$ , and  $\tau_2 = 3.5 \mu\text{s}$ .

3. The total number of events in the bins were corrected by weighting the number of events left in a bin,  $N - N_2$ , by the live-time fraction  $f_{\text{live}}$ :

$$N_{\text{corrected}} = \frac{N - N_2}{f_{\text{live}}} = \frac{(N - N_2)T}{T - \tau_1 N - \tau_2 N_2}, \text{ where } f_{\text{live}} = \frac{T - T_{\text{dead}}}{T}. \quad (4.4)$$

However, it should be noted that increasing the shielding around the detector to reduce counts is preferred to weighting the bins, as this reduces the total count rate, which will reduce overall dead-time. Shown in Figure 38 are the corrected decay curves of shots 96181 and 96184. Figure 38 also displays the long dead-time after each time the buffer of the FemtoDAQ is filled and needs to be read out.

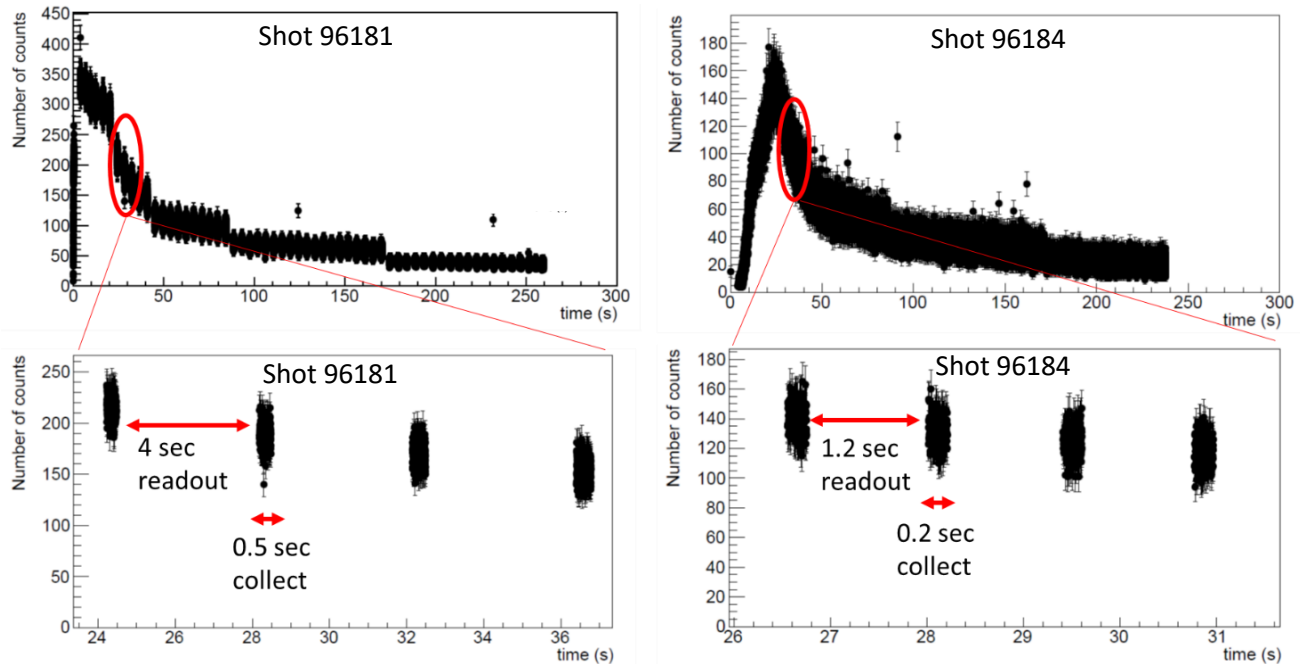


Figure 38. Decay curves showing dead-time due to FemtoDAQ readout time for two high yield shots. (Left) The decay curve for shot 96181 (using  $4\pi$  detector) shows the FemtoDAQ struggling to keep up with the high count rate. The buffer would fill after collecting for 0.5 s and the FemtoDAQ would then take 4 s to read out the data collected. (Right) The decay curve of shot 96184 (using  $4\pi$  detector). Before this shot, the FemtoDAQ collection time was constrained to 0.2 s and therefore did not fill the buffer, however, it still took about 1.2 s to read out the data collected.

The first step in reducing this dead-time was reducing the FemtoDAQ timeout. The FemtoDAQ could read out the data much faster if it did not have to suddenly handle its filled buffer. It is believed that this is due to the handshaking procedure between the FemtoDAQ and the FPGA; the system works much faster when it is read out at a scheduled interval than when it must first communicate that the buffer is filled and then read out. Additionally, making the FemtoDAQ timeout shorter resulted in fewer events in the buffer, also reducing the read-out time. Shown in Figure 39 is the decay curve from shot 96188, which used the getter detector, along with a plot of the live-time fraction as a function of time. The getter detector, due to its smaller volume and a lead brick being placed between the detector and the target chamber, reached a maximum count rate of only 18,000 events/s, this meant that the data buffer filled only once at about 7 s immediately after the shot, but did not fill again during any of the remaining 30 s counting intervals. After these periods, the FemtoDAQ took

about 3.5 s to read out the data collected. Even in the periods of highest count rate, a live-time fraction of 95% was held.

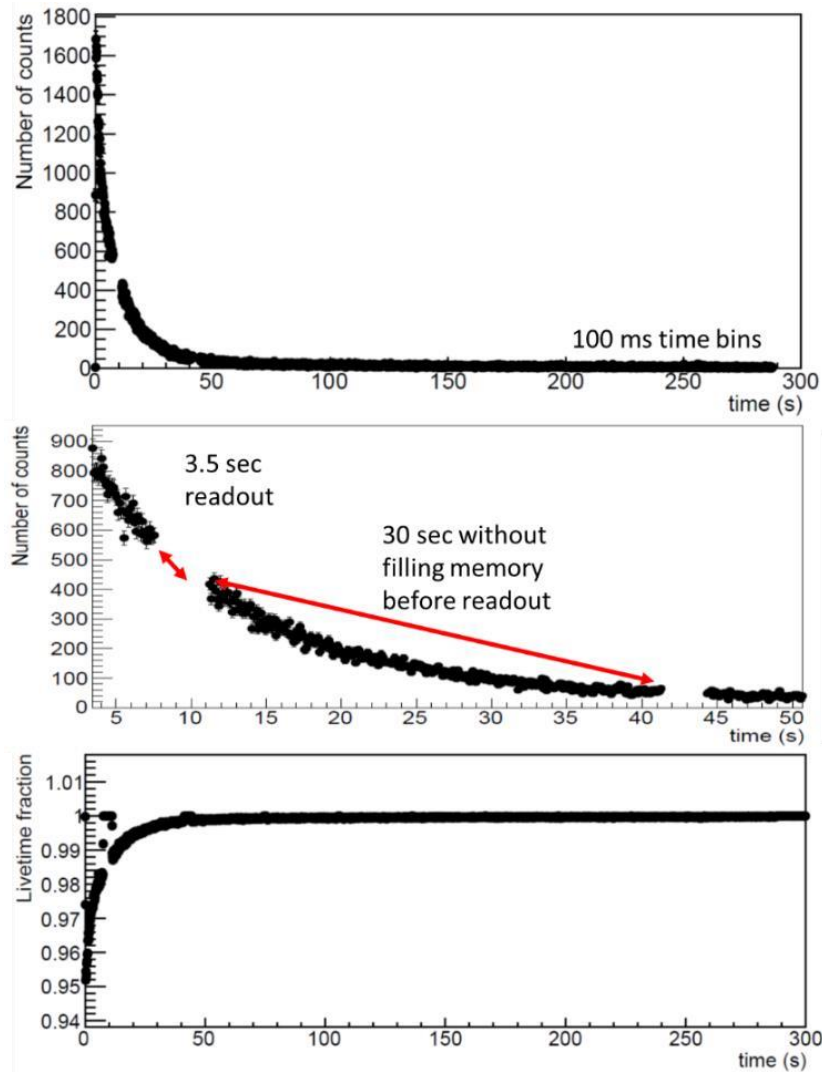


Figure 39. Getter detector decay curves and live-time fraction from shot 96188. (Top) The decay curve from shot 96188 with 100 ms time bins. Here, a lead brick was placed between the detector and the target chamber. (Middle) The decay curve from roughly 5 s to 50 s, showing the buffer fill at 7 s, then take 3.5 s to read out the data. Decays were then able to count for the full 30 s timeout period before being read out. (Bottom) The live-time fraction as a function of time. Even at the times of the highest count rate, the live-time fraction was 95% (read-out interval is ignored in this calculation).

#### 4.3.1.2. Question 2: Histogram Shape Over Time

Another consequence of the extremely high count rate in the seconds immediately after the implosion is event pile-up. This occurred when the electronics triggered on an event, but



multiple subsequent pulses also fell within the digitization window. With faster processing electronics this might not be so significant, however, the linear gates used in the processing electronics, LG105/N linear gates, date back to the late 1960s and have a long hold time of about 3.5  $\mu\text{s}$ . When another event occurred within 3.5  $\mu\text{s}$  of the previous event, the correct timestamp was recorded, however, the linear gates were still holding the previous event's pulse heights, so these same values were recorded again. This did not interfere with the decay curves, since the timestamp was recorded correctly, but drastically affected the shape of the 2-D histogram used for particle identification. To quantify the effect that event pile-up had on the shape of the dE, E, and 2-D histograms, as well as answer question Q2, the change in the histograms' shape over time was studied. The analysis code was modified to produce overlaid histograms, which consisted of normalized histograms from consecutive time intervals of equal length. This provided a qualitative picture of how the shape of the histograms changed throughout the collection period.

As seen in Figure 40, Figure 41, and Figure 42, the shape of the histograms changed considerably over time. The change shown in the overlaid histogram plots for shot 96188 (measured with the getter detector and had an initial rate of  $\sim 18,000$  counts/s) was most prominent when looking at the first 30 s of data collection when compared to any other later interval. This suggested that event pile-up caused by the high count rate may be the cause. All successfully measured high-yield D-T shots were then examined in this manner to see if this trend was found throughout. As seen in Figure 41 and Figure 42, the shape and position of the peaks do not appear to change as a function of time in the  $^{207}\text{Bi}$  measurements, however, in the data taken during D-T shots, the peak of the dE and E histograms shifted down and narrowed. The shape of the histogram might change due to several short-lived radioisotopes with different beta spectrums decaying within the first 30 s and disappearing before the later data was collected. However, because the shape of the histograms changes considerably after this period, it is suspected that pile-up is the chief cause. Currently, it is not known how much short-lived isotopes would effect the shape of the histograms in the first few minutes of counting, so this phenomenon should be examined further.

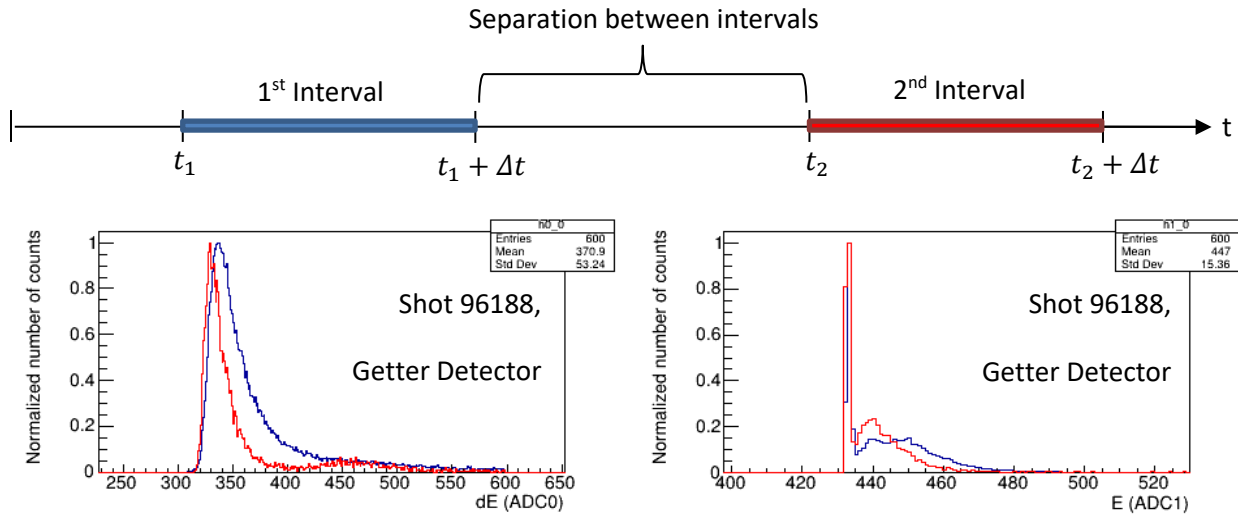


Figure 40. Time intervals and overlaid histograms. In order to assess how the histogram shape changed over time, two configurable, equal-length time intervals were compared. The analysis code plotted dE (left) and E (right) histograms for the first time interval from 0 to 60 seconds (blue) and from 120 to 180 seconds (red) for shot 96188 ( $t_1 = 60$  s,  $t_2 = 120$  s,  $\Delta t = 60$  s).

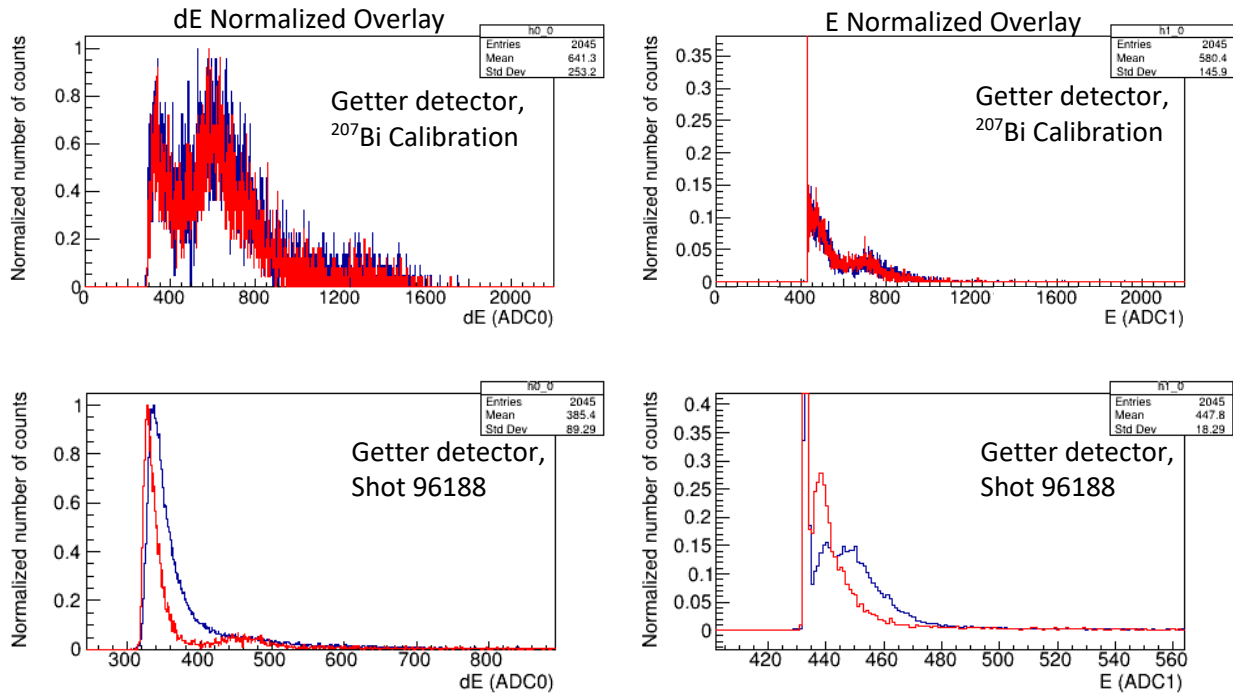


Figure 41. Shifting and widening of the dE and E histograms in getter detector runs. The normalized overlay of the dE (left) and E (right) histograms during the time intervals 0-100 s (blue) and 100-200 s (red) of multiple runs for shot 96188 (bottom), with a  $^{207}\text{Bi}$  run (top) for comparison.

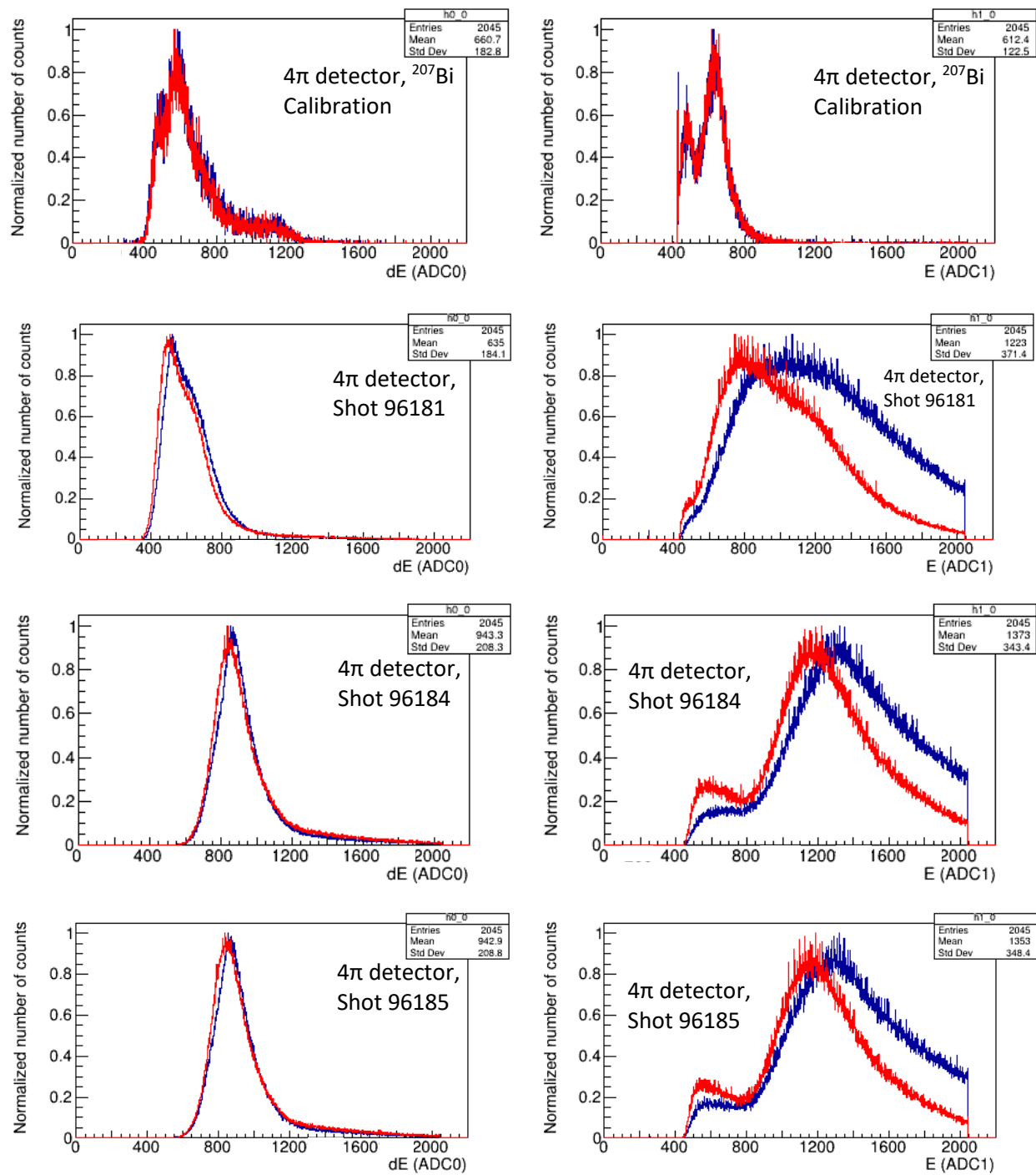


Figure 42. Shifting and widening of the dE and E histograms in 4 $\pi$  detector runs. The normalized overlay of the dE (left) and E (right) histograms during the time intervals 0-100 s (blue) and 100-200 s (red) of multiple runs for shots 96181 through 96185 with a  $^{207}\text{Bi}$  run (top) for comparison.

#### 4.3.1.3. Question 2: Sequential Event Analysis

To test the theory that event pile-up was the chief cause of the histogram shape change, histograms showing the difference between the dE and E values of sequential events were created. Recall that pile-up results in two sequential events having the same dE and E values if they occur within 3.5  $\mu$ s of each other. Therefore, if pile-up was occurring at a high rate, a plot of the difference between sequential events would show a large spike at a difference of zero. Such plots are shown in Figure 43 for the same runs as in Figure 41. The expectation is a gaussian-like distribution about some mean channel value, with peaking at the differences between the most common beta emission. However, in all the data gathered from D-T shots, a large, very sharp center peak that can be up to three times the height of the rest of the distribution is found. This peak has a full-width half-max of only 2-3 channels.

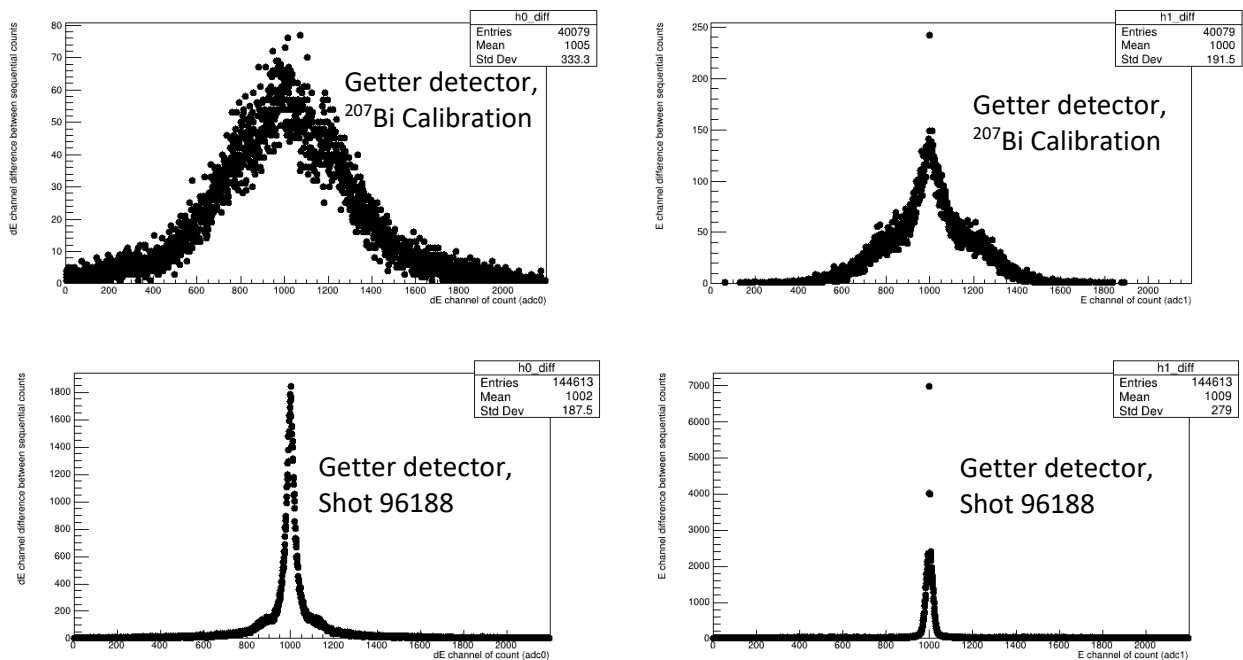


Figure 43. Sequential difference histograms for shot 96188 with the getter detector. These histograms show the channel difference in dE (left) and E (right) values between each event and the event before it. Histograms from the  $^{207}\text{Bi}$  calibration runs (top) are also included for comparison. Each histogram has been shifted by 1000 channels so that both the negative and positive differences are shown.

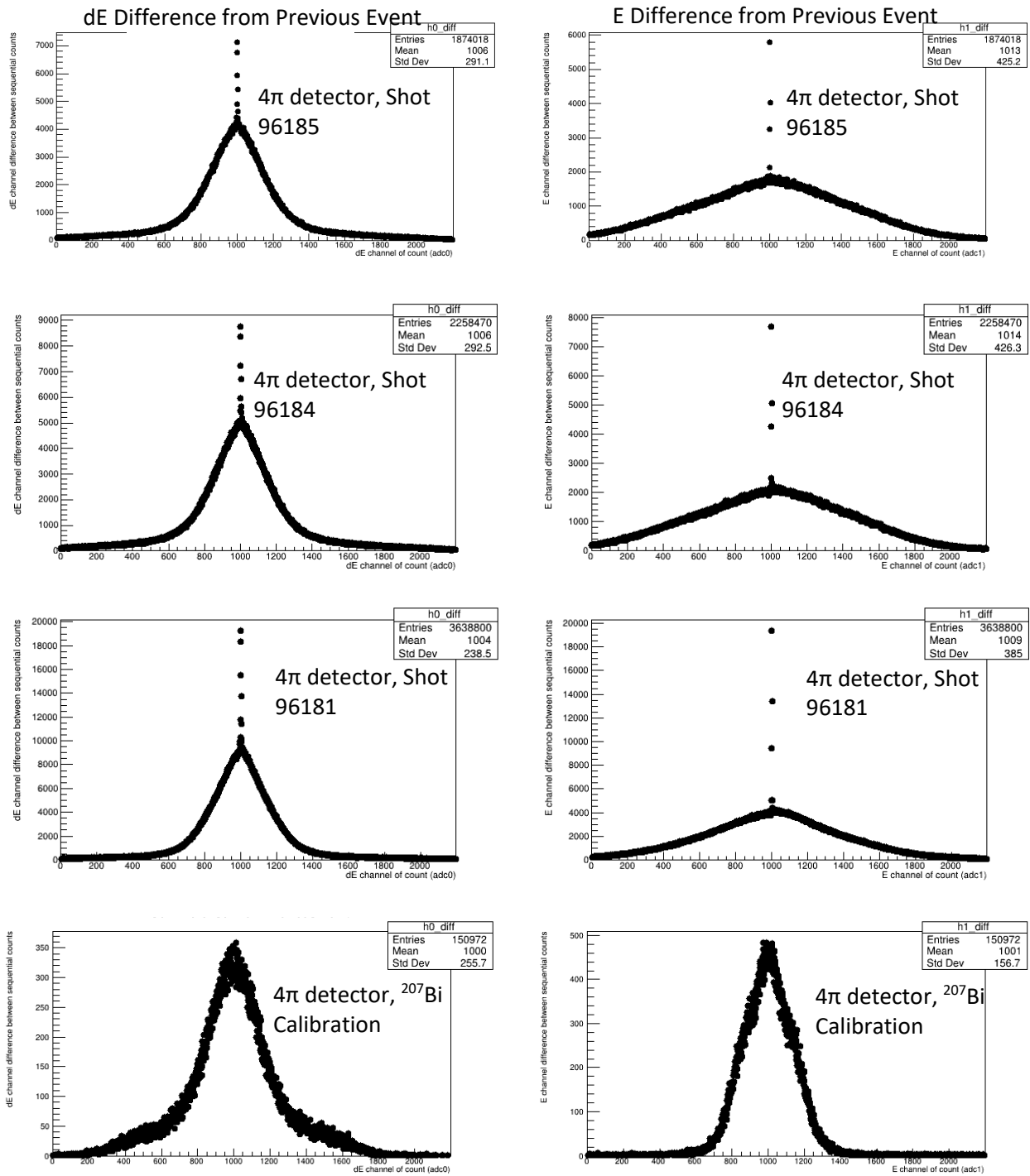


Figure 44. Sequential difference histograms for ICF shots with the 4 $\pi$  detector. These histograms show the channel difference in dE (left) and E (right) values between each event and the event before it. Histograms from the  $^{207}\text{Bi}$  calibration runs (top) are also included for comparison. Each histogram has been shifted by 1000 channels so that both the negative and positive differences are shown.

Since this peak is absent from the lower count rate runs that used the  $^{207}\text{Bi}$  source, it is evidence suggestive of event pile-up. Since the linear gate and stretcher pulse heights could have minor fluctuations, these large frequency peaks of only 2-3 channels wide would be expected if a single event was being digitized multiple times, when additional pulses that came within  $3.5\ \mu\text{s}$  of the initial pulses also triggered the acquisition system. The presence and size of these peaks can be used to estimate the amount of pile-up and the shift of the dE and E histograms early into the counting can be used to gauge the impact of the pile-up. The height of each of these central peaks can be used as a rough estimate of the number of pile-up counts.

#### 4.3.1.4. Question 3: Detector “Warm-Up” Time

The third major question that was to be answered in Section 4.3.1 was how long it took the detectors to begin counting once the isolating relays closed. From test runs before the ride-along experiment, immediately after both detectors’ construction, it was determined that the phototube and processing electronics associated with each detector had a warm-up time of around 2-3 ms. That is, once the detector is powered on, 2-3 ms would pass before the detectors would be functioning normally. However, during the ride-along experiment, it was found that this time highly varied between counting runs and detectors. On average, the time was also much longer than the predicted 2-3 ms. Knowing the warm-up time of the detectors is vital to the proposed methodology. The light-ion reactions of interest produce products that beta decay with half-lives on the order of a few hundred milliseconds to a few seconds. Therefore, the detector system must begin counting as soon as possible after the shot to measure the decay of the products in their first few half-lives. As shown in Figure 45, the time for the  $4\pi$  detector to begin counting at full rate varied from tenths of a second (shot 96181 had the buffer fill in just 0.5 seconds and counting did not resume until roughly 4 seconds later, so actual warm-up time may be close to 4.5 s), to up to 14 s after the relays closed. Additionally, the relays used (view Appendix A) have a close time of 3 ms, so counting cannot begin until after 3 ms, despite the detector and electronics configuration. The getter detector had a start-up time of around 0.2 s in the only successful run conducted with it. Since the relay close time of 3 ms is much less than the observed warm up time, it is currently believed that saturation of the scintillator in both of the detectors in the moments directly

after the shot is the chief cause of the delay. The PMT signal during this saturation would likely be one large sum peak from multiple pulses being generated close together. This sum pulse would then only trigger once, as it would appear as one large pulse to the processing electronics. Once the true count rate decreases, this phenomenon would become less frequent, and the measured count rate would increase. It is believed that this is what is causing the trend seen in the plots of Figure 45. This could prevent the PMT from producing distinct pulses for several seconds (like shining a bright light into the photocathode of the PMT) and even damage the photocathode over time. It is believed that more shielding around the detector could decrease the initial count rate due to the flux of radiation that is causing the saturation.

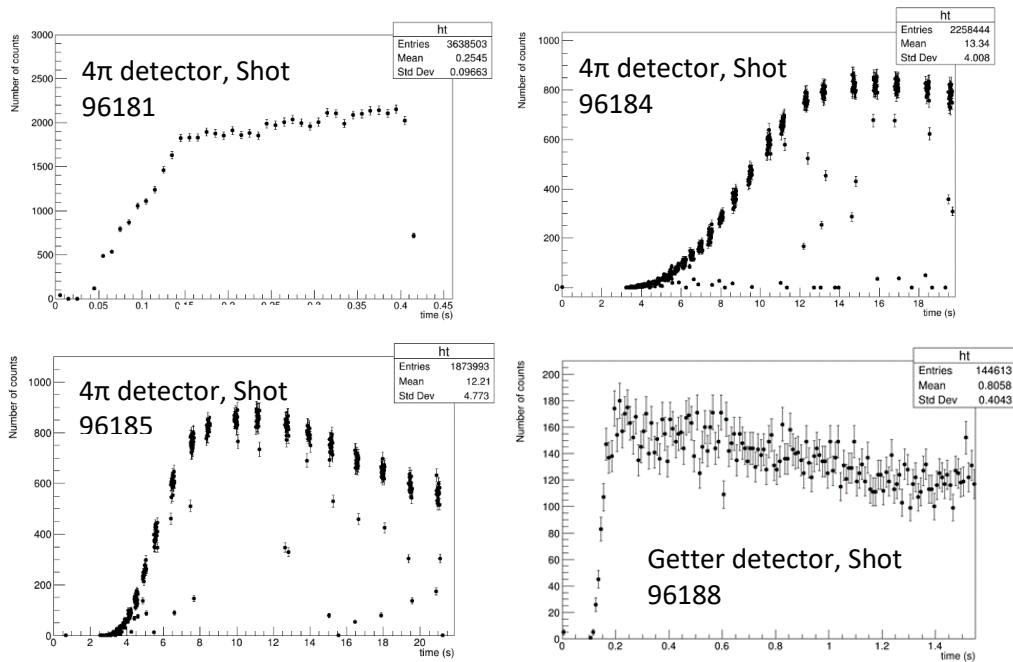


Figure 45. Initial start-up of the detectors. (Top left) The time spectra from shot 96181 with the  $4\pi$  detector, which shows the peak count rate occurring at 0.4 s. (Top right) The time spectra from shot 96184 with the  $4\pi$  detector, which shows a peak count rate at roughly 14 s. (Bottom left) The time spectra from shot 96185 with the  $4\pi$  detector, which shows a peak count rate at roughly 11 s. (Bottom right) The time spectra from shot 96188 with the getter detector, which shows a peak count rate at roughly 0.2 s.

Due to the high variability of the measured warm-up time and few runs to obtain an estimate from, it is difficult to give an exact value to the warm-up time of each detector, however, it can be concluded that in this configuration it is much longer than predicted.

#### 4.3.1.5. Question 4: Possible Background Sources

The next question is which radioisotopes, created from which activating materials in the environment, are responsible for the background. Because of the increased dead-time caused by the FemtoDAQ buffer filling up, only shot 96188, measured with the getter detector, produced a clean decay curve that could be fitted. The fit was obtained by minimizing  $\chi^2$  with MINUIT [46] (using the process of fitting each component of Equation (4.5), one at a time, as described in Section 4.2) and was the sum of three separate decay terms, one with a shorter half-life, and one with a longer half-life:

$$F(t) = N_0 e^{-\lambda_0 t} + N_1 e^{-\lambda_1 t} + N_2 e^{-\lambda_2 t} + B, \quad (4.5)$$

where  $N_k$  is the number of initial nuclei of species  $k$  with a decay constant of  $\lambda_k$  and  $B$  was a constant background rate. This equation was fit to the decay curve generated by the getter detector data (Figure 46 left) as well as the decay curve generated from just events within the cut region of the 2-D histogram (Figure 46 right).

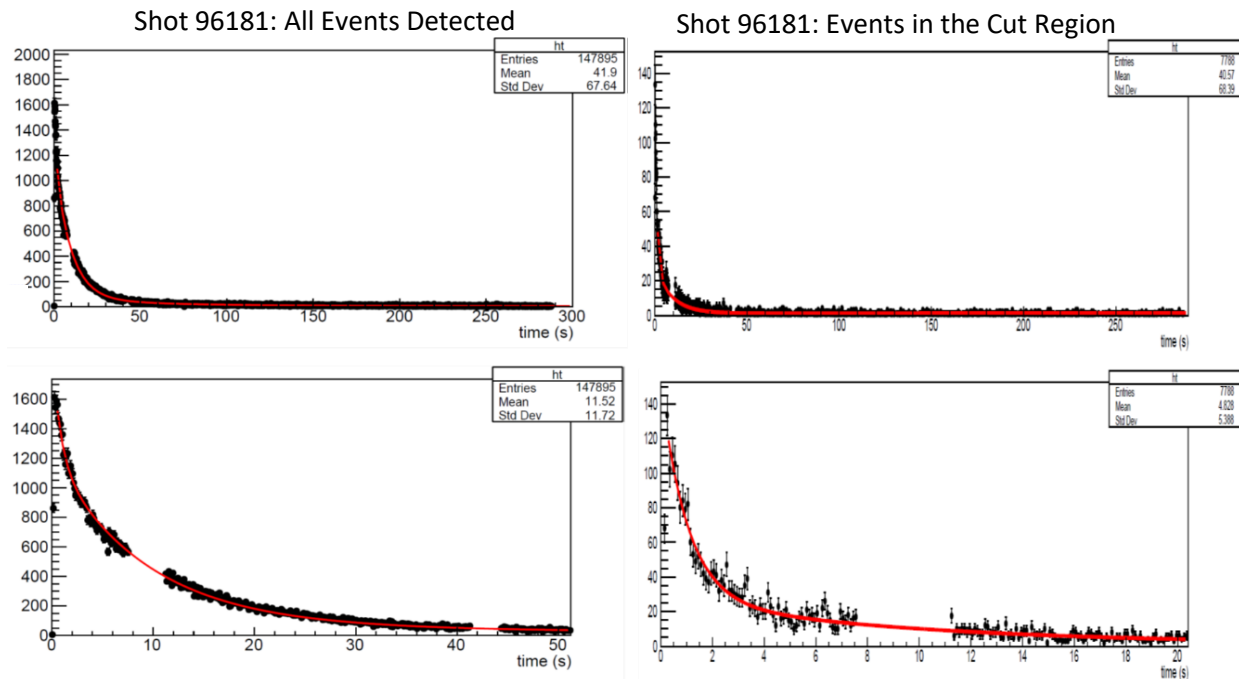


Figure 46. Fitted decay curves for shot 96188 with the getter detector. The red line represents the fit of Equation (4.5). (Left) The equation was fitted to all events detected and (right) just those in the cut region. Additionally, the equation was fitted to just the first 50 s for each set counting run (bottom plots). The three decay constants obtained in the fit corresponded to radioisotopes with half-lives of about 0.7 s, 7.0 s, and 60 s. A good fit to the events in the cut region did not require the use of the 60 s decay term.



The calculated best fit parameters are shown in Table 4. It is unknown how many and which individual radioisotopes were contributing the decay curves indicated, and identification of possible radio isotopes is currently underway. However, some preliminary analysis on the 7 s decay has been completed. As mentioned in Section 4.3.1, radioisotopes produced by (n,\*), (p,\*), and ( $\gamma$ \*) reactions with  $^{56}\text{Fe}$ ,  $^{16}\text{O}$ ,  $^{14}\text{N}$ , or  $^{27}\text{Al}$  were expected.

Table 5 shows the characteristics of radioisotopes that can be reached by these reactions and have half-lives of approximately 7 s.

Table 4. Best fit parameters for shot 96188. Best fit parameters for the decay curve of all measured events and for events within the beta particle cut region.

Component	All Measured Events		Cut on $\beta$ Events	
	$T_{1/2}$ (sec) = $\ln(2)/\lambda$	N	$T_{1/2}$ (sec) = $\ln(2)/\lambda$	N
1	0.76	728	0.73	115
2	7.13 (fixed)	1080	7.13 (fixed)	23
3	59	40	Not needed	

Table 5. Table of possible radioisotopes detected. Shown are radioisotopes that could be created from (n,\*) reactions that have a reactant that would be present within the environment around the detectors, product half-lives comparable to those found in the fit of the shot 96188 data, and thresholds below the 14.1 MeV energy of D-T fusion primary neutrons. Threshold energies calculated using NNDC's QCalc [50] and cross sections obtained from the NNDC EXFOR Database [11].

Isotope	Half Life (s)	Decay Const. (1/s)	Mode	Reaction	Threshold (MeV)	CS (mb)	Source
$^{26}\text{Al}$	6.346	0.10923	EC, $\beta^-$	$^{27}\text{Al}(n,2n)^{26}\text{Al}^*$	13.546	8.48 at 14.1 MeV	Target Chamber, $^{27}\text{Al}$ bar, $^{27}\text{Al}$ foil
$^{16}\text{N}$	7.130	0.09722	$\beta^-$	$^{16}\text{O}(n,p)^{16}\text{N}$	10.25	42 at 14.1 MeV	Air

It was found that both the decay of  $^{26}\text{Al}$  in its first excited state (a  $0^+$  state with a half-life of 6.34 s) generated through the  $^{27}\text{Al}(n,2n)^{26}\text{Al}^*$  reaction and  $^{16}\text{N}$  generated by the  $^{16}\text{O}(n,p)^{16}\text{N}$

could be responsible for the 7 s component of the decay. Their decay schemes are shown in Figure 47. Though the cross section of  $^{16}\text{O}(n,p)^{16}\text{N}$  [51] is five times larger than that of  $^{27}\text{Al}(n,2n)^{26}\text{Al}^*$  [52] at 14.1 MeV, it is possible that the detector may be more sensitive to the  $^{26}\text{Al}^*$  decays, as aluminum was much closer to the detector than a majority of the air in the room. For this reason, both  $^{16}\text{N}$  and  $^{26}\text{Al}^*$  decays are being investigated.

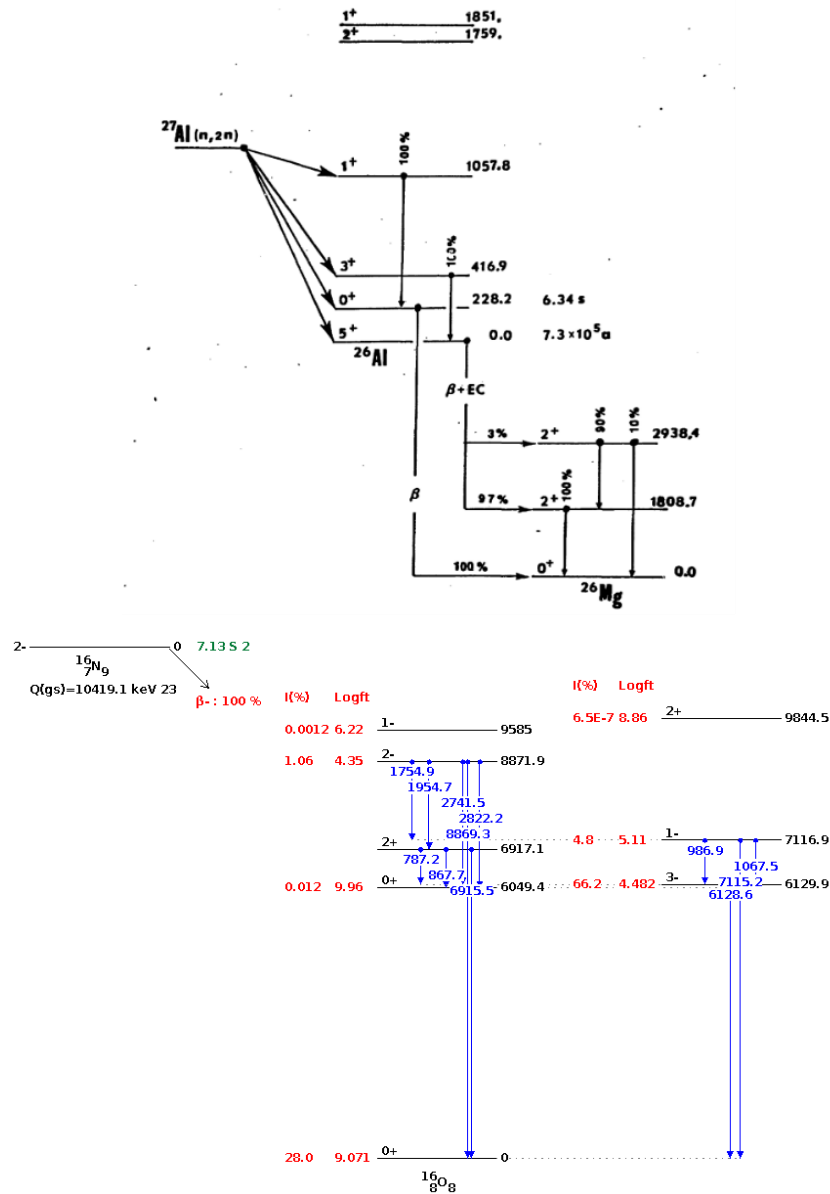


Figure 47. Decay diagrams of  $^{26}\text{Al}^*$  and  $^{16}\text{N}$ . The (Left)  $^{26}\text{Al}^*$  decay diagram, taken from Ref. [52]. In its 0<sup>+</sup> excited state,  $^{26}\text{Al}$  decays 100% of the time by positron emission to the ground state of  $^{26}\text{Mg}$ . (Right)  $^{16}\text{N}$  decay diagram, generated using Ref. [11]. In its ground state,  $^{16}\text{N}$  decays by beta emission to the ground state of  $^{16}\text{O}$  28% of the time, and to the 3<sup>-</sup> state 66.2% of the time.

#### 4.4. *GEANT4 Simulations*

After determining some possible candidates for the observed background, it was decided that a simulation of the detectors would be used to predict the count rates expected due to the  $^{16}\text{N}$  and  $^{26}\text{Al}^*$  produced in materials near the detector. This could then be compared with the measured rates. A simulation, written in C++ with the GEANT 4 [53] toolkit, a software package developed by CERN that uses Monte-Carlo simulations to model the passage of particles through matter, was developed so that particles from the decays of multiple different species of radioisotopes in different geometries around the detector could be examined. This simulation data was then exported into a format readable by the ROOT analysis code used for the LLE ride-along data. The simulation included several possible source geometries, including a point source within an aluminum holder to simulate a  $^{207}\text{Bi}$  source, the air outside the detector (the simulation volume was a 400 mm cube centered on the detector), the air inside the  $4\pi$  detector, an Al bar beneath the detectors, and the volume of a 0.016 mm thick  $^{27}\text{Al}$  foil wrapped around the getter detector. The  $^{27}\text{Al}$  foil wrapping on the large detector has been modeled, however the ability to select this region as a source for decays has yet to be implemented. The simulation also had configurable parameters for simulating pile-up (which needs to be investigated further) and crosstalk between the dE and E channels. This cross talk is a result from the processing electronics not completely separating the fast and slow pulses from the PMT signal and causes the the dE and E values to be mixed, as seen in the 2-D histograms (recall how the edges in the histograms of Figure 36 are not parallel with the axes).

##### 4.4.1. Getter Detector

The getter detector, wrapped in 0.016 mm thick  $^{27}\text{Al}$  foil, was modeled for  $^{207}\text{Bi}$  decays from a point source in front of the detector,  $^{16}\text{N}$  decays in the air outside the detector, and  $^{26}\text{Al}^*$  decays in the  $^{27}\text{Al}$  bar and foil. The detector was simulated with 10% crosstalk and the results of these simulations were compared to the measurements taken at LLE. Figure 49 shows a comparison of a  $^{207}\text{Bi}$  calibration run with the getter detector to a  $^{207}\text{Bi}$  point source simulated in front of the getter detector.

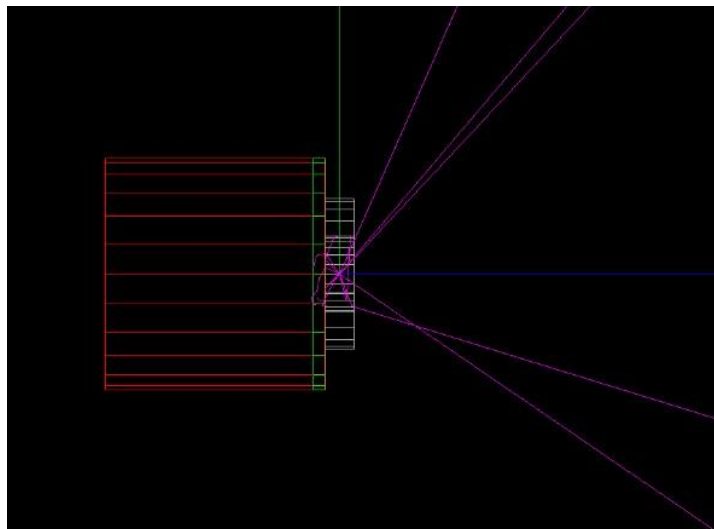


Figure 48. GEANT4 Getter Detector Rendering. A wireframe rendering of the getter detector and source produced by the GEANT4 simulation with the slow scintillator in red, fast scintillator in green,  $^{207}\text{Bi}$  source holder in grey, and simulated particle tracks in purple.

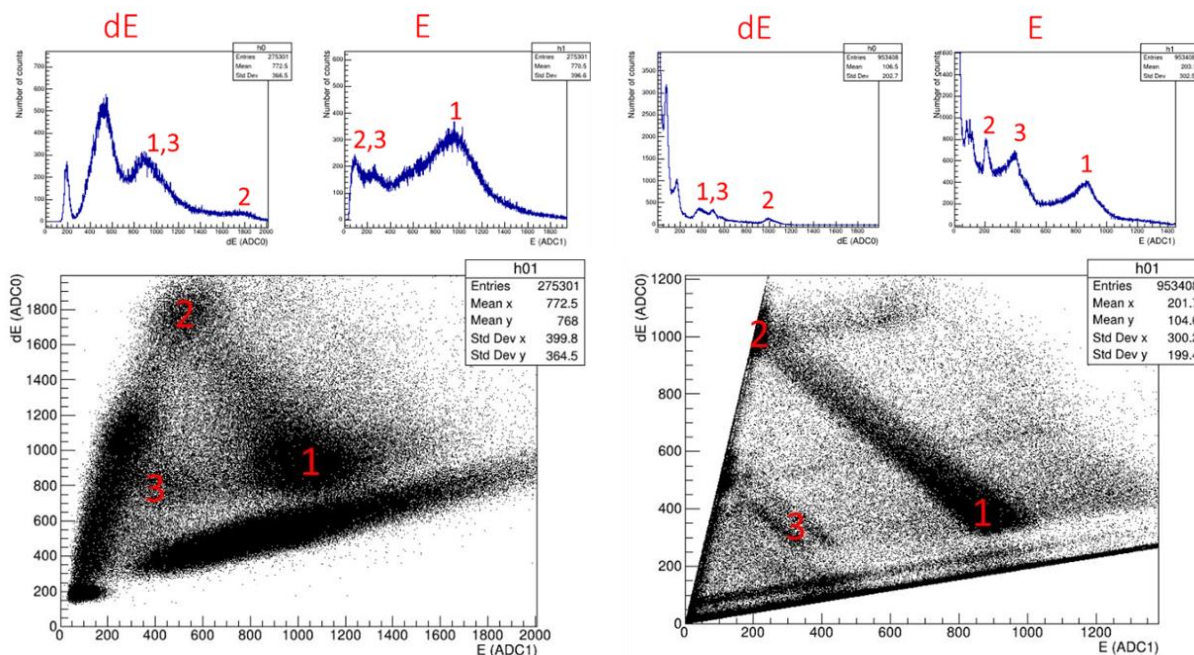


Figure 49. Getter detector  $^{207}\text{Bi}$  simulation comparison. (Left) Singles spectra and 2-D histogram for a  $^{207}\text{Bi}$  calibration run on the getter detector. (Middle) Singles spectrums and 2-D histogram from a simulation of 1,000,000  $^{207}\text{Bi}$  decays from a point source the same distance in front of the getter detector. Regions of interest and their corresponding peaks on the singles spectra are labeled 1 through 3: 1 denotes what are believed to be 1.063 MeV betas, 2 denotes 1.063 MeV betas which hit the dE layer at an oblique angle, and 3 denotes roughly 570 keV betas (reference Figure 22 for  $^{207}\text{Bi}$  decay scheme). As shown above all three features are present in both the data and the simulation.

#### 4.4.2. $4\pi$ Detector

In a similar manner to the getter detector, the  $4\pi$  detector was simulated. The detector was also modeled wrapped in 0.016 mm thick  $^{27}\text{Al}$  foil, but a new source geometry was added: the inner volume of the detector. Figure 50 shows the simulated detector. The results found were used to calculate the expected number of  $^{16}\text{N}$  that would be detected per shot. Further simulations of the  $4\pi$  detector to include the decay of  $^{26}\text{Al}^*$  within the  $^{27}\text{Al}$  foil wrapping must be performed in order to determine the significance of the  $^{27}\text{Al}(n,2n)^{26}\text{Al}^*$  background in shots 96181, 96184, and 96185.

#### 4.4.3. Calculating Expected Decays

These simulations are still being analyzed to estimate the absolute efficiency of the detector, as well as its relative sensitivity to different background radiations from sources from different directions.

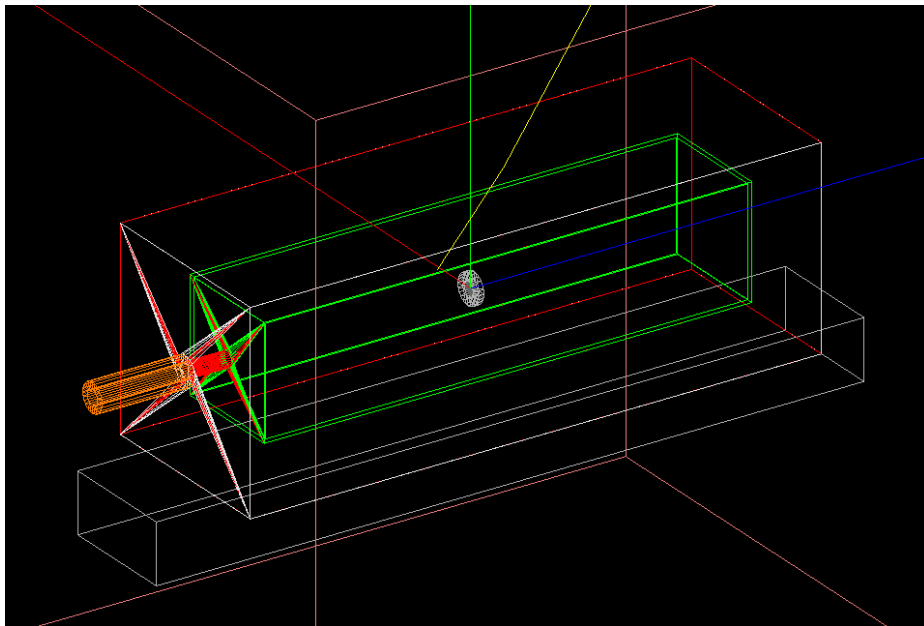


Figure 50.  $4\pi$  Detector simulation. A wireframe diagram of the  $4\pi$  detector with the slow scintillator (red), fast scintillator (green), aluminum vacuum flange (orange),  $^{27}\text{Al}$  foil (wrapped around the entire detector) and  $^{27}\text{Al}$  bar (grey),  $^{27}\text{Al}$  point source holder(white), and simulated particle track (yellow).

However, since the neutron yield for each shot is known, an estimate of the expected number of  $^{16}\text{N}$  and  $^{26}\text{Al}^*$  can be calculated by hand. Equation (2.1) can be rewritten as a function of

the cross-section of the reaction  $\sigma$ , the number density of target nuclei  $n_t$ , the volume of the target  $V$ , and the flux of the projectiles  $F_p = \frac{N_p}{A}$ :

$$N = \sigma \frac{N_p N_t}{A} = \sigma F_p n_t V. \quad (4.6)$$

The flux  $F_p$  at distance  $d$  from the point where the projectiles are emitted is the number of projectiles per unit area. Assuming the projectiles are emitted isotropically from the source, the flux is

$$F_p = \frac{N_p}{4\pi d^2}. \quad (4.7)$$

Furthermore, the number density of target nuclei is equal to

$$n_t = \frac{\rho_t}{A_t}, \quad (4.8)$$

where  $\rho_t$  is the mass density of the target material and  $A_t$  is the atomic mass of the a target nucleus. Therefore, assuming that the target has uniform density the number of reactions  $N$  in a given target volume  $V$  is then

$$N = \sigma \frac{N_p \rho_t}{4\pi d^2 A_t} V. \quad (4.9)$$

Equation (4.9) was used to calculate the number of  $^{16}\text{N}$  and  $^{26}\text{Al}^*$  generated in shot 96184, which had a neutron yield of  $1.56 \times 10^{14}$  and detectors 2.4 m from target chamber center (TCC), and in shot 96188, which had a which had a neutron yield of  $1.50 \times 10^{14}$  and detectors 2.4 m from TCC. The yields of these isotopes were multiplied by the detection fraction obtained from getter detector and  $4\pi$  detector simulations. The predicted detected decays were then compared to the measured decays from shots 96184 and 96188 in Table 6. As seen above in Table 6, the predicted number of detected decays is an order of magnitude lower than the measured number at 0.2 s for the getter detector. However, the values are much closer for the  $4\pi$  detector at 30 s.

Table 6. Expected  $^{26}\text{Al}^*$  and  $^{16}\text{N}$  based on GEANT4 simulations. Using the neutron yield and Equation (4.9), the estimated number of  $^{26}\text{Al}^*$  and  $^{16}\text{N}$  produced by shot 96188 for getter detector rows, and shot 96184 for  $4\pi$  detector rows, is shown below. Using the simulation, values for the number of  $^{26}\text{Al}^*$  and  $^{16}\text{N}$  detected per million from different environmental sources were predicted for both detectors. Using these values, the predicted number of decays of each isotope detected per shot was calculated and compared to the measured values. The simulation of the  $4\pi$  detector with the foil wrapping is not complete at this time, so no  $^{26}\text{Al}^*$  values are listed.

	$^{26}\text{Al}$ in Foil	$^{26}\text{Al}$ in Bar	$^{16}\text{N}$ Inside	$^{16}\text{N}$ Outside
Getter Detector	1,802	$5.05 \times 10^7$		$3.49 \times 10^7$
$4\pi$ Detector	198,800	$5.05 \times 10^7$	250,600	$3.40 \times 10^7$
Detected decays per million simulated				
Getter Detector	37,740	382		164
$4\pi$ Detector		1,360	4,500	477,000
Predicted number of decays detected				
Getter Detector	67	19,300		5,720
$4\pi$ Detector		68,900	1,128	$1.56 \times 10^7$
Predicted number of decays detected per 10 ms				
Getter Detector at 0.2 s	~1	21		5
$4\pi$ Detector at 30 s		3	~1	853
Measured number of decays 96184 per 10 ms				
Getter Detector at 0.2 s		~180		~180
$4\pi$ Detector at 30 s		~1450		~1450

One explanation of this is that short-lived isotopes make up a large fraction of the background within the first few seconds after the shot, but  $^{26}\text{Al}^*$  and  $^{16}\text{N}$  make up a larger portion of the background after this period. This comparison would be worth revisiting after a future ride-along experiment that is better equipped to deal with the high initial count rate, as such an experiment would provide a clearer insight into the background in the milliseconds to seconds after the shot.

#### 4.4.4. Correcting Crosstalk

The next step in analyzing the data from the ride-along would be to calibrate the energy scales for the dE and E scintillators. This would provide further insight into what background

sources are present by allowing the singles spectra on an absolute energy scale to be compared with the spectra of various other radioisotopes. However, one issue that was briefly mentioned in Section 4.4 is the presence of crosstalk. It is estimated that there is about a 10% crosstalk between the dE and E channels, caused by the overlap of the slow and fast components of each PMT pulse. Unless it is specifically instructed to, the GEANT4 simulation does not simulate crosstalk, so it can be used as a basis upon which to transform the experimental data to remove crosstalk.

Referencing Figure 49, three features were labeled within the data and the simulation. These three features were  $\sim 1$  MeV conversion betas,  $\sim 1$  MeV conversion betas from oblique angles, and  $\sim 500$  keV conversion betas (view Figure 22 for the conversion spectrum and decay scheme of  $^{207}\text{Bi}$ ). Consider drawing vectors from the origin to each of these features, as shown in Figure 51. A transformation matrix based on how vectors  $\vec{1}$ ,  $\vec{2}$ , and  $\vec{3}$  transform can then be constructed which transforms  $\vec{1}$ ,  $\vec{2}$ , and  $\vec{3}$  into  $\vec{1}'$ ,  $\vec{2}'$ , and  $\vec{3}'$ , the same vectors but without crosstalk. To create this transformation a three-point calibration was used. In general, the transformation can be expressed as a matrix M which satisfies

$$M(\vec{2} - \vec{2}') = (\vec{2}' - \vec{2}'), M(\vec{3} - \vec{2}') = (\vec{3}' - \vec{2}'), \quad (4.10)$$

$$\text{and } M(\vec{1} - \vec{2}') = (\vec{1}' - \vec{2}').$$

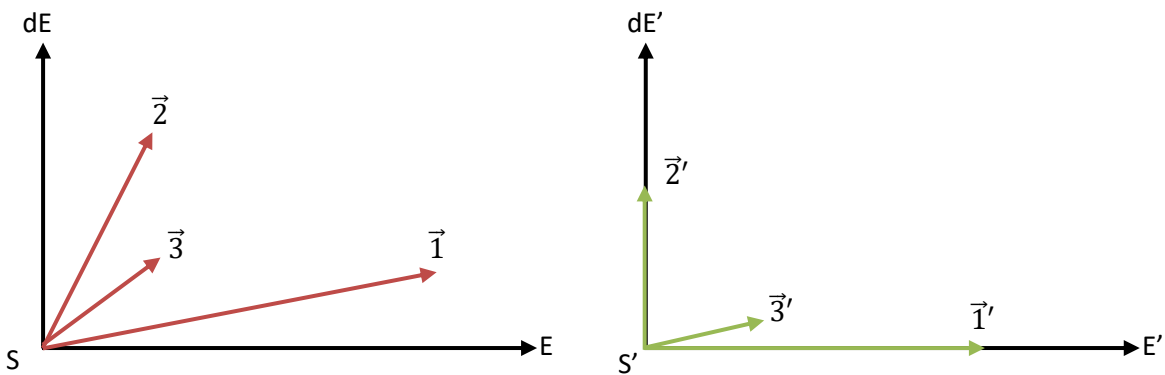


Figure 51. Experimental data basis and simulation basis. (Left) the coordinate system of the experimental data with three vectors pointing towards 1MeV betas ( $\vec{1}$ ), oblique 1 MeV betas ( $\vec{2}$ ), and  $\sim 500$  keV betas ( $\vec{3}$ ). (Right) The coordinate system of the simulation, which has no cross talk, pointing to the same three features in a coordinate system without crosstalk.



This comes from shifting vector  $\vec{1}$  to the origin in both spaces and then ensuring that M takes each vector to its primed version. Thus, for any vector  $\vec{x}$ , in general,

$$\vec{x}' = M(\vec{x} - \vec{2}) + \vec{2}'. \quad (4.11)$$

In order to find the elements of the transformation matrix, the system of Equations (4.10) must be solved. Upon solving, the elements  $m_1, m_2, m_3, m_4$  are found and the general equation to transform a point of the experimental data into a coordinate system with no cross talk is

$$\begin{aligned} \vec{x}' = & (m_1(x_E - 2_E) + m_2(x_{dE} - 2_{dE}) + 2'_E)\hat{E}' \\ & + (m_3(x_E - 2_E) + m_4(x_{dE} - 2_{dE}) + 2'_{dE})\hat{dE}'. \end{aligned} \quad (4.12)$$

This transformation was then applied to a  $^{207}\text{Bi}$  calibration run (Figure 52). However, the initial vectors in Figure 51 must be chosen by hand for each 2-D histogram and a new matrix M must be generated.

This transformation was then applied to a  $^{207}\text{Bi}$  calibration run. The original 2-D histogram, and the transformed histogram are shown in Figure 52. Interestingly, even after the transformation, which aligned vectors  $\vec{1}'$ ,  $\vec{2}'$ , and  $\vec{3}'$  as intended, the lower E band had a positive slope. Because of this, this method of correcting for crosstalk and calibrating the energy spectrum is worth investigating further.

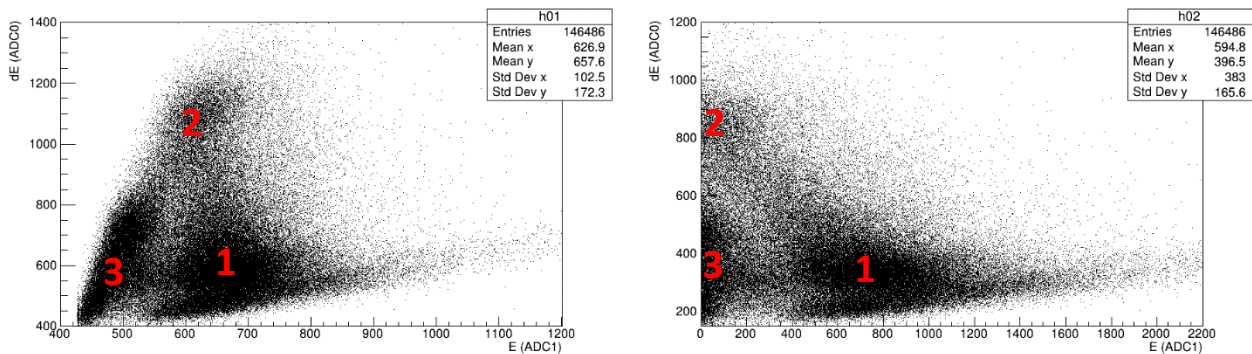


Figure 52.  $4\pi$  detector crosstalk correction comparison. (Left) The 2-D histogram from a 10 min  $^{207}\text{Bi}$  calibration run on the  $4\pi$  detector. (Right) The same run, but transforming the events using the using the crosstalk correction found in Equation (4.12). The correction was shifted up 200 dE channels so that the background band along the E axis can be seen.

## Chapter 5

### CONCLUSION

#### **5.1. Introduction**

In this section the primary conclusions drawn from the  $^{41}\text{Ar}$  experiment and the LLE ride-along will be given. Additionally, a future experiment designed to measure collection fraction for the proposed collection methods, a future LLE ride along, experiment and efforts to improve the data acquisition system will be discussed.

#### **5.2. Summary of Results**

Analysis of the 2019  $^{41}\text{Ar}$  experiment and the LLE ride-along experiment served as proofs of concept for the proposed methodology. The detection of  $^{41}\text{Ar}$  and  $^{13}\text{N}$  (Section 4.2) showed that the  $4\pi$  detector and processing electronics were functioning correctly and could be used to identify and count the decay of inert radioactive gasses within the  $4\pi$  detector's inner volume. This also showed the detector could hold gas within its inner volume for multiple hours without losing a significant amount.

Additionally, the LLE ride-along experiment has yielded three primary conclusions. The first conclusion was that the overall count rate peaked at 350,000 counts/s for the  $4\pi$  detector and 18,000 counts/s for the getter detector. This high count rate caused the data buffer to fill quickly and introduced long of dead intervals while the data was being read out. However, referencing Table 1, the light-ion reactions of interest would produce anywhere from  $10^5$  to  $10^7$  product nuclei per shot, and if the amount of product nuclei trapped is 1% (consistent with the solid angle of the getter detector) and the absolute efficiency of the detector is near 100%, then a desired product with a one-second half-life trapped by proposed apparatus would produce 500,000 decays within its first half-life. This leads to the second conclusion: for the getter detector, this number is large compared to the background. However, the same cannot be said for the  $4\pi$  detector. This means that the getter detector could potentially be used to measure such a decay. However, several differences between the ride-along's apparatus and the apparatus of the proposed methodology exist: the getter detector would

be placed within the target chamber instead of outside of the chamber and the  $4\pi$  detector would be further shielded from secondary radiation coming from outside of its volume. The final major conclusion is that the apparatus must be adjusted to reduce dead-time and the effects of pile-up in the data. Improvements in the processing electronics such as an FPGA with more memory and faster read out capabilities and linear gates with a shorter hold time would help with this. Additionally, setting the window of the processing electronics to 500 ns would allow for a higher count rate without pile-up; digitized pulses could be read out as they were digitized, relieving the issues associated with having a data buffer; and fits accounting for pile-up could be used to analyze the data.

### **5.3. Future Experiments**

One question that remains unanswered by the two experiments discussed in this paper is the question of what fraction of the product nuclei can be trapped and counted. This question is a complicated and depends on many factors of the chosen detector's design and the chosen collection method, among other factors. Therefore, the best way to answer this question directly is through experiment. Though, this could potentially be simulated and then verified by experimental results.

#### **5.3.1. Exploding Wire Experiment**

In collaboration with SUNY Geneseo, an experiment is being designed that would measure the collection fraction for several collection methods. The proposed experiment consists of a thin wire or foil coated with or composed of a desired target material that would be activated via  $(d,*)$ ,  $(p,*)$ , or  $(n,*)$  reactions generated using SUNY Geneseo's Tandem Pelletron Accelerator. This wire or foil would be suspended in the center of the Houghton College test chamber and heated or vaporized using a large current pulse. If done quickly enough, this could produce a roughly isotropic expanding radioactive gas which could then be collected via the collection methods discussed in Section 1.3. Figure 53 shows a diagram of the proposed experiment and Table 7 is a listing of the possible reactions that could be used.

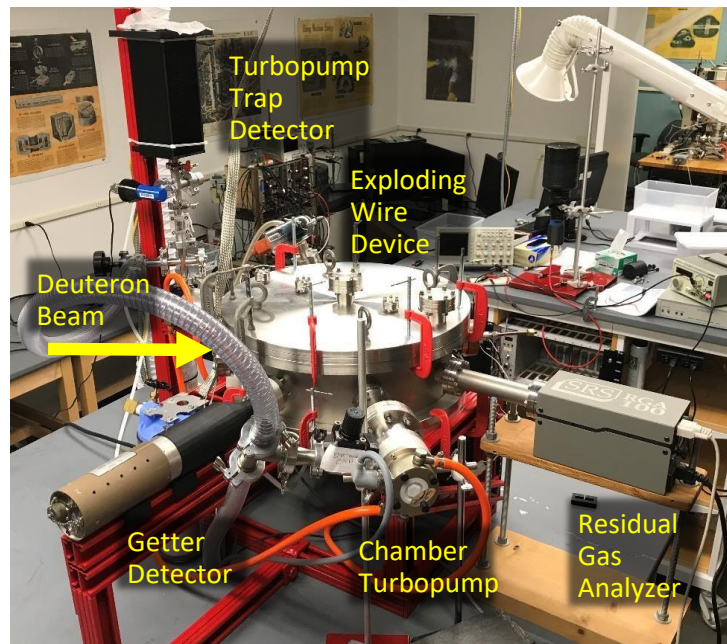
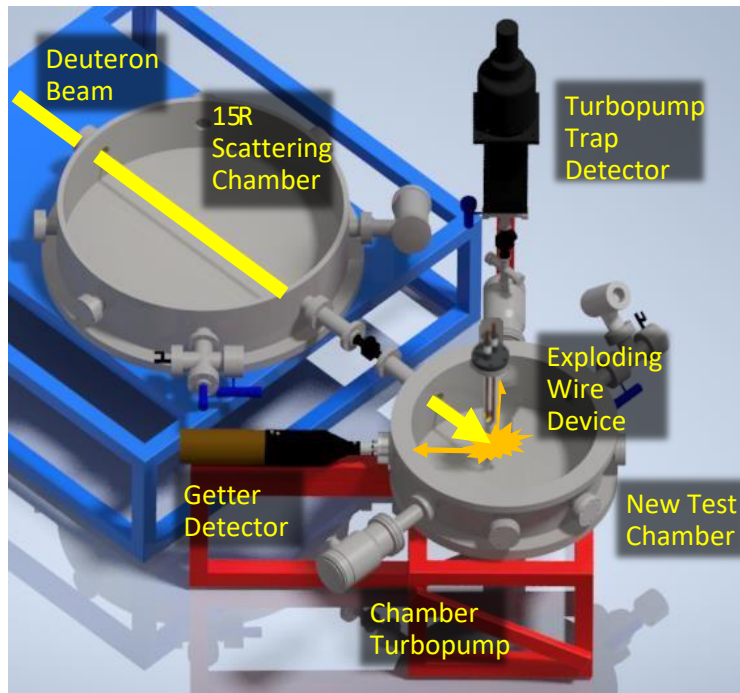


Figure 53. The exploding wire experiment. (Top) A 3-D CAD drawing of SUNY Geneseo's 30R Pelletron beamline with the Houghton College test chamber attached to the end of the beamline. The deuteron beam will travel through an inlet into the test chamber and strike the foil or wire, activating it. After a set period of time the beam will be stopped and a large current will be driven through the wire or foil, causing the radioactive material to evaporate into the chamber where it will be collected by the getter detector or trapped in the turbopump, which (not pictured here) has the  $4\pi$  detector attached to its outlet. (Bottom) A photo of the new test chamber which would be transported to SUNY Geneseo to be attached to the end of the pelletron beamline.

Table 7. Candidate reactions for the exploding wire experiment. Typical properties of the deuteron beam generated by the 30R Pelletron have been used in the calculations of the expected yields. Maximum yield occurs when the production rate of the product nuclei matches its decay rate.

Reaction	Reaction Threshold (MeV)	Reactant Natural Abundance (%)	Approx. Cross-Section (barns)	Product Half-Life (s)	Product Beta End Point Energy (MeV)	Yield (Total Number of Product Nuclei)
<b>Deuteron Reaction:</b>						
Deuteron beam 10 nA, Deuterons/second = $6.25 \times 10^{10}$ , 2 MeV						
$^{27}\text{Al}(d, p)^{28}\text{Al}$	0.0	100	$1.5 \times 10^{-1}$	134.7	2.8	$3.3 \times 10^7$
$^{65}\text{Cu}(d, p)^{66}\text{Cu}$	0.0	31	$6.5 \times 10^{-2}$	307.2	2.6	$5.2 \times 10^6$
<b>Neutron Reaction:</b>						
Deuteron beam 10 nA, Deuterons/second = $6.25 \times 10^{10}$ , 2 MeV						
Neutron Energy = 5 MeV, neutrons/second = $3.87 \times 10^6$						
$^{19}\text{F}(n, \alpha)^{16}\text{N}$	1.6	100	$2.1 \times 10^{-1}$	7.1	4.2	$1.6 \times 10^4$
$^{55}\text{Mn}(n, p)^{55}\text{Cr}$	1.9	100	$2.0 \times 10^{-2}$	209.8	2.6	$2.6 \times 10^5$
$^{27}\text{Al}(n, p)^{27}\text{Mg}$	1.9	100	$2.0 \times 10^{-3}$	567.4	1.7	$1.3 \times 10^4$

### 5.3.2. Second LLE Ride-Along

Additionally, a return to LLE with an improved data acquisition system and additional shielding for the detectors would give further insight into the behavior of the electronics after a high yield D-T shot, as well as a more accurate and hopefully reduced background measurement. Currently, professors and students from the Houghton College electrical engineering program are designing a new FPGA for the data acquisition system which would have reduced read-out times and a larger data buffer. Once tested, this new FPGA could be used during this second ride-along experiment, potentially reducing dead-time and the effect of pile-up of the background measurements.

### 5.4. Conclusion

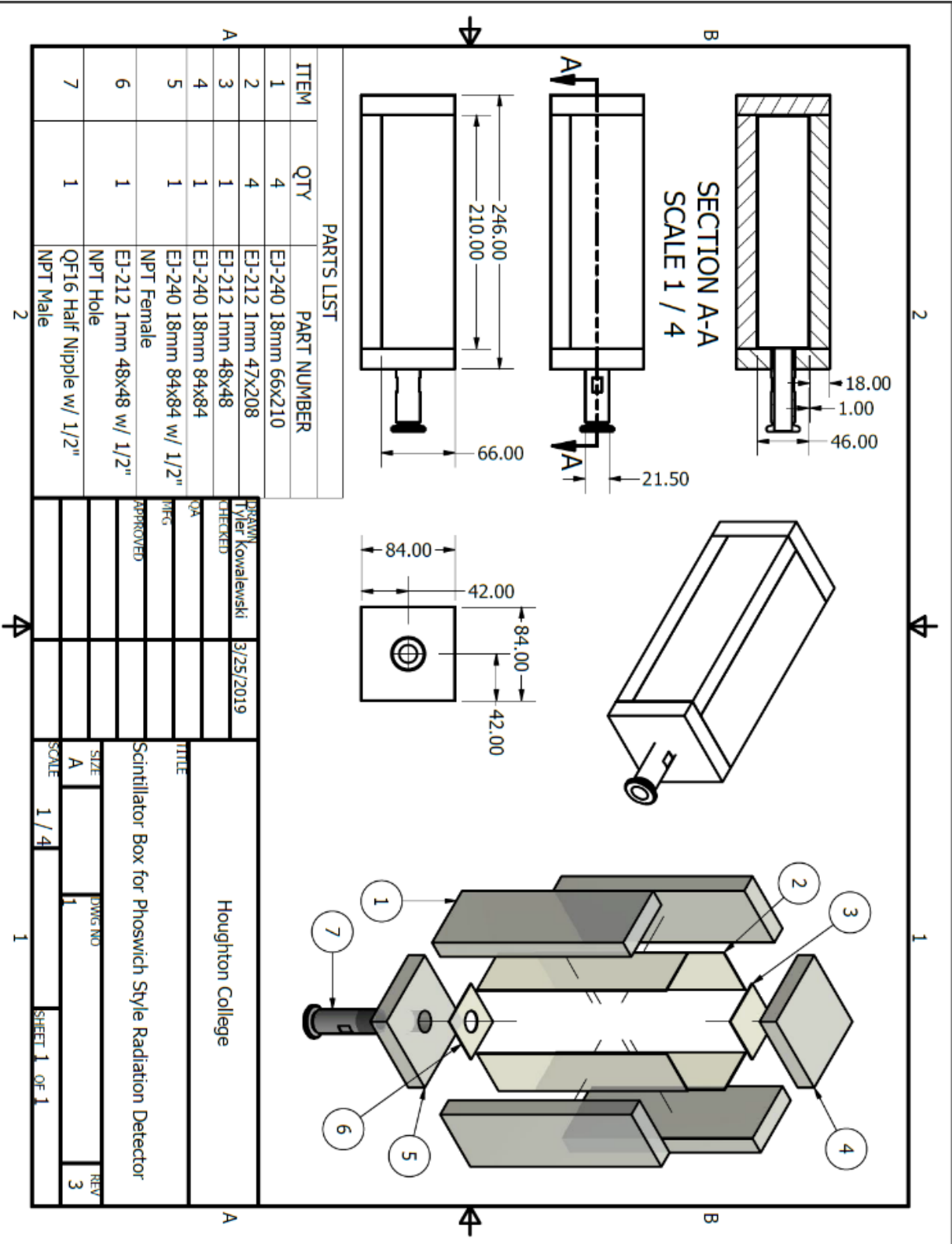
Due to its ability to generate a large number of fusion reactions within an extremely short period of time, ICF could potentially be used to study fundamental nuclear science. Many

reactions that previously could not be measured, due to their extremely small cross-sections at low energies, could potentially be measured using the proposed methodology. The measured cross-sections can then be used to improve big bang nucleosynthesis and stellar nucleosynthesis models, as well as be used in the field of fusion energy generation.

Two phoswich scintillator detectors have been constructed that could be used to detect and count the decays of products from reactions of interest. These detectors have been tested and simulated in order to characterize their behavior in the seconds after a high yield D-T shot at LLE on the OMEGA-60 laser system. A preliminary measurement of the background in the seconds after a high yield D-T shot has been made, and analysis of these results, as well as the results of simulations of the detector system, is ongoing.

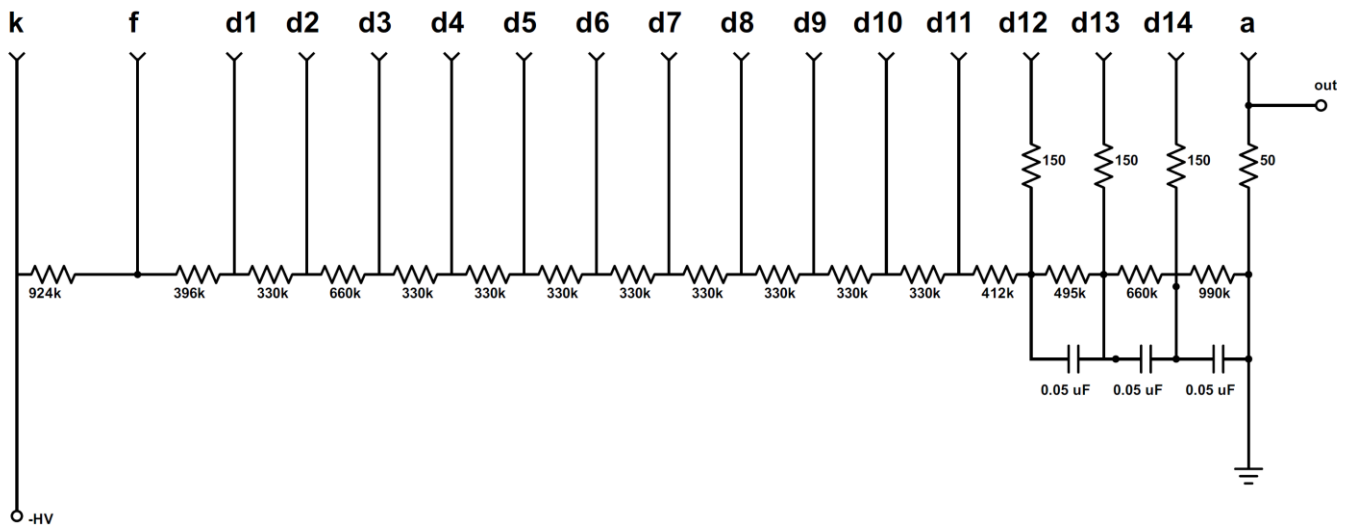
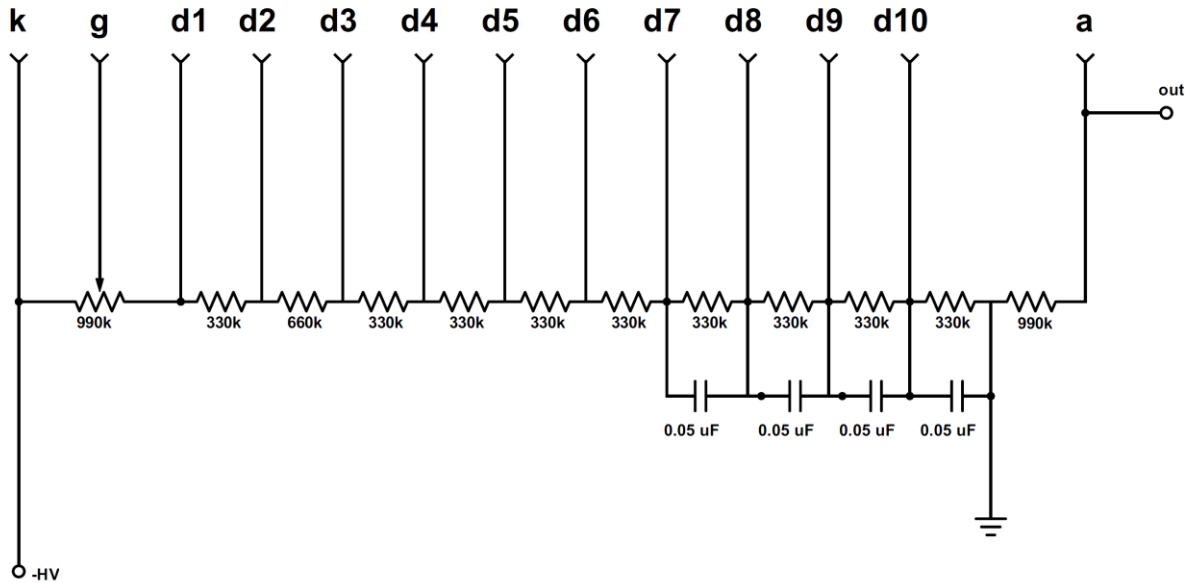
Appendix A

CAD DRAWING OF THE  $4\pi$  PHOSWICH DETECTOR



Appendix B

PMT BASE CIRCUITS

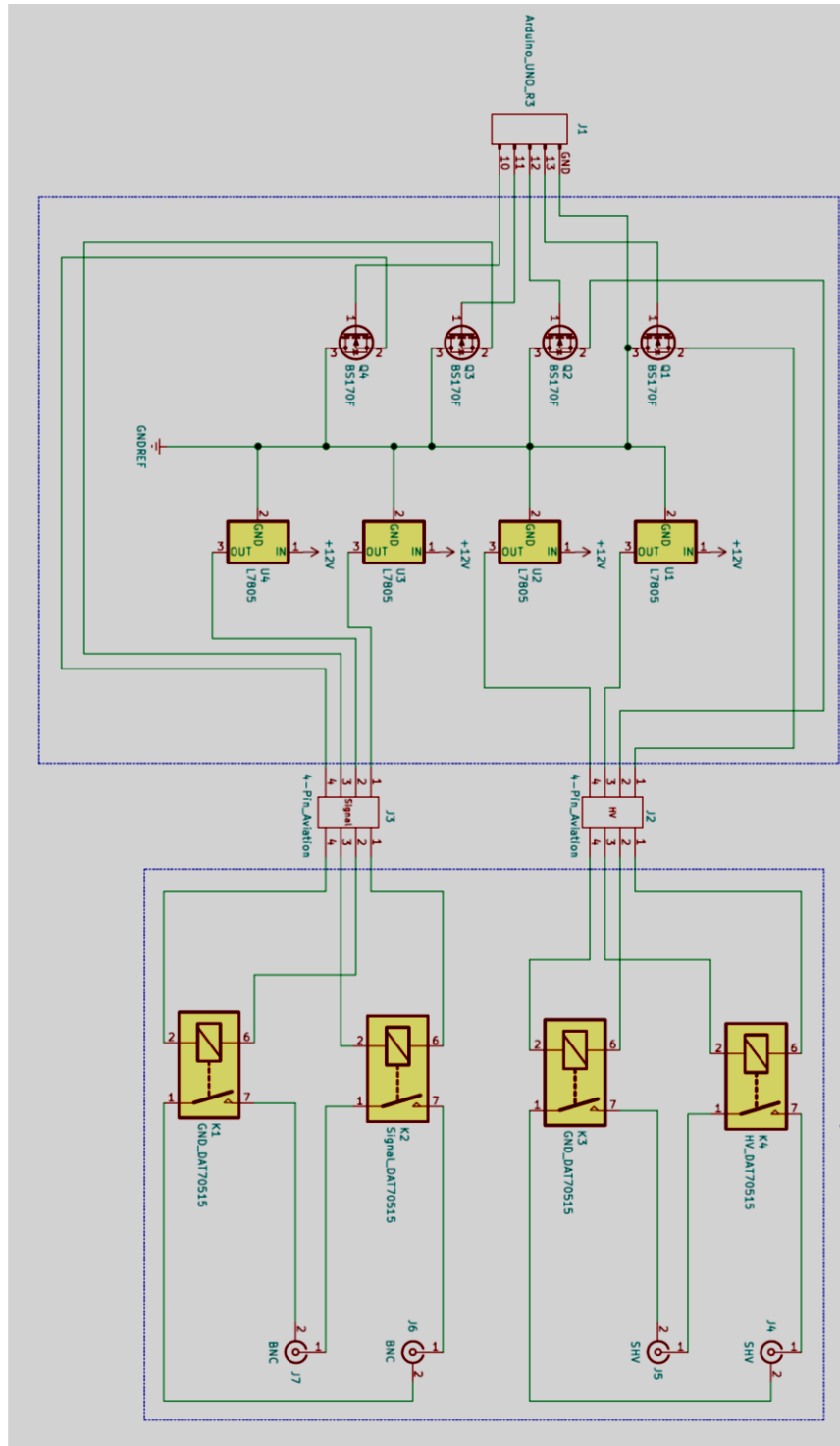


The custom base that was designed and built for the ADIT B133D01 (top) and ET Enterprises 9823KB (bottom) phototubes.



# Appendix C

## SCHEMATIC FOR THE RELAY ISOLATION CIRCUIT



## Appendix D

### FEMTODAQ PYTHON CODE RUNNING ON BEAGLEBONE

```
#!/usr/bin/python

# SLICS.py
# Short-Lived Isotope Counting System
# (c) 2019 Mark Yuly
#
# based on:
# energy_ex.py
# (c) 2016 SkuTek Instrumentation
# Author: D. Hunter
#
# versions:
# 0.1 09/22/16 - initial version based
# on histogram_ex.py
# 1.0 10/11/16 DH - corrected usage
# because ARMED is not active high
# 1.1 10/25/16 DH - updated logic for
# status read
#
# Capture energy data from the FemtoDAQ on
# inputs 0 and 1
# Create a CSV compatible text file with the
# data
#
# based on:
# decay_exp.py
# (c) 2016 Mark Yuly

import sys,time,datetime
from timeit import default_timer as timer
from FemtoLib import * # import the
Digitizer class
import Adafruit_BBIO.GPIO as GPIO

# from DAQfile import DataFile # import
the DataFile class

### GPIO parameters
GPIO_A = "GPIO0_22" # input channel A
GPIO_B = "GPIO1_29" # input channel B

### parameters for data capture
OFFSET0 = 0 #offset %
OFFSET1 = 0 #offset %

SIG_POLO = NONINV # ADC polarity
SIG_POL1 = NONINV # ADC polarity
TRIG_POL = RISING # Trigger polarity

BLR0 = DISABLE # baseline restore
BLN_BLOCK0 = 300 # [samples] baseline
blocking period
BLR1 = DISABLE # baseline restore
BLN_BLOCK1 = 300 # [samples] baseline
blocking period

PULSE_WIN = 35 # [samples] pulse height
window
SIG_AVG0 = 4 # [samples] signal
averaging time (QDC length)
SIG_AVG1 = 4 # [samples] signal
averaging time (QDC length)

PT_DELAY = 500 # [samples] post trigger
delay

# main routine
if __name__ == '__main__':
    if len(sys.argv) < 4: # need run
        number and timeout parameter
            print 'Usage: decay_exp.py run_num t
            repeats'
            print ' run_num = starting run
            number'
            print ' t = time out value
            (milliseconds) [1-65535]'
            print ' repeats = number of times to
            repeat time out value for a given run \n'
            print 'Digital I/O:'
            print ' 0 = (IN) External Trigger'
            print ' 1 = (IN) Veto'
            print ' 2 = (OUT) Armed'
            print ' 3 = (OUT) Logging Busy'
            sys.exit()

    # convert run number and catch any
    errors
    try:
        run = int(sys.argv[1])
    except:
        print 'Invalid starting run number'
        sys.exit()

    if (run < 0):
        print 'Invalid starting run number
        (must be >= 0)'
        sys.exit()

    # convert timeout and catch any errors
    try:
        TimeOut = int(sys.argv[2])
    except:
        print 'Invalid timeout value (must
        be 1-65535)'
        sys.exit()

    if (TimeOut <= 0):
        print 'Invalid timeout value (must
        be 1-65535)'
        sys.exit()

    try:
        repeats = int(sys.argv[3])
    except:
        print 'Invalid run number'
        sys.exit()

    if (repeats < 1):
        print 'Invalid run number (must be
        at least 1)'
        sys.exit()

    #####
    # SET UP THE FEMTODAQ
```

```

#####

digi = Digitizer() # create a digitizer
object
digi.WaitForReady() # wait for it to be
ready

# read the firmware
fwStr = digi.GetFirmwareString()

# read the ADctype from the digitizer
ADctype = digi.IdentifyADC()
digi.InitADC() # normal mode

# turn off data and pulse test mode in
case they were on before
digi.DisableDataTest()
digi.DisableInternalPulseGenerator()

digi.SetChannelSignalPolarity(0,SIG_POL0)

digi.SetChannelSignalPolarity(1,SIG_POL1)

digi.SetChannelOffsetVoltage(0,OFFSET0)
digi.SetChannelOffsetVoltage(1,OFFSET1)

if BLR0:
    digi.EnableChannelBaselineRestore(0)
else:

```

```

digi.DisableChannelBaselineRestore(0)

    if BLR1:
        digi.EnableChannelBaselineRestore(1)
    else:

digi.DisableChannelBaselineRestore(1)

digi.SetChannelBaselineBlocking(0,BLN_BLOCK0
)

digi.SetChannelBaselineBlocking(1,BLN_BLOCK1
)

    # set the signal averaging time for each
channel

digi.SetChannelSignalAveragingTime(0,SIG_AVG
0)

digi.SetChannelSignalAveragingTime(1,SIG_AVG
1)

    # set the post trigger delay
digi.SetPostTriggerDelay(PT_DELAY)

    # set the pulse energy window
digi.SetPulseEnergyWindow(PULSE_WIN)

```

## Appendix E

### C CODE USED TO ANALYZE THE PHOSWICH DETECTOR DATA

```

//
=====
//
// Analyzer.C
//
// Short-Lived Isotope Counting System
// (SLICS)
// Read SLICS data from text file and
// analyze.
// (c) 2016 Mark Yuly
//
// versions:
// 0.1 07/26/2016 MY - initial
// version, 6He experiment using Si detector
// 1.0 08/02/2017 MY - 6He experiment
// using phoswich detector
// 1.1 07/23/2018 MY - 41Ar experiment
// 1.2 12/17/2019 MY - OMEGA ride along
// experiment
// 1.3 06/17/2020 MY - stripped down
// analyzer for OMEGA expt
// 2.0 06/17/2020 MY - OMEGA expt, major
// corrections for deadtime using femtoDAQ

#include <iostream>

//
=====
// Subroutine to read data from run file,
// fill ntuple
//
=====
void read_file(TString fname, TNtuple
*ntuple) {

char cline[256]; // input
line buffer

// store data from FemtoDAQ
float adc0,adc1;
float timestamp;

printf("Opening input file: %s \n",
fname.Data());
ifstream in;
in.open(fname.Data());

// Read in the first 10 comment lines
for (int i=1; i<10; i++) {
in.getline(cline,256);
//printf("%s \n",cline);
cout<<"line"<<i<<": "<<cline<<endl;
}

// number of data lines read in from each
file
Int_t nlines = 0;

// current index of event
Int_t i=0;

// Read in data and fill histograms and
// ntuple
do {
in >> timestamp>>adc0>>adc1;
if (in.fail()) break;
if (nlines < 10) printf("%d time=%f
adc0=%f adc1=%f
\n",in.good(),timestamp,adc0,adc1);
//printf("%d time=%f adc0=%f adc1=%f
\n",in.good(),timestamp,adc0,adc1);
ntuple->Fill(timestamp,adc0,adc1);
nlines++;
} while(!in.eof());

printf(" Found %d points\n",nlines);
//printf("start=%ld \n",start);
//printf("time=%ld adc0=%d adc1=%d
\n",timestamp,adc0,adc1);

in.close();
}

//
=====
// Main
//
=====

// Calibration points to use for
// correct_channel
int a1 = 520;
int a2 = 725;
int b1 = 660;
int b2 = 550;
int c1 = 620;
int c2 = 1100;
int alp = 10;
int a2p = 475;
int b1p = 790;
int b2p = 190;
int c1p = 10;
int c2p = 975;

//calibration constants based on above
// points
double m1 = (alp*(b2-c2)-a2*(b1p-
c1p)+b1p*c2-b2*c1p)/(a1*(b2-c2)-a2*(b1-
c1)+b1*c2-b2*c1);
double m2 = -1*(alp*(b1-c1)-a1*(b1p-
c1p)+b1p*c1-b1*c1p)/(a1*(b2-c2)-a2*(b1-
c1)+b1*c2-b2*c1);
double m3 = (a2p*(b2-c2)-a2*(b2p-
c2p)+b2p*c2-b2*c2p)/(a1*(b2-c2)-a2*(b1-
c1)+b1*c2-b2*c1);
double m4 = (a1*(b2p-c2p)-a2p*(b1-
c1)+b1*c2p-b2p*c1)/(a1*(b2-c2)-a2*(b1-
c1)+b1*c2-b2*c1);

```

```

int correct_channel(int x1, int x2, int isX)
{
    if (isX == 1) {
        return m1*(x1-a1)+m2*(x2-a2)+a1p;
    } else if (isX == 0) {
        return m3*(x1-a1)+m4*(x2-a2)+a2p;
    } else {
        return 0;
        return 0;
    }
}

void analyze(TString fname="test") {
//
// Read in and analyzed data from file
//fname".
//
// If the first three characters in fname
// are "run" then the file is assumed ot be a
// single run,
// otherwise its assumed to be a list of
// runs, a single column of run numbers.
//
// The cuts are read from the file
// analyzer_cuts.root. If this file does not
// exist, a graphical
// cut is made and saved to
// analyzer_cuts.root.
//
// gStyle->SetOptStat(0); //
// removes statistics box from everythings

// ===== USER SETTABLE VALUES
// =====
// length of run in seconds
Int_t run_length = 300;

// size of time bin (ms)
Int_t time_bin_size =100;

// width of linear gate, us
float LGwidth = 3.0;

// switches
bool consec = false; //require consecutive
timestamps
bool pileup = false; //correct for linear
gate width
bool edges = false; //fix bins on edges
of dead tiem due to femtoDAQ data transfer
bool deadtime = false; //correct for
deadtime
//
// =====
// =====

TString run_file; // list of run
file names to process
int numlist; // number of
files to process
int in_run_num; // run number to
input
int ii;
char buffer[100]; // temporary
buffer

char last_buffer[100]; // temporary
buffer of last item processed
char cline[256]; // input line
buffer
float timestamp;
float prev_timestamp;
float last_timestamp;
float adc0,adc1;
float prev_adc0,prev_adc1;
float* row_content; // pointer to
ntuple event
int nbin;
float blow, bhigh,bwidth; // low and high
edges of bin given by nbin

// number of time bins
Int_t num_time_bin =
run_length*1000./time_bin_size ;
printf("\n Number of time bins
%d\n\n",num_time_bin);

// exponential decay + background fit
function
TF1 *decay_func = new TF1("user","[0]*exp(-
(log(2)/[1])*x) + [2]*exp(-(log(2)/[3])*x)
+ [4]*exp(-(log(2)/[5])*x) +
[6]+[7]*x",0.,run_length);
//TF1 *decay_func = new
TF1("user","[0]*exp(-(log(2)/[1])*x) +
[2]*exp(-(log(2)/[3])*x) +
[4]+[5]*x",0.,run_length);
//TF1 *decay_func = new TF1("user","[0]*(1.-
exp(-[1]*x)) + [2]*(1.-exp(-[3]*x))+[4]*(1.-
exp(-[5]*x))+[6]*x+[7]",0.,run_length);

//Create the .root file to store
TString root_name = fname;
root_name.Append(".root");
TFile *f = new TFile(root_name,"RECREATE");
TFile *f_cut;
TCutG *cutg;
TCutG *mycutg;

//
// =====
// =====
// Read in the cuts from analyzer_cuts.root
//
// =====
// =====

bool GCUT; // Do a graphical cut and
save (true) or use file (false)

if(gSystem-
>AccessPathName("analyzer_cuts.root")){ //
do graphical cuts
f_cut = new
TFile("analyzer_cuts.root","new");
std::cout << "Creating file
analyzer_cuts.root." << std::endl;
GCUT = true;
} else {
// use cuts from file
f_cut = new
TFile("analyzer_cuts.root");
std::cout << "Found file
analyzer_cuts.root." << std::endl;
//mycut->Print();
GCUT = false;
}
}

```

```

f->cd();

// create the raw data ntuple
TNtuple *ntuple = new TNtuple("ntuple","data
from ascii file","timestamp:adc0:adc1");

//
=====
// Read in the data from single file or file
list
//
=====

//Either open a single run file, or loop
through a list of run files
if (fname(0,3)=="run") { // single
run file
printf("Opening run file: %s\n",
fname.Data());
read_file(fname, ntuple);
printf(" File opened and read
successfully.\n");
}
else {
printf("Opening run list file: %s\n",
fname.Data());
ifstream in_list;
in_list.open(fname.Data());

// number of data lines read in from
each file
numlist = 0;

// Read in the file names
do {
in_list >> in_run_num;

sprintf(buffer,"run_%04d.dat",in_run_num);
run_file=buffer;
if (buffer[7] != last_buffer[7])
read_file(run_file, ntuple);
numlist++;
strcpy(last_buffer, buffer);
} while (!in_list.eof());
}

// Total number of entries in the ntuple
int total_ntuple; // total number
of entries in the ntuple
total_ntuple=ntuple->GetEntries();

printf(" Found %d runs in list\n",numlist);
printf(" Total number of entries in ntuple:
%d \n",total_ntuple);

//
=====
// create the filtered data mtuple --
eliminate non-consecutive
//
=====
TNtuple *mtuple = new
TNtuple("mtuple","consecutive
data","timestamp:adc0:adc1");

```

```

if(consec) {
// filter the data
prev_timestamp = 0;
prev_adc0=0;
prev_adc1=0;

ii=0;
for (int irow=0;irow<total_ntuple;irow++){
ntuple->GetEntry(irow);
row_content = ntuple->GetArgs();
timestamp = row_content[0];
adc0 = row_content[1];
adc1 = row_content[2];

if (timestamp-prev_timestamp>0) {
if (prev_timestamp!=0) mtuple-
>Fill(prev_timestamp,prev_adc0,prev_adc1);
ii=ii+1;
}
//else printf("Event %d out of
order\n",irow);

prev_timestamp=timestamp;
prev_adc0=adc0;
prev_adc1=adc1;
}
}
else mtuple=ntuple;

// Total number of entries in mtuple
int total_mtuple; // total number
of entries in the mtuple
total_mtuple=mtuple->GetEntries();
printf("total mtuple = %d\n",total_mtuple);

//
=====
// create the filtered data otuple --
eliminate less than LGwidth
//
=====
TNtuple *otuple = new TNtuple("otuple","LG
data","timestamp:adc0:adc1");

if(pileup) {
// filter the data
prev_timestamp = 0;
prev_adc0=0;
prev_adc1=0;

ii=0;
for (int irow=0;irow<total_mtuple;irow++){
mtuple->GetEntry(irow);
row_content = mtuple->GetArgs();
timestamp = row_content[0];
adc0 = row_content[1];
adc1 = row_content[2];

if (timestamp-
prev_timestamp>LGwidth*100.) {
if (prev_timestamp!=0) otuple-
>Fill(prev_timestamp,prev_adc0,prev_adc1);
ii=ii+1;
}

prev_timestamp=timestamp;
prev_adc0=adc0;

```

```

    prev_adcl=adcl;
}
}
else otuple=mtuple;

// Total number of entries in otuple
int total_otuple; // total number
of entries in the ntuple
total_otuple=otuple->GetEntries();
printf("total otuple = %d\n",total_otuple);

//
=====
// Create histograms
//
=====

// create the temporary histograms
TH1F *htemp = new
TH1F("htemp","",num_time_bin,0.,run_length);

// create the display histograms
int dE_range = 6000;
int E_range = 6000;

TH1F *h0 = new
TH1F("h0","ADC0_spectrum",dE_range,0,dE_rang
e-1);
h0->SetFillColor(0);
TH1F *h1 = new
TH1F("h1","ADC1_spectrum",E_range,0,E_range-
1);
h1->SetFillColor(0);
TH2F *h01 = new TH2F("h01","ADC0 vs
ADC1",E_range,0,E_range-
1,dE_range,0,dE_range-1);
h01->SetFillColor(0);
TH2F *h02 = new TH2F("h02","ADC0 vs ADC1
Corrected",E_range,0,E_range-
1,dE_range,0,dE_range-1);
h02->SetFillColor(0);
TH1F *ht = new TH1F("ht","counts vs
time",num_time_bin,0.,run_length);
ht->SetFillColor(0);
TH1F *hlive = new
TH1F("hlive","",num_time_bin,0.,run_length);
hlive->SetFillColor(2);
TH1F *hweight = new
TH1F("hweight","",num_time_bin,0.,run_length
);
hweight->SetFillColor(3);

// create intermediate temporary histogram
for (int irow=0;irow<total_otuple;++irow){

    // get the event
    otuple->GetEntry(irow);
    row_content = otuple->GetArgs();
    timestamp = row_content[0];
    htemp->Fill( timestamp/1.0e8);

}

float weight[num_time_bin]; // weights for
each time bin

if (edges) {

```

```

//
=====
// Scan through the histogram to weight
partially filled bins just to the left of
FemtoDAQ download
//
=====

int irow;
for (int nbin=1;nbin<num_time_bin;nbin++){
    weight[nbin-1] = 1;

    // Look at bin to left -- may be only
partly filled
    if ( htemp->GetBinContent(nbin) < 3 &&
htemp->GetBinContent(nbin-1) > 3 ) {
        blow=ht->GetXaxis()-
>GetBinLowEdge(nbin-1);
        bwidth=ht->GetXaxis()-
>GetBinWidth(nbin-1);
        bhigh=blow+bwidth;
        last_timestamp = 0;
        for
(irow=0;irow<total_otuple;irow++){
            //scan through events to find those in bin
to left
            // get the event
            otuple->GetEntry(irow);
            row_content = otuple-
>GetArgs();
            timestamp = row_content[0];
            //printf("test %d %d %f %f
%f\n",nbin-
1,irow,last_timestamp/1.0e8,timestamp/1.0e8,
blow,bhigh);
            if (timestamp/1.0e8<bhigh)
last_timestamp = timestamp;
            else break;
        }
        weight[nbin-1] = (bhigh-
blow)/(last_timestamp/1.0e8-blow);
        //printf("left %d %d %f %f %f %f
%f\n",nbin-
1,irow,last_timestamp/1.0e8,timestamp/1.0e8,
blow,bhigh,weight[nbin-1]);
    }
}

//
=====
// Scan through the histogram to weight
partially filled bins just to the right of
FemtoDAQ download
//
=====

for (int nbin=num_time_bin;nbin>0;nbin--){

    // Look at bin to right -- may be only
partly filled
    if ( htemp->GetBinContent(nbin) < 3 &&
htemp->GetBinContent(nbin+1) > 3 ) {
        blow=ht->GetXaxis()-
>GetBinLowEdge(nbin+1);
        bwidth=ht->GetXaxis()-
>GetBinWidth(nbin+1);
        bhigh=blow+bwidth;

```

```

        last_timestamp = 0;
        for
(irow=total_otuple;irow>0;irow--){
//scan through events to find those in bin
to left
                // get the event
                otuple->GetEntry(irow);
                row_content = otuple-
>GetArgs();
                timestamp = row_content[0];
                //printf("test %d %d %f %f
%f %f\n",nbin-
1,irow,last_timestamp/1.0e8,timestamp/1.0e8,
blow,bhigh);
                if (timestamp/1.0e8>blow)
last_timestamp = timestamp;
                else break;
        }
        weight[nbin+1] = (bhigh-
blow)/(bhigh-last_timestamp/1.0e8);
        //printf("right %d %d %f %f %f %f
%f\n",nbin+1,irow,last_timestamp/1.0e8,times
tamp/1.0e8,blow,bhigh,weight[nbin+1]);
    }
}
}
else {
    for (int
nbin=1;nbin<num_time_bin;nbin++){
        weight[nbin-1] = 1;
    }
}

//
=====
// Fill the ADC histograms
//
=====

for (int irow=0;irow<total_mtuple;++irow){
    // get the event
    otuple->GetEntry(irow);
    row_content = otuple->GetArgs();
    timestamp = row_content[0];
    adc0 = row_content[1];
    adc1 = row_content[2];

    // fill the histograms
    h0->Fill(adc0); // hist dE
    h1->Fill(adc1); // hist E
    h01->Fill(adc1,adc0); // dE vs E
    //h02->Fill(500,500); // dE vs E
    h02-
>Fill(correct_channel(adc1,adc0,1),correct_c
hannel(adc1,adc0,0)); // dE vs E
calibrated and E-dE channel bleed over
corrected
    }

//
=====
// Canvas 1 -- Show the ADC spectra
//
=====

```

```

// Create Canvas 1 and three pads

TCanvas *c1 = new
TCanvas("c1",fname.Data(),200,10,800,1200);
c1->SetFillColor(0);

TPad *pad1 = new
TPad("pad1","ADC0",0.03,0.62,0.50,0.92,21);
pad1->SetFillColor(0);
TPad *pad2 = new
TPad("pad2","ADC1",0.51,0.62,0.98,0.92,21);
pad2->SetFillColor(0);
TPad *pad3 = new TPad("pad3","ADC0 vs
ADC1",0.03,0.02,0.50,0.57,21);
pad3->SetFillColor(0);
TPad *pad4 = new TPad("pad3","ADC0 vs
ADC1",0.51,0.02,0.98,0.57,21);
pad4->SetFillColor(0);
pad1->Draw();
pad2->Draw();
pad3->Draw();
pad4->Draw();

// Settings and Sizes

pad1->SetBottomMargin(0.15);
pad1->SetLeftMargin(0.14);
pad2->SetBottomMargin(0.15);
pad2->SetLeftMargin(0.14);

h0->GetXaxis()->SetTitle("dE (ADC0)");
h0->GetXaxis()->SetLabelSize(0.05);
h0->GetXaxis()->SetTitleSize(0.05);
h0->GetYaxis()->SetTitle("Number of
counts");
h0->GetYaxis()->SetLabelSize(0.05);
h0->GetYaxis()->SetTitleSize(0.05);
h0->GetYaxis()->SetTitleOffset(1.4);

h1->GetXaxis()->SetTitle("E (ADC1)");
h1->GetXaxis()->SetLabelSize(0.05);
h1->GetXaxis()->SetTitleSize(0.05);
h1->GetYaxis()->SetTitle("Number of
counts");
h1->GetYaxis()->SetLabelSize(0.05);
h1->GetYaxis()->SetTitleSize(0.05);
h1->GetYaxis()->SetTitleOffset(1.4);

h01 -> SetYTitle("dE (ADC0)");
h01->GetYaxis()->SetTitleOffset(1.3);
h01 -> SetXTitle("E (ADC1)");
//h01->GetYaxis()->SetRange(1000, 2200);
//h01->GetXaxis()->SetRangeUser(300, 2000.);

h02 -> SetYTitle("dE (ADC0)");
h02->GetYaxis()->SetTitleOffset(1.3);
h02 -> SetXTitle("E (ADC1)");
//h02->GetYaxis()->SetRange(1000, 2200);
//h02->GetXaxis()->SetRangeUser(300, 2000.);

pad1->cd();
h0->Draw();
pad2->cd();
h1->Draw();
pad3->cd();
h01->Draw();
pad3->Draw();
pad4->cd();
h02->Draw();
pad4->Draw();

```



```

c1->Update();
// Do the graphical cuts

if(GCUT) {
    f_cut->cd();
    cout << "Please make a TCutG" << endl;

    pad3->cd();
    gPad->Modified(); // make sure
    gPad->Update(); // hist is drawn

    //cutg->SetLineColor(kGreen);
    cutg=(TCutG*)gPad-
>WaitPrimitive("CUTG","CutG");
    cutg->SetName("mycut");
    mycutg=(TCutG *)gROOT-
>FindObject("mycut");
    mycutg->SetLineColor(kRed);
    mycutg->Draw();
    printf("\nSaved and applied the
following cuts:\n\n");
    mycutg->Print();
    mycutg->Write();

    f_cut->Close();
}
else {
    f_cut->cd();
    cout<<"Drawing cuts from file."<<endl;

    cutg=(TCutG *)f_cut->Get("mycut");
    mycutg=(TCutG *)gROOT-
>FindObject("mycut");
    pad3->cd();

    mycutg->SetLineColor(kRed);
    mycutg->Draw();
    printf("\nApplied the following
cuts:\n\n");
    mycutg->Print();

    f_cut->Close();
}

//
=====
// Fill the decay time histograms
//
=====

    int count_in=0;
    for (int
irow=0;irow<total_mtuple;++irow){

        // get the event
        otuple->GetEntry(irow);
        row_content = otuple->GetArgs();
        timestamp = row_content[0];
        adc0 = row_content[1];
        adc1 = row_content[2];

        // fill the histogram

        if (mycutg->IsInside(adc1,adc0)) {
            //printf("isinside = %d %f %f
%f\n", irow, adc1, adc0, timestamp/1.0e8);
            ht->Fill( timestamp/1.0e8 );
            count_in++;
        }
    }
    printf("Events in cut: %d\n",count_in);

    //
=====
// Rescale time bns by weight and deadtime
//
=====
    float NN; // number in bin
    float k=LGwidth*1e-6; // deadtime is
LGwidth us
    float flive; // live time fraction

    for (int nbin=1;nbin<num_time_bin;nbin++){

        NN=ht->GetBinContent(nbin);
        bwidth=ht->GetXaxis()-
>GetBinWidth(nbin);

        if (deadtime) flive = (bwidth-
k*NN)/bwidth;
        else flive=1;

        //if ( flive < 0.98 ) hlive-
>SetBinContent(nbin,flive);
        //else hlive->SetBinContent(nbin,2);

        hlive->SetBinContent(nbin,flive);

        hweight-
>SetBinContent(nbin,weight[nbin]);

        //if (NN*weight[nbin]/flive>3) ht-
>SetBinContent(nbin,NN*weight[nbin]/flive);
        //else ht->SetBinContent(nbin,0);

        ht-
>SetBinContent(nbin,NN*weight[nbin]/flive);

        //printf("bin %d binedge %f content %f
weight %f live %f \n",nbin,ht->GetXaxis()-
>GetBinLowEdge(nbin),ht-
>GetBinContent(nbin),weight[nbin],flive);
    }

    //
=====
// Canvas 2 -- Show the decay histogram vs
time and fit, livetime and weights
//
=====

    // Create Canvas 2 and three pads

    TCanvas *c2 = new
TCanvas("c2",fname.Data(),200,10,800,1600);
    TPad *dpad1 = new
TPad("decays","decays",0.03,0.6,0.97,1.,21);
    dpad1->SetFillColor(0);
    TPad *dpad2 = new
TPad("live","live",0.03,0.3,0.97,0.6,21);
    dpad2->SetFillColor(0);

```

```

TPad *dpad3 = new
TPad("weight", "weight", 0.03, 0.0, 0.97, 0.3, 21)
;
dpad3->SetFillColor(0);
dpad1->Draw();
dpad2->Draw();
dpad3->Draw();

// decay curve

dpad1->cd();
gPad->SetBottomMargin(0.15);
ht->GetYaxis()->SetTitle("Number of
counts");
ht->GetXaxis()->SetTitle("time (s)");
gStyle->SetErrorX(0.0001);
ht->SetLineColor(kBlack);
ht->SetMarkerStyle(20);
ht->SetFillColor(kGreen);
ht->GetXaxis()->SetLabelSize(0.05);
ht->GetXaxis()->SetTitleSize(0.05);
ht->GetYaxis()->SetLabelSize(0.05);
ht->GetYaxis()->SetTitleSize(0.05);
ht->GetYaxis()->SetTitleOffset(1.7);
//ht->GetYaxis()->SetRangeUser(0, 70000);

ht->Draw("E1");
gPad->Draw();

// live time fraction

dpad2->cd();
gPad->SetBottomMargin(0.15);
hlive->GetYaxis()->SetTitle("Livetime
fraction");
hlive->GetXaxis()->SetTitle("time (s)");
gStyle->SetErrorX(0.0001);
hlive->SetLineColor(kBlack);
hlive->SetMarkerStyle(20);
hlive->SetFillColor(kGreen);
hlive->GetXaxis()->SetLabelSize(0.06);
hlive->GetXaxis()->SetTitleSize(0.06);

hlive->GetYaxis()->SetLabelSize(0.06);
hlive->GetYaxis()->SetTitleSize(0.06);
hlive->GetYaxis()->SetTitleOffset(.7);

hlive->Draw("P");
gPad->Draw();
c2->Update();

// weight for incomplete bins

dpad3->cd();
gPad->SetBottomMargin(0.15);
hweight->GetYaxis()->SetTitle("Bin Weight");
hweight->GetXaxis()->SetTitle("time (s)");
gStyle->SetErrorX(0.0001);
hweight->SetLineColor(kBlack);
hweight->SetMarkerStyle(20);
hweight->SetFillColor(kGreen);
hweight->GetXaxis()->SetLabelSize(0.06);
hweight->GetXaxis()->SetTitleSize(0.06);
hweight->GetYaxis()->SetLabelSize(0.06);
hweight->GetYaxis()->SetTitleSize(0.06);
hweight->GetYaxis()->SetTitleOffset(0.7);

hweight->GetYaxis()->SetRangeUser(0.8, 1.2);

hweight->Draw("P");
gPad->Draw();
c2->Update();

// write the histogram and ntuples to root
file
f->cd();
f->Write();

}

```

## References

- 
- [1] A. Eddington, *The Scientific Monthly* **11**, 297 (1920).
- [2] A. Eddington, *Monthly Notices of the Royal Astronomical Society* **77**, 16 (1916).
- [3] H. A. Bethe, *Physical Review* **55**, 434 (1939).
- [4] R. A. Alpher, H. Bethe, G. Gamow, *Physical Review* **73**, 803 (1948).
- [5] L. Gresh, R. McCrory, J. Soures, *Inertial Confinement Fusion: An Introduction* (Laboratory for Laser Energetics, 2009).
- [6] J. Melendez and I. Ramirez, *Astrophys. J.* **615** L33 (2004).
- [7] M. Asplund et al., *Astrophys. J.* **644**, 229 (2006).
- [8] M. Kang, Y. Hu, H. Hu, and S. Zhu, *Journal of Cosmology and Astroparticle Physics* **2012**, 11 (2012).
- [9] National Nuclear Data Center Experimental Nuclear Reaction Data (EXFOR) database, <https://www.nndc.bnl.gov/exfor/>.
- [10] S. N. Abramovich *et al.*, *Bull. Russian Academy of Sciences – Physics* **50**, 62 (1986). (data taken from Ref. [11], original paper not available).
- [11] National Nuclear Data Center, information extracted from the NuDat 2 database, <http://www.nndc.bnl.gov/nudat2/>.
- [12] A. S. Belov, V. E. Kusik, Yu. V. Ryabov, *Nuovo Cimento A* **103**, 1647 (1990).
- [13] V. A. Davidenko et al., *Soviet Atomic Energy Supplement* **5**, 7 (1957). (data taken from Ref. [11], original paper not available).
- [14] A. S. Ganeev *et al.*, *Soviet Atomic Energy Supplement* **5**, 21 (1957). (data taken from Ref. [11], original paper not available).
- [15] International Atomic Energy Agency, *Decommissioning of Particle Accelerators*. (2020).
- [16] Laboratory for Laser Energetics, *Advanced Tritium Recovery System*, LLE Review **89**, 25 (2001).
- [17] United States Department of Energy, *United States Nuclear Tests: July 1945 through September 1992*. (1994) <https://www.nnss.gov>.

- 
- [18] The Nuclear Weapon Archive, <http://www.nuclearweaponarchive.org>.
- [19] J. D. Lawson, Proceedings of the Physical Society Section B **70**, 1 (1957).
- [20] J. Wesson, *The Science of Jet*, (EUROfusion, 2000).
- [21] D. Meade. Nuclear Fusion **50**, 014004 (2009).
- [22] P. T. Farnsworth, *Electric discharge device for producing interactions between nuclei*. US Patent 3,258,402 (1966).
- [23] University of Wisconsin-Madison, *Inertial Electrostatic Confinement Fusion*. (2014)  
<https://iec.neep.wisc.edu/publications.php>.
- [24] Initial Performance Results of the OMEGA Laser System, LLE Review **63**, (1996).
- [25] L. J. Waxer, et al., Optics and Photonics News **16**, 30 (2005).
- [26] E. Moses, *Multi-megajoule NIF: Ushering in a New Era in High Energy Density Science*, (LLNL, 2008).
- [27] J. -L. Miquel, C. Lion, P. Vivini, Journal of Physics: Conference Series **688**, 012067 (2016).
- [28] M. A. Stoyer, T. C. Sangster, et. al, The Review of Scientific Instruments **83**, 023505 (2012).
- [29] A.J. Koning, S. Hilaire and M.C. Duijvestijn, "TALYS-1.0", Proceedings of the International Conference on Nuclear Data for Science and Technology, April 22-27, 2007, Nice, France, editors. O. Bersillon, F. Gunsing, E. Bauge, R. Jacqmin, and S. Leray, EDP Sciences, 211 (2008).
- [30] S. N. Abramovich, B. Y. Guzhovskij, V. A. Zherebtsov, and A. G. Zvenigorodskij, International Nuclear Data Committee Report INDC(CCP)-326/L+F, (1991).
- [31] D. Ciric, B. Stepancic, R. Popic, D. Stanojevic, M. Aleksic, Fizika **4**, 193 (1972). (data taken from Ref. [11], original paper not available).
- [32] F. E. Cecil, et al., Phys. Rev. **C 27**, 6 (1983).
- [33] K. S. Nam, G. M. Osetinskii, Yadernaya Fizika **9**, 487 (1969) (Soviet Journal of Nuclear Physics **9**, 279 (1969), USA) (data taken from Ref. [11], original paper not available).
- [34] R. W. Kavanagh, C. A. Barnes, Phys. Rev. **112**, 503 (1958).

- 
- [35] N. A. Bostrom, E. L. Hudspeth, I. L. Morgan, *Phys. Rev.* **105**, 1545 (1957).
- [36] K. Cook, B.S. thesis, (Houghton College, 2019).
- [37] K. Sharp, F. Matschinsky, *Entropy* **17**, 1971 (2015).
- [38] H. S. Bosch, G. M. Hale, *Nucl. Fusion* **32**, 611 (1992).
- [39] G. Gamow, *Zeitschrift für Physik* **51**, 204 (1928).
- [40] D. T. Casey, Ph.D. thesis, (Massachusetts Institute of Technology, 2012).
- [41] R. E. Azuma, et. al., *Physics Review C* **81**, 045805 (2010).
- [42] G. M. Hale and D. C. Dodder, *Proceedings of the International Conference on Nuclear Cross Sections for Technology*, NBS Special Publication 594 (1979) (Los Alamos Report LA-UR-79-2896).
- [43] F. Wauters, et al., *Nuclear Instruments and Methods in Physics Research Section A Accelerators Spectrometers Detectors and Associated Equipment* **604**, 563(2008).
- [44] R. W. Michelmann, J. Krauskopf, J. D. Meyer, K. Bethge, *Nucl. Instrum. Methods in Physics Res* **51**, 1 (1990).
- [45] J. W. Engle, G. W. Severin, T. E. Barnhart, L. D. Knutson, R. J. Nickles, *Applied Radiation and Isotopes* **70**, 355 (2012).
- [46] F. James, *MINUIT: Function Minimization and Error Analysis*, (CERN, 1994).
- [47] *ROOT Data Analysis Framework: User's Guide*, (CERN, 2018).
- [48] A. R. Rutledge, L. V. Smith, J. S. Merritt, *International Journal of Radiation Applications and Instrumentation. Part A. Applied Radiation and Isotopes* **37**, 1029 (1986).
- [49] F. Ajzenberg-Selove, *Nuclear Physics A* **523**, 1 (1991).
- [50] National Nuclear Data Center, threshold values calculated using NNDC QCalc, <https://www.nndc.bnl.gov/qcalc/>.
- [51] M. Subaşı, et al., *Nuclear Science and Engineering* **135**, 260 (2000).
- [52] R. K. Smither, L. R. Greenwood, *Journal of Nuclear Materials* **123**, 1071 (1984).
- [53] *Introduction to GEANT4*, (CERN, 2020) (Retrieved from [https://geant4.web.cern.ch/support/user\\_documentation](https://geant4.web.cern.ch/support/user_documentation)).